Novel Calibration Techniques to Enable Next-Generation Cosmic Microwave Background Observations

by

Taylor Ashley Baildon

A dissertation submitted in partial fulfillment
of the requirements for the degree of
Doctor of Philosophy
(Physics)
in The University of Michigan
2021

Doctoral Committee:

        Professor Vanessa Sih, Co-Chair
        Dr. Sara Simon, Fermilab Wilson Fellow, Co-Chair
        Professor Myron Campbell
        Professor Dragan Huterer
        Associate Professor Christopher Miller
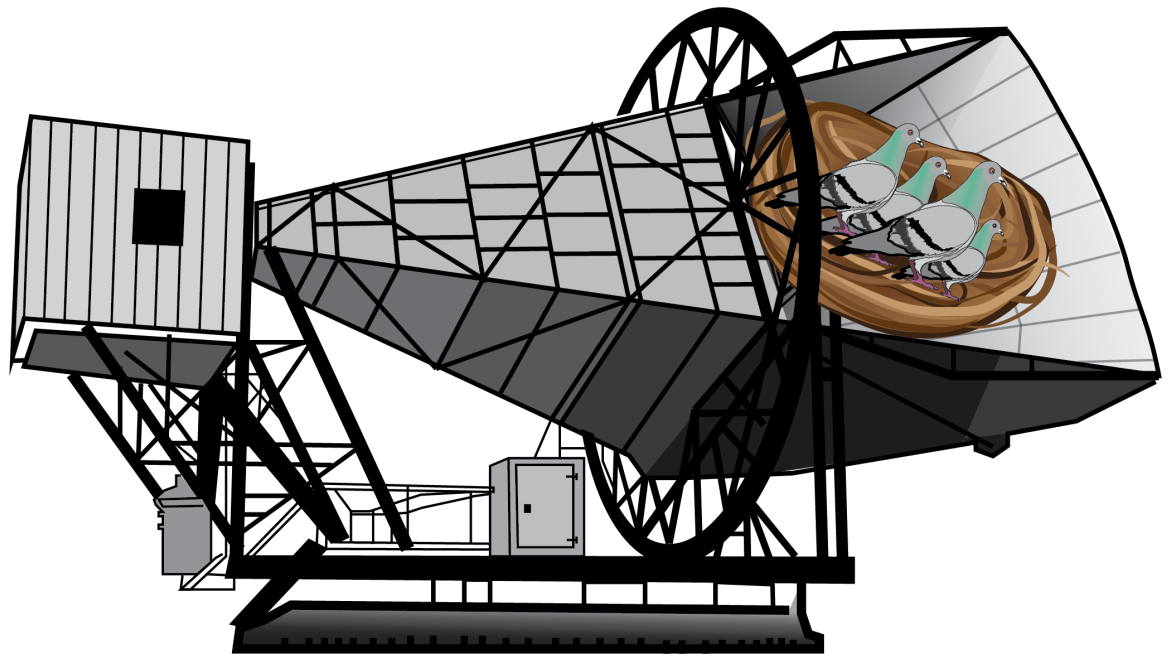
Pigeons in the Bell Labs radio horn antenna: the original instrumental setup used by Penzias and Wilson when they accidentally discovered the Cosmic Microwave Background radiation in 1966.

Taylor A. Baildon

baildon@umich.edu

ORCID iD: 0000-0002-7009-6154

ACKNOWLEDGEMENTS

TABLE OF CONTENTS

LIST OF FIGURES

LIST OF TABLES

LIST OF ABBREVIATIONS

GR General Relativity

BBN Big Bang Nucleosynthesis

CMB Cosmic Microwave Background

COBE Cosmic Background Explorer

WMAP Wilkinson Microwave Anisotropy Probe

DES Dark Energy Survey

DESI Dark Energy Spectroscopic Instrument

BOSS Baryon Oscillation Spectroscopic Survey

LSST Large Synoptic Survey Telescope

SDSS Sloan Digital Sky Survey

ACT Atacama Cosmology Telescope

ACTPol Atacama Cosmology Telescope Polarimeter

AdvACT Advanced ACTPol

SO Simons Observatory

LAT Large Aperture Telescope

LATR Large Aperture Telescope Receiver

SAT Small Aperture Telescope

SZ Sunyaev Zel'dovich

AR anti-reflection

OMT orthogonal mode transducer

PWV precipitable water vapor

UHMWPE ultra-high molecular weight polyethylene

HDPE high-density polyethylene

CAD computer aided design

TES transition-edge sensor

DR dilution refrigerator

LF low-frequency

MF mid-frequency

HF high-frequency

UHF ultra high-frequency

SQUID semiconducting quantum interference device

TDM time-division multiplexing

FOV field of view

BICEP Background Imaging of Cosmic Extragalactic Polarization

SPT South Pole Telescope

HWP half-wave plate

DFT discrete Fourier transform

FTS Fourier transform spectrometer

PIXIE Primordial Inflation Explorer

S/N signal-to-noise

LN2 liquid Nitrogen

RMS root mean square

SED spectral energy density

BSM beyond the Standard Model

HSC Hyper Suprime-Cam

ABSTRACT

Cosmic Microwave Background (CMB) experiments like Advanced ACTPol (Ad-vACT) and Simons Observatory (SO) seek to uncover the physics of the early Universe, just $\sim 10^{-32}$ seconds after its formation, and its evolution since. With just 6 parameters, the ΛCDM model of cosmology describes our Universe exceptionally well, but leaves some questions unanswered. The CMB can answer questions left unanswered by ΛCDM, including whether the early Universe underwent a period of inflation, if there are particles beyond the Standard Model, the sum of the neutrino masses, and the nature of dark matter and dark energy.

However, reaching the level of precision necessary to measure the signals in the CMB that can answer these questions is extremely difficult and requires unprecedented sensitivity, which presents a number of instrumental challenges. Additionally, measurements can be contaminated by polarized foregrounds such as dust and synchrotron emission. To recover the CMB signal, we must characterize and remove these polarized foregrounds with high precision, which requires multiple frequency bands and highly stringent instrument calibration. Previous experiments have never needed to calibrate to such extreme levels, but future experiments seeking to improve CMB measurements will require sub-percent level uncertainties in detector bandpass characterization. This will necessitate new calibration techniques.

In this thesis, I present my work towards achieving this unprecedented level of precision in detector bandpass calibration for AdvACT, SO, and future experiments such as CMB-S4, through analyzing current measurements and using novel techniques to

improve Fourier transform spectrometer (FTS) bandpass calibration, including characterizing the FTS transfer function, design improvements, and improved coupling optics. I will discuss the viability of these methods for future CMB experiments. This work will improve the frequency calibration needed to remove polarized foregrounds from CMB maps, which will enable CMB measurements that will advance our understanding of the fundamental physics of the Universe.

CHAPTER I

Introduction

1.1 ΛCDM

Albert Einstein created his Theory of General Relativity (GR) in 1915, marking the beginning of modern-day cosmology [1]. This new theory described gravitation as the interaction between matter and spacetime—how a massive body changes the geometric curvature of the spacetime surrounding it, causing nearby bodies to move in orbits rather than in straight lines (as would happen in a flat spacetime). GR provided an entirely new framework for understanding gravitation, one that went beyond the classical description of a mutual gravitational force to describe gravity as a property of spacetime.

The next series of discoveries provided the first evidence that our Universe began in a hot, dense state and expanded outward (the so-called "Big Bang"), and they formed the basis for our current model of our Universe, called "ΛCDM."

1.1.1 The development of the ΛCDM Model

In 1922, Alexander Friedmann derived an expanding universe solution to Einstein's theory, providing a theoretical framework for an expanding Universe. Edwin Hubble confirmed Friedmann's conjecture in 1929 when he found empirical evidence that our Universe is indeed expanding. He found that almost all galaxies that we

can observe appear to be moving away from us [2]. Hubble also discovered that the further away the galaxy was (the proper distance D), the faster its receding velocity v:

$$v = H_0 D. \tag{1.1}$$

Here H_0 is "the Hubble constant"—a parameter describing the current expansion rate of our Universe, which was estimated to be around $50 - 100$ km/s/Mpc in the 1930's [2]. Hubble's Law (Equation 1.1) led cosmologists to conclude that our Universe is expanding.

An expanding Universe was puzzling. Since we see our Universe filled with matter today, we would expect gravitation to pull masses towards each other over time. To account for the expansion, there must be some other form of energy driving it. They described this phenomenon as "dark energy". Einstein accounted for this expansion by adding a cosmological constant Λ in his equations—referred to in the acronym ΛCDM. Precision measurements of our Universe in the last decade have shown that dark energy makes up 68% of the energy density in the Universe [3].

The measured expansion of the Universe implied not only that our Universe would become larger in the future, but also that it was much smaller in the past. It suggested that if we were to trace our Universe's size far enough back in time, it would eventually converge to a single point. Cosmologists began theorizing that our Universe had a "start"—it has existed for a finite period of time and began as a hot and infinitely dense point. This hot, dense beginning has since been coined the "Big Bang": a blast of energy that formed our Universe all at once, followed by expansion and cooling over time. As the Universe expanded and cooled, subatomic particles were generated through fusion via Big Bang Nucleosynthesis (BBN) [4].

In the 1940s, Ralph Alpher and George Gamow started developing a theory for BBN, the primordial nucleosynthesis that generated the light elements (Helium,
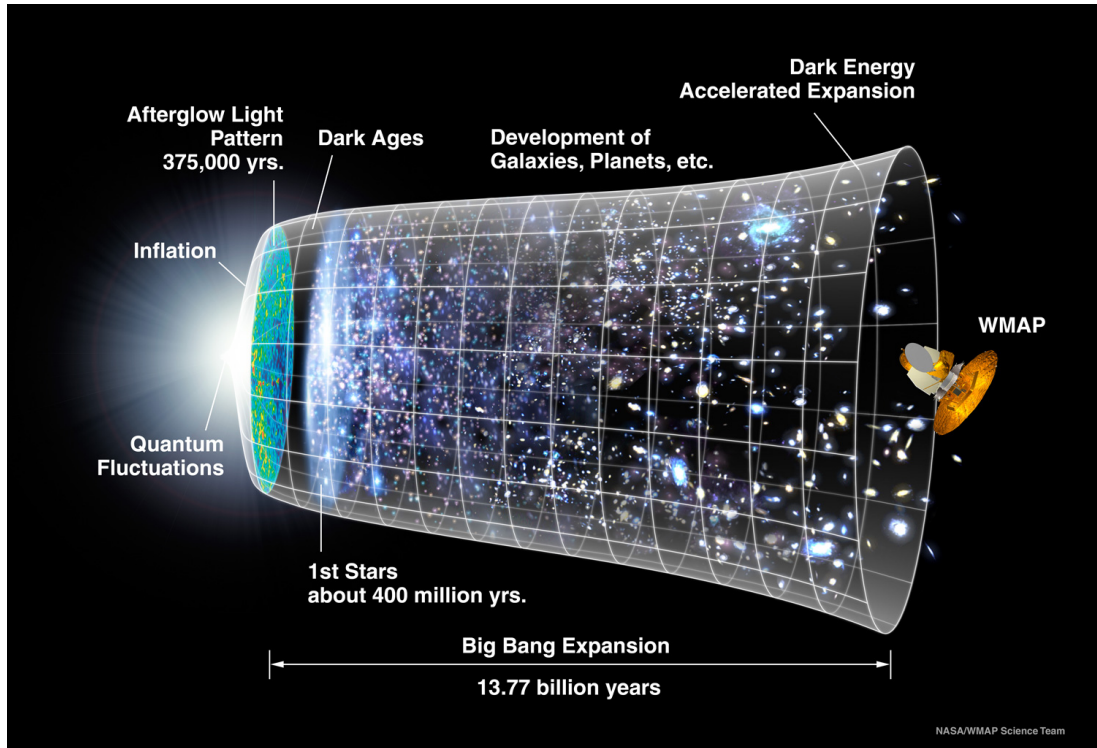
Figure 1.1: History of our Universe's evolution as described by ΛCDM cosmology and inflationary theory. Our Universe had a hot, dense beginning (left side), then underwent a period of rapid inflation, during which quantum fluctuations were blown up to large scales across the sky, seeding the structure we observe in the Universe today. We observe these fluctuations in the CMB, which was formed $\sim 375,000$ years after the Universe began. The Universe then entered a phase referred to as the "Dark Ages," where the slight density fluctuations—seeded by quantum fluctuations in the early Universe—allowed for gravitational interactions that would form the first gas clouds and eventually stars. The first stars formed around 400 million years after the Universe began, and over the course of the next ~ 13 billion years, galaxies, planets, and galaxy clusters started to form. Image from the NASA/WMAP Science Team.

Lithium, and their isotopes) that are abundant in our Universe today. They proposed that the initial conditions of the early Universe (~ 1 second after the Big Bang event) determined the ratio of neutrons and protons generated during BBN, and that the Universe was extremely hot, radiation-dominated, and almost perfectly homogeneous during this time. As the Universe expanded and cooled, deuterium and eventually other light nucleons were able to form [4]. BBN was found to not sufficiently explain the abundance of heavy elements that we observe today; however, later findings indicated that the heavy elements in our Universe were generated by stellar nucleosynthesis and supernovae. BBN is still considered a successful mathematical description of how primordial elements formed, and accounts for the relative abundances of Hydrogen and Helium we observe today (which together make up more than 99% of the baryonic matter in our Universe) [5].

In 1966, Arno Penzias and Robert Wilson made an accidental discovery that won them a Nobel Prize: there is a relic radiation surrounding us that was produced shortly after the Universe formed [6]. This further supported our Universe's hot, dense beginning; if it occurred, we would observe leftover radiation today that has cooled significantly with the expansion of the Universe, called the Cosmic Microwave Background (CMB) [7]. Later measurements found that the CMB is a nearly perfect blackbody (Figure 1.2) with a temperature around 2.73 K [8]. The blackbody curve provided proof that our Universe was once in thermal equilibrium, and has been cooling ever since—which we see as the 2.73 K blackbody radiation surrounding us today [9]. The CMB will be discussed in further detail in Section 1.3.

Today, we refer to these three key discoveries as "the three pillars of the Big Bang":

- The Universe is expanding.
- Big Bang Nucleosynthesis accurately accounts for the relative abundances of light elements in our Universe today.
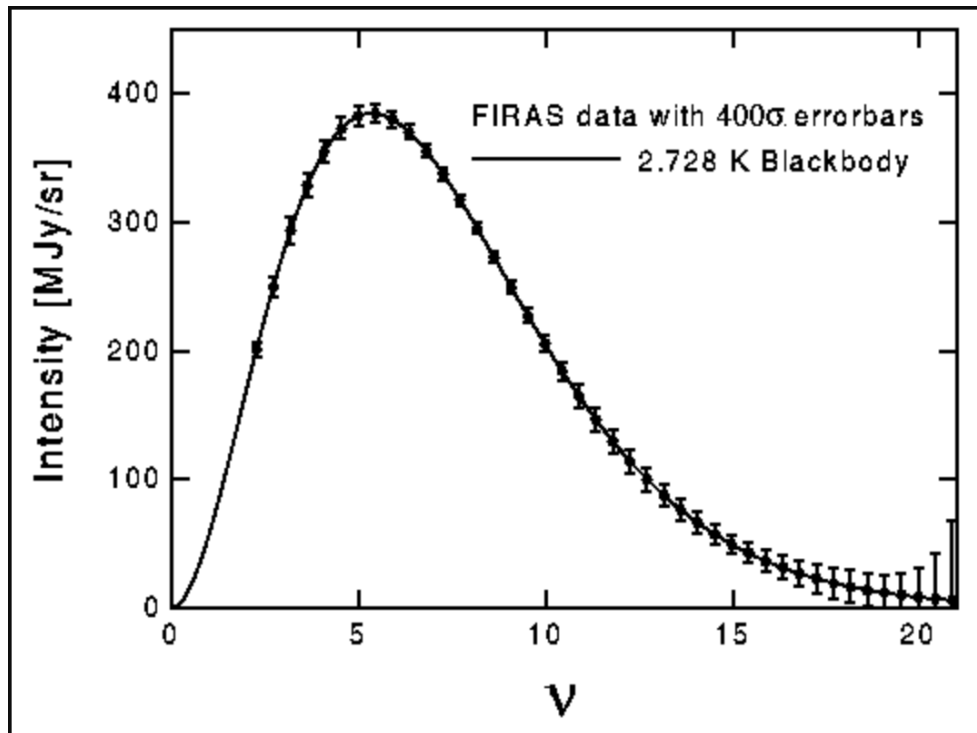
Figure 1.2: COBE measurement of the CMB blackbody spectrum, with 400σ error bars [8]. This data confirmed that the CMB is nearly a perfect blackbody at 2.728 K—indicating a hot thermal source that has cooled significantly during our Universe's expansion.

- The Cosmic Microwave Background is a relic radiation originating from the extremely hot conditions of the early Universe.

In addition to a hot, dense beginning and a dark energy component that drives the Universe's expansion, the -CDM in the ΛCDM model comes from "cold dark matter," which was first discovered in 1933 by Fritz Zwicky.

Zwicky found that galaxies in the Coma galaxy cluster were moving much faster than predicted by their masses, which were calculated from the luminosity of visible matter [10]. This led to the conclusion that galaxies contain much more matter than we can observe and are largely made up of "dark matter." Dark matter is thought to be made up of particles that interact primarily through gravitational interactions but do not interact with electromagnetic fields.

Later observations led by Vera Rubin in the 1970's confirmed Zwicky's hypothesis that galaxies are vastly made up of dark matter. Rubin's measurements of galaxy rotation curves—the velocity of stars and gas as a function of galactic radial distance—showed that the velocity of matter did not decrease as the radial distance passed the bulk of the galaxy's visible matter as predicted. Instead, the velocity appeared to remain constant with increasing radial distance (Figure 1.3), indicating that there must be additional mass at large radial distances [11].

To explain the structure formation that we observe in our Universe, this dark matter must be 'cold' (i.e. slow moving, unlike 'hot' relativistic particles). Slow-moving particles allow gravitational effects to dominate, causing the small density perturbations in the early Universe to coalesce into gas clouds and larger objects. Measurements today show that 26.8% of our Universe is composed of dark matter [13].

1.1.2 Six parameters of ΛCDM

The ΛCDM model describes our Universe very well and can be quantified by 6 key parameters: $h^2\Omega_b$, $h^2\Omega_c$, θ_*, A_s, τ, and n_s [3]. These parameters are outlined below.
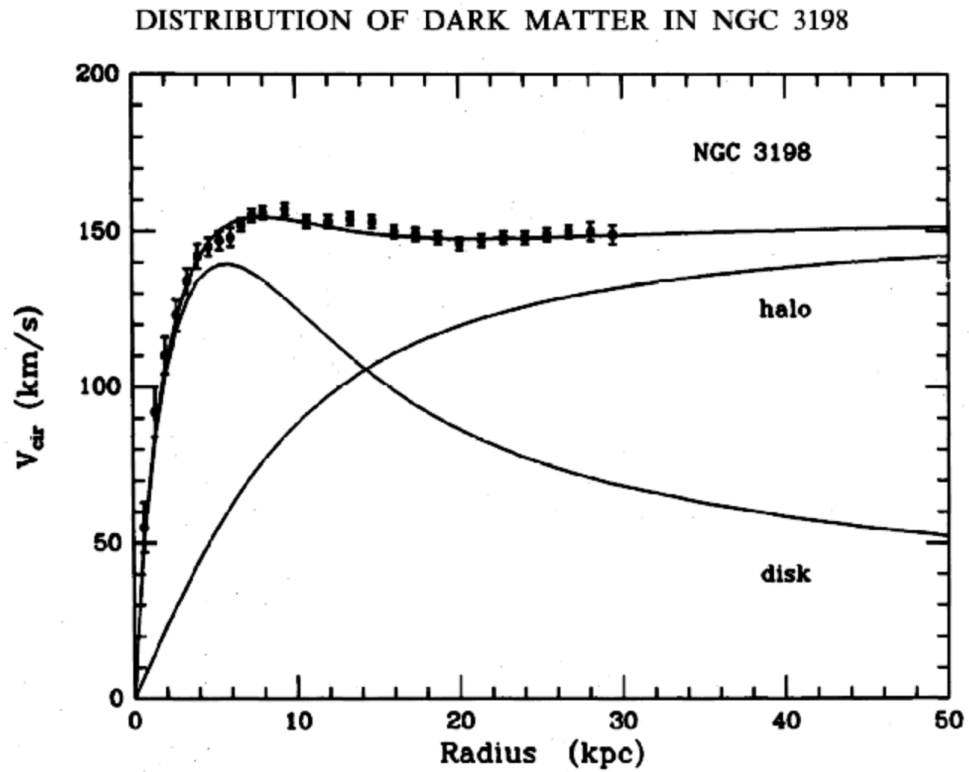
Figure 1.3: Measured galaxy rotation curve for NGC 3198, plotted alongside the curve predicted from the galaxy's distribution of visible matter (labeled 'disk'). The theorized 'halo' curve represents an undetected dark matter profile that would explain the discrepancy between NGC 3198's measured rotation curve and the predicted disk profile [12].

The constant h is related to the Hubble constant H_0 introduced in Equation 1.1:

$$H_0 \equiv h \times 100\,\mathrm{km/s/Mpc}, \tag{1.2}$$

and h is called the dimensionless Hubble constant.

The total energy density of the Universe is described by the density parameter Ω:

$$\Omega = \Omega_m + \Omega_r + \Omega_\Lambda, \tag{1.3}$$

where Ω_m, Ω_r, and Ω_Λ are the matter, radiation, and dark energy densities of the Universe, respectively. The matter density can further be broken down into energy densities of baryonic matter (Ω_b) and cold dark matter (Ω_c):

$$\Omega_m = \Omega_b + \Omega_c. \tag{1.4}$$

These quantities are combined into two independent quantities: $h^2\Omega_b$ and $h^2\Omega_c$, which are the physical baryon density parameter and the physical dark matter density parameter, respectively.

The next parameter θ_* describes the angular size of the acoustic horizon at the time the CMB radiation decoupled, and is defined as $\theta_* = r_*/D_M$, where r_* is the comoving sound horizon at recombination (quantifying the distance the photon-baryon perturbations can influence), and D_M is the comoving angular diameter distance that maps this distance into an angle on the sky [3]. The parameter θ_* is the angular scale of the first peak of the power spectrum 1.5, indicated in Figure 1.4. If our Universe is flat (zero geometric curvature), we would expect to see a peak in the spectrum at $\theta_* \approx 1°$ [14]. We indeed see this in the measurements: Planck estimates $\theta_* = (0.59643 \pm 0.00026)°$ with 68% confidence, corresponding to $\ell \approx 300$ [3] (note: Figure 1.4 shows Wilkinson Microwave Anisotropy Probe (WMAP) data from

2007 for illustration purposes, not the most recent Planck measurements). Planck's measurement for θ_* is consistent with a very flat Universe.

The power spectrum $p(k)$ of the initial scalar fluctuations is given by:

$$p(k) = A_s \left(\frac{k}{k_i} \right)^{n_s - 1}. \tag{1.5}$$

Here k is the comoving wavenumber, k_i is the initial comoving wavenumber, A_s is the initial amplitude of scalar fluctuations, and n_s is the scalar spectral index. The initial amplitude of scalar fluctuations A_s quantifies how the CMB temperature varies across the sky. The scalar spectral index n_s describes how scalar fluctuations vary with scale. A value of $n_s = 1$ would correspond to scale-invariant fluctuations; Planck currently estimates $n_s = 0.965 \pm 0.004$ with 68% confidence [3].

The last parameter, τ, is the optical depth at reionization—the first stars, quasars, and dwarf galaxies around $z = 8$ that ionized neutral hydrogen, leaving an imprint on the CMB. τ gives us a measure of the line-of-sight free-electron opacity of the CMB, which can inform theories on how the first stars and galaxies formed.

The ΛCDM model makes several assumptions about the nature of our Universe: it is flat ($\Omega = 1$); dark energy can be treated as a cosmological constant, with an equation of state $w = -1$; the sum of the masses of neutrino species is fixed; the running of the scalar spectral index $dn_s/d\ln k = 0$; and the effective number of relativistic species $N_{\text{eff}} = 3.046$, which is the three flavors of neutrinos plus their interactions.

1.1.3 Shortcomings of ΛCDM

While ΛCDM is currently our best working cosmological model, it fails to explain some crucial findings. Our Universe would have to have very finely tuned initial conditions to explain what we observe today. There is a very small probability that
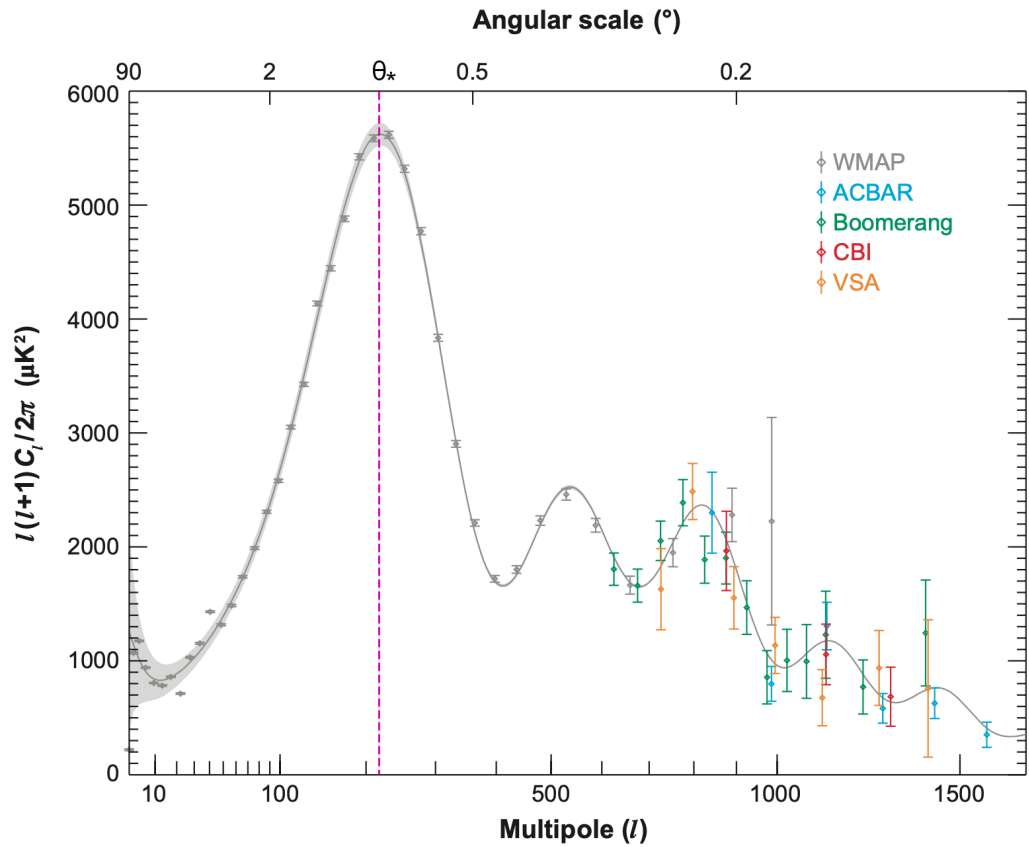
Figure 1.4: The CMB temperature power spectrum, with the parameter θ_* indicated. Data from WMAP [15] and high-ℓ data from other experiments are shown, in addition to the best-fit cosmological model to the WMAP data [9].

each cosmological parameter would be tuned to just the right value and work together with the other parameters to form our Universe. ΛCDM offers no explanation for how or why these values would be finely tuned to the values we measure today.

The flatness problem

Our Universe is nearly perfectly flat, with $\Omega_0 = 0.9940 \pm 0.0148$ [3, 16], making the deviation of the density parameter from one $|1 - \Omega_0| \leq 0.2$. When our Universe was dominated by radiation and matter in its early stages, the density parameter evolved at the rate

$$|1 - \Omega(t)| = \frac{(1 - \Omega_0)a^2}{\Omega_{r,0} + a\Omega_{m,0}}, \tag{1.6}$$

where a is the scale factor of the Universe at time t, and $\Omega_{r,0}$ and $\Omega_{m,0}$ are the present-day densities of radiation and matter, respectively [14]. If we extrapolate $\Omega(t)$ backwards to the time of BBN, when $a \approx 3.6 \times 10^{-8}$, we find that

$$|1 - \Omega(t_{\text{BBN}})| \leq 3 \times 10^{-14}.$$

If we extrapolate as far back as we can, to the Planck time at $t_p \approx 10^{-44}$ s and $a \approx 2 \times 10^{-32}$, we find that the deviation of the density parameter from one is

$$|1 - \Omega(t_p)| \leq 1 \times 10^{-60}, \tag{1.7}$$

meaning $\Omega(t_p)$ is extraordinarily close to one [14].

ΛCDM doesn't address how or why our Universe would be so flat. Anthropic explanations often rely on the existence of a multiverse, which cannot be empirically falsified. We could consider this tiny deviation to be a coincidence—that $\Omega(t_p)$ could have had any value, and it just happened to deviate from one by 10^{-60}. However, a coincidence at the level of one part in 10^{60} is extremely unlikely [14]. This leaves no
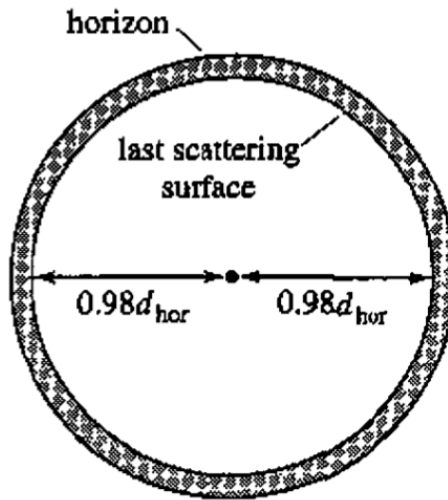
Figure 1.5: The proper distance to the "surface of last scattering"—the time the CMB was released and the Universe became transparent. This distance is 98% of the distance to the horizon (d_{hor}), or the edge of the observable Universe [14].

satisfying explanation for why our Universe is nearly perfectly flat.

The horizon problem

We observe an extremely uniform temperature across the entire sky. ΛCDM alone predicts that the causal distance is about 100 comoving Mpc, meaning light from the Big Bang era could only travel 100 comoving Mpc before recombination. This distance corresponds to a ~ 2 degree patch on the sky today; objects or particles that have more than 2 degrees of separation on the sky today are therefore out of causal contact with one another, and cannot exchange information [14]. However, when we observe the CMB, we see the exact same temperature all the way across the sky—only varying by $\sim 10^{-5}$ Kelvin!

The Universe's expansion history as described by ΛCDM, including the conditions necessary for BBN, would not allow for distant regions to reach thermal equilibrium. This is referred to as "the horizon problem" because patches outside each other's particle causal horizon appear to be in thermal equilibrium.

The magnetic monopole problem

We have never observed magnetic monopoles anywhere in the Universe. Modern particle theory predicts the existence of magnetic monopoles—the magnetic points analogous to electric point charges—and that the extremely hot conditions of our early Universe would produce a large quantity of stable magnetic monopoles that should be observable today.

Dark energy and dark matter

ΛCDM depends on the existence of a mysterious "dark energy" and elusive "dark matter" particles, yet it does not explain their nature or their origin.

Initial density fluctuations

The structure in the ΛCDM Universe also depends on the existence of density perturbations or fluctuations in the early Universe; however, it does not explain the source of these fluctuations.

1.2   Inflation

Inflationary theory offers solutions to several of the problems that ΛCDM leaves open [17]. The theory introduces an inflationary epoch shortly after our Universe's formation ($t \sim 10^{-32}$ s) during which our tiny Universe underwent an exponential expansion. This expansion, called inflation, happened before recombination and reionization, and our Universe has continued to expand at a much slower rate ever since [9].

Inflation solves the flatness problem because it describes a spacetime with initial curvature that expands so rapidly during the inflationary period, that it becomes almost perfectly flat [17]. This would give the initial conditions necessary to allow our Universe to look extremely flat 14 billion years later today instead of quickly
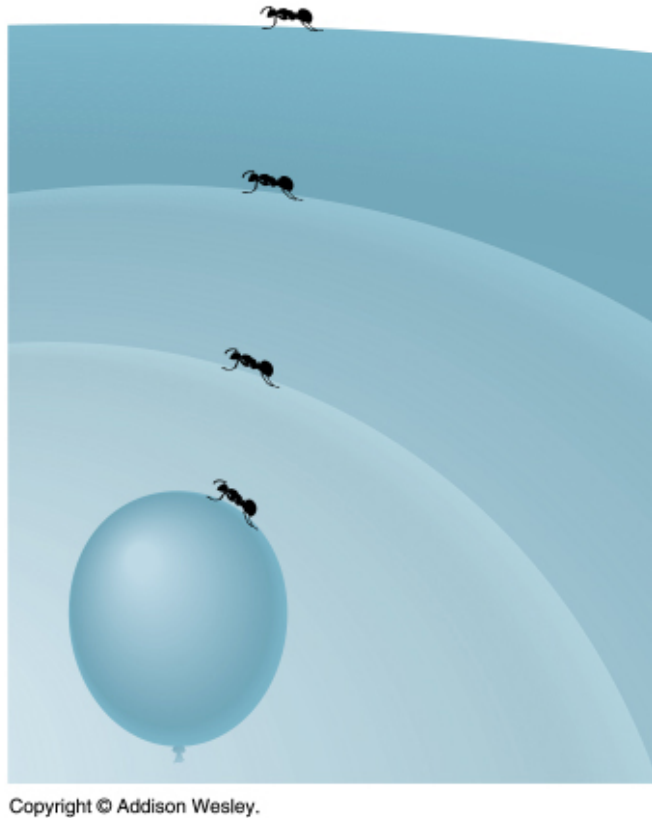
Figure 1.6: Illustration of flatness caused by vast expansion of a curved surface. If our Universe started with some curvature, represented here as a 2-dimensional curved surface, inflation would allow for this curvature to appear nearly perfectly flat today, after significant expansion of spacetime [18].

ending in a Big Crunch or Big Rip.

The horizon problem also disappears because inflation describes an extremely dense, tiny, and hot universe that is able to reach thermal equilibrium in its very early stages before space expands superluminally. The superluminal expansion of space during inflation allows for regions that were previously in causal contact to fall out of causal contact, explaining why we see a nearly homogeneous temperature across the sky [17].

Inflation also provides an explanation for the magnetic monopole problem: magnetic monopoles were indeed created during the very early stages of our Universe, but their density is less than one per observable universe because of the large-scale

expansion during inflation [17].

The origins of the perplexing large-scale structure that we observe in our Universe can also be explained by inflation. The rapid expansion of spacetime during inflation causes quantum fluctuations to expand to cosmological scales, forming the seeds of structure that gravitationally coalesce over time into the structure we observe today [19].

Inflation would have left a signature imprint in the linear polarization of the CMB. The polarization in the CMB can be mathematically decomposed into two types: E-modes and B-modes. E-modes are shown in Figure 1.7; they are so named because they have even parity (no curl), analogous to an electric field $\vec{E}$. It follows then that B-modes, also shown in Figure 1.7, have odd parity (no divergence) like the magnetic field $\vec{B}$ [20]. Scalar perturbations are sourced by density perturbations and can only produce E-modes, so we expect to see E-modes in the CMB. If inflation occurred, the rapid expansion of space would have created primordial gravitational waves. These gravitational waves would have acted as tensor perturbations, and would have created E-modes and B-modes in equal quantities that peak on ∼degree angular scales on the sky today [21, 22].

The amplitude of the B-mode signal measured from the CMB is quantified by the tensor-to-scalar ratio r, defined as

$$r \equiv \frac{\Delta_t^2}{\Delta_t^2},\tag{1.8}$$

where Δ_t and Δ_s are the tensor and scalar power spectra, respectively. We can describe inflation as being driven by a scalar "inflaton" field, with a potential $V(\phi)$. If we assume $\Delta_s^2 \simeq 10^{-9}$ based off CMB E-mode measurements[1], we find

$$V^{1/4} \simeq \left(\frac{r}{0.01}\right)^{1/4} 10^{16} \text{GeV}.\tag{1.9}$$

---

[1]Personal correspondence with Dragan Huterer
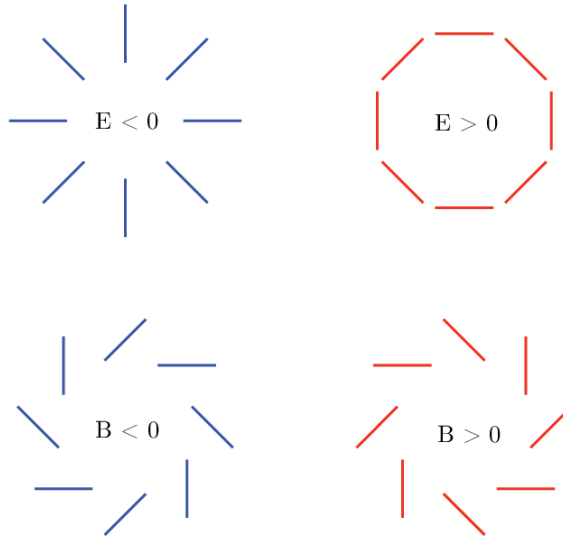
(a) E-mode (even parity) and B-mode (odd parity) polarization [23]. Both polarization modes possess a handedness, corresponding to positive and negative values of E and B.
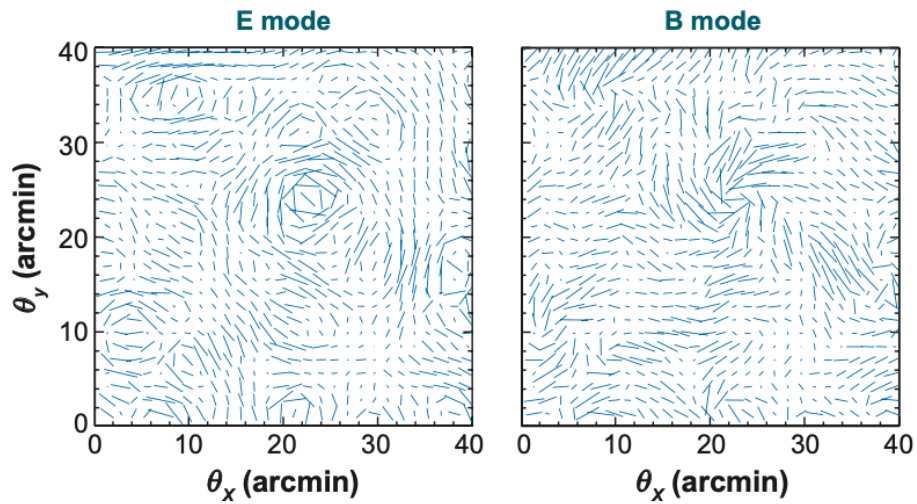
(b) E-mode and B-mode spatial polarization patterns. The length of the lines represents the degree of polarization, while their orientation gives the direction of maximum electric field. Frames courtesy of W. Hu [9].

Figure 1.7: Illustrations of E-mode (curl-free) and B-mode (divergence-free) photon polarization.
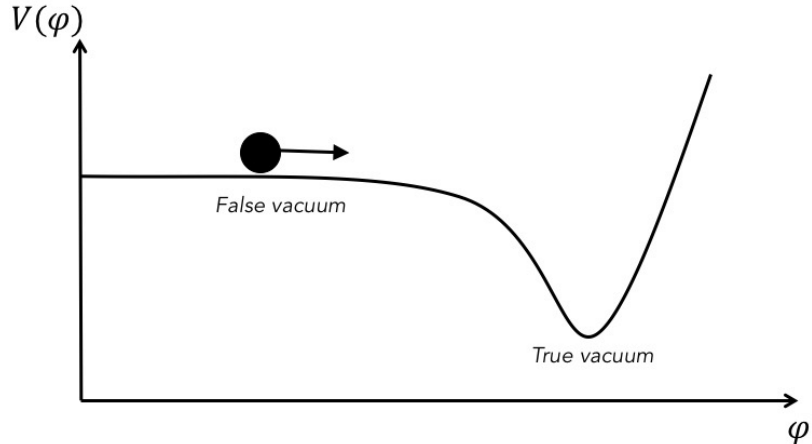
Figure 1.8: Example of one inflationary model (the slow roll scenario) that describes the Universe as starting in a false vacuum. Here we see the potential energy V of the inflaton field ϕ. This "slow roll" model asserts that our Universe slowly transitions to a true vacuum in its early stages, providing an energy mechanism for inflation [24].

The amplitude of the B-mode signal Δ_t^2 thereby sets the energy scale of inflation, which is proportional to the potential V [20].

There are many models of inflation (e.g. Figure 1.8); the most natural models of inflation predict $r \sim 0.01$. Values of $r < 0.001$ would rule out the most natural, widely studied inflationary models; measuring or placing upper limits on r can therefore help significantly narrow down the number of viable models of inflation.

1.3 Precision Cosmology with the CMB

The Cosmic Microwave Background is the relic radiation leftover from the formation of our early Universe. We observe it at a nearly uniform 2.733 K across the sky. Observations of the CMB allow us to test the assumptions made by ΛCDM and search for new physics beyond the Standard Model. Measurements of the CMB can tell us how flat our Universe is (Ω), if dark energy is a cosmological constant ($w = -1$), if inflation occurred ($r > 0$), the sum of the mass of neutrinos (Σm_ν), if there are additional relativistic particles ($\Delta N_{\text{eff}} \geq 0.027$), and the nature of dark matter and dark energy [25].

1.3.1 CMB Measurements

Theoretical and measured temperature anisotropies (TT), E-mode (EE), and B-mode (BB) power spectra are shown in Figure 1.9. Power spectra of the CMB are made by breaking down the sky into spherical harmonics $Y_{\ell m}(\theta, \phi)$ and binning the power at each angular scale [9]. Large ℓ therefore correspond to small angular sizes on the sky, while small ℓ correspond to large angular scales. CMB experiments can further improve their constraints on cosmological parameters by combining with other data sets like optical large scale structure surveys (e.g. DES).

Temperature spectrum

The CMB temperature anisotropies are the small fluctuations in power across the sky that remain after the average temperature of the CMB is removed, and they can be expanded into spherical harmonics $Y_{\ell m}$:

$$\frac{\delta T}{T}(\hat{n}) = \sum_{\ell=2}^{\infty} \sum_{m=-\ell}^{\ell} a_{\ell m}^{TT} Y_{\ell m}, \tag{1.10}$$

where $a_{\ell m}^{TT}$ are coefficients [9]. The monopole term $\ell = 0$ is not included here because the expansion is about the mean temperature, which is the monopole. We also skip the dipole term $\ell = 1$ since it is caused by our own motion through the CMB rest frame and is not a primordial signal. The coefficients $a_{\ell m}^{TT}$ can be determined from the full-sky temperature anisotropy map using orthogonality of spherical harmonics,

$$a_{\ell m}^{TT} = \int \frac{\delta T}{T}(\hat{n}) Y_{\ell m}^{*}(\hat{n}) d\Omega, \tag{1.11}$$

and because m ranges from $-\ell$ to ℓ, there are $2\ell + 1$ coefficients $a_{\ell m}^{TT}$ for each ℓ. Inflation predicts that the temperature fluctuations $\frac{\delta T}{T}$ have a gaussian distribution, so the coefficients $a_{\ell m}$ will also be a gaussian distribution about zero (the mean), with
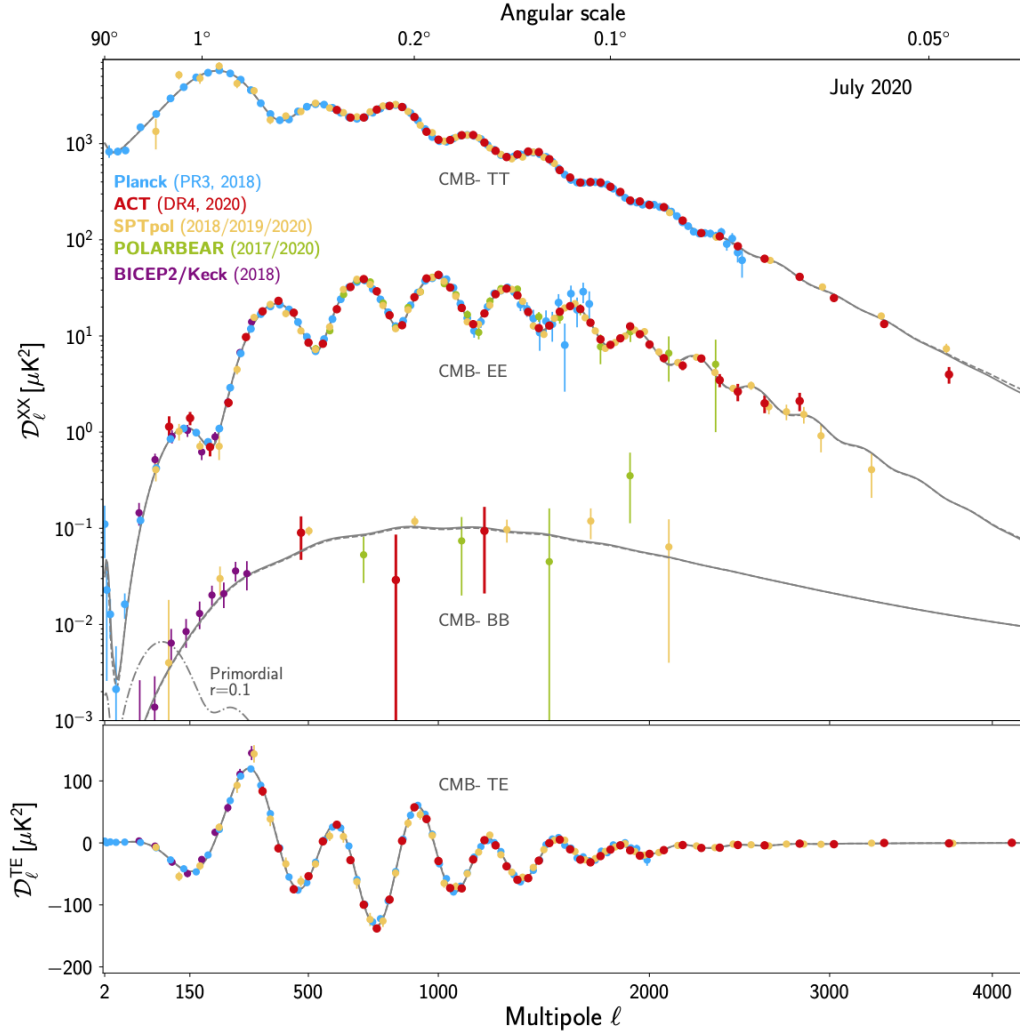
Figure 1.9: Recent temperature anisotropy and polarization power spectra (measured and projected) of the CMB, from AdvACT and other current experiments [26]. The primordial B-mode spectrum with $r = 0.1$ is shown as the dot-dashed line. We see the first peak of the TT spectrum near $1°$ as predicted for a flat Universe.

a variance C_ℓ. If we assume statistical isotropy, then C_ℓ does not depend on m, and can be estimated by [9]

$$C_\ell^{TT} = \frac{\sum_{m=-\ell}^{\ell} |a_{\ell m}^{TT}|^2}{2\ell + 1}. \tag{1.12}$$

The smaller peaks and troughs in the TT spectrum (Figure 1.9) are signatures of oscillations in the primordial plasma. These oscillations were caused by competing forces in the early Universe: the inward gravitational pull from dark matter vs. the outward pressure from hot baryonic matter [9].

Each peak and trough carries information about the contents of the Universe. Small perturbations in Σm_ν and $N_{\rm eff}$ would change the phase and amplitudes of these peaks, and the relative abundance of dark matter to baryonic matter can be found using the ratio of odd to even peaks. Different values of Ω would have different effects on our Universe's geometry: $\Omega < 1$ indicating a "closed universe" (spherical geometry), $\Omega > 1$ indicating an "open universe" (negative curvature), and $\Omega = 1$ indicating a flat universe. The value of Ω sets the angular scale of the first peak. We expect the power spectrum to peak around $1°$, or $\ell \sim 100$, for a flat Universe, and in the measured TT spectrum we indeed see a peak at an angular scale of $\sim 1°$ [26]. At small angular scales, sources like galaxy clusters add an additional contribution to the power spectrum, so the signals from the sources must be masked to recover the small angular scales of the temperature spectrum.

E-mode spectrum

The CMB EE spectrum can also be expanded into spherical harmonics with variance

$$C_\ell^{\rm EE} = \frac{\sum_{m=-\ell}^{\ell} |a_{\ell m}^{\rm EE}|^2}{2\ell + 1}, \tag{1.13}$$

where $a_{\ell m}^{\rm EE}$ are the E-mode spectrum coefficients. As we can see in Figure 1.9, the EE spectrum has many features that resemble those in the TT spectrum; this is

because density perturbations in the early Universe not only source E-modes, they also create temperature anisotropies in CMB photons at the time of decoupling. The cross-correlated TE spectrum (also seen in Figure 1.9) reflects the similarities between the two spectra.

Like the temperature spectrum, the high-ℓ region is sensitive to the parameters N_{eff} and Σm_ν. Higher N_{eff} and Σm_ν would result in suppressed structure formation, changing the angular scale of both EE and TT fluctuations [27].

The tail of the EE spectrum is not dominated by sources as TT is since most sources (galaxies and clusters) are largely unpolarized. Since the high-ℓ EE spectrum isn't dominated by sources, we can get cleaner lensing signals (caused by large-scale structure) from the tail of the EE spectrum.

B-mode spectrum

We can again decompose the power spectrum into spherical harmonics for the BB signal with variance

$$C_\ell^{\text{BB}} = \frac{\sum_{m=-\ell}^{\ell} |a_{\ell m}^{\text{BB}}|^2}{2\ell + 1} \tag{1.14}$$

and B-mode spectrum coefficients $a_{\ell m}^{\text{BB}}$. The BB spectrum is expected to have two main components: a contribution from gravitational lensing from large-scale structure at small angular scales and the primordial B-mode signal from inflation at roughly degree angular scales. Just like the EE spectrum, the BB spectrum is impacted by lensing from large-scale structure in the Universe. The lensed B-mode signal is even cleaner than the E-mode channel because there are no other contributions to the B-mode spectrum on these scales. The highly sought-after BB spectrum would reveal the energy scale of the primordial B-mode signal. It would provide a measurement of the tensor-to-scalar ratio r, allowing us to narrow down the pool of working cosmological models as discussed in Section 1.2. This signal can be contaminated by the lensed B-mode signal, so characterizing the full B-mode signal across many angular scales is

important for recovering a measurement of r.

Sunyaev Zel'dovich effect

Galaxy clusters can be detected in the CMB through the Sunyaev Zel'dovich (SZ) effect. The SZ effect is a characteristic distortion of the true CMB temperature signal in frequency caused by inverse Compton scattering. High-energy electrons from the hot gas that comprises the majority of mass in galaxy clusters scatter CMB photons, giving them an energy boost as they stream through [28]. The inverse Compton scattering creates a temperature decrement at 90 GHz and 150 GHz, as these low-energy photons are scattered to higher energies, while we see a temperature increment at 270 GHz from the scattered photons that received an energy boost [29]. There is a null (no increment or decrement) at 220 GHz . Clusters thus show up as cold (or colder) spots in CMB maps at 90 GHz and 150 GHz and hotter spots on the sky at 270 GHz.This characteristic frequency variation can be used to distinguish galaxy clusters from other sources on the sky.

CMB surveys in the next generation expect to deliver cluster catalogs with $\sim$ 100,000 galaxy clusters [25]. Because galaxy clusters are the largest structures in the universe and formed relatively recently, in the matter- and dark energy-dominated eras of our Universe's history, they are highly sensitive probes of the nature of dark matter and dark energy.

1.4 Measurement Challenges

Current CMB experiments (such as ACT [31], POLARBEAR [32], SPT [33], and BICEP/Keck [34]) seek to measure the E-mode, B-mode, and temperature anisotropy power spectra. As shown in Figure 1.9, the B-mode signal is orders of magnitude smaller than the E-mode signal. Measuring such a weak signal requires extremely sensitive instruments. The sensitivity of a given CMB survey can be roughly esti-
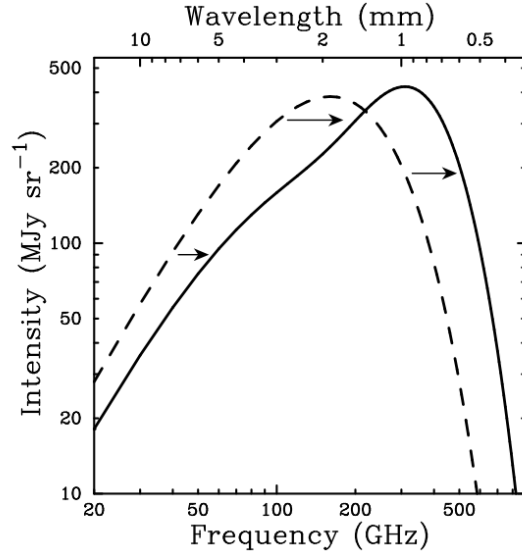
Figure 1.10: The CMB blackbody spectrum undistorted (dashed line) and distorted (solid line) by the thermal SZ effect. The inverse Compton scattering boosts lower energy CMB photons to higher energies, causing a shift in the CMB power spectrum to higher frequencies [29].
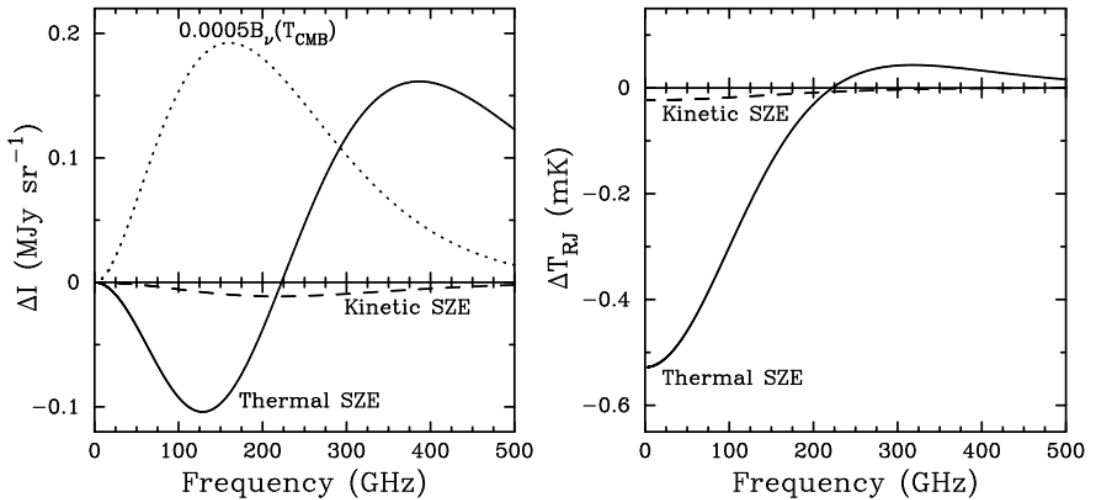
Figure 1.11: The temperature distortions caused by the thermal SZ effect are shown above. Lower frequencies like 90 GHz and 150 GHz experience a temperature decrement, ~ 220 GHz has a null, and 270 GHz has an increment [30]. Inverse Compton scattering occurs when CMB photons pass through the hot gas in galaxy clusters, boosting lower-energy photons to higher frequencies.

mated by the map depth, which is defined as

$$\text{Map Depth} = \text{NET}\sqrt{\frac{A}{N_{\text{dets}}t}}. \tag{1.15}$$

Here, "NET" is the effective noise equivalent temperature of a single detector in $\mu\text{K}\sqrt{s}$, A is the survey area in arcmin^2, N_{dets} is the number of operational detectors, and t is the survey observation time in seconds. The map depth is given in $\mu\text{K-arcmin}$. Per detector, NETs are typically on the order of several hundred $\mu\text{K}\sqrt{s}$ for 27-150 GHz detector bands, and on order ~ 1000 $\mu\text{K}\sqrt{s}$ for 220/270 GHz detector bands, though precise numbers are instrument-specific. Only minor improvements to per-detector NETs can be made with instrumental design, and the area of the sky observed is set by the observation goals for a given experiment. Thus, the survey observation time and the number of detectors N_{dets} observing the sky must be maximized to improve the sensitivity. The primary method to gain sensitivity in future experiments will be through scaling up the number of detectors by factors of $\sim 10 - 100$, which presents a technological challenge.

Another challenge facing ground-based CMB observations is the emission from our atmosphere, which changes over time. To reduce the overall impact of the atmosphere on measurements, we choose observing sites in high, dry places where the atmosphere is thinnest and has low water vapor, such as the South Pole and the mountainous Atacama Desert. Even in these extreme conditions, there will be atmospheric emission, which can be patchy and changing over time. This creates slowly varying correlated noise in measurements ($1/f$ noise) [35]. Polarization modulators modulate the incoming polarization from the sky, separating the CMB polarization from the largely unpolarized atmosphere, which enables measurements at larger angular scales where the $1/f$ noise dominates the signal [36].

Other sources in our Universe produce polarized light at microwave frequencies

that can be confused as E-mode and B-mode signals; these sources dominate the small CMB B-mode signal by several orders of magnitude. The biggest sources of polarized foreground emissions are dust and synchrotron emission [9], and these foregrounds must be removed with high precision and accuracy to realize a true measurement of the CMB B-mode signal. As shown in Figure 1.12, both dust and synchrotron emission have spectra in our intended observing frequency range (GHz–THz) that are distinct from that of the CMB [37]. Synchrotron emission dominates at low frequencies, while polarized dust emission dominates at high frequencies. We therefore design our experiments to cover a broad frequency range, so we can characterize these foreground signals accurately and remove them. Modern experiments such as the Advanced ACTPol (AdvACT) Experiment and Simons Observatory (SO) utilize multichroic detectors to fit multiple detector frequency bands in the same focal plane area. Mostly dichroic detectors with two frequency bands per pixel are used, because we are limited by the capabilities of anti-reflection (AR) coatings on the filters and lenses. It is extremely difficult to create an AR coating that transmits with high efficiency across more than 3 frequency bands, and dichroic detectors are the most practical for most uses. Ultimately, we must be able to define our detector bandpasses with the highest precision possible so we can fully characterize and carefully remove these polarized foregrounds.
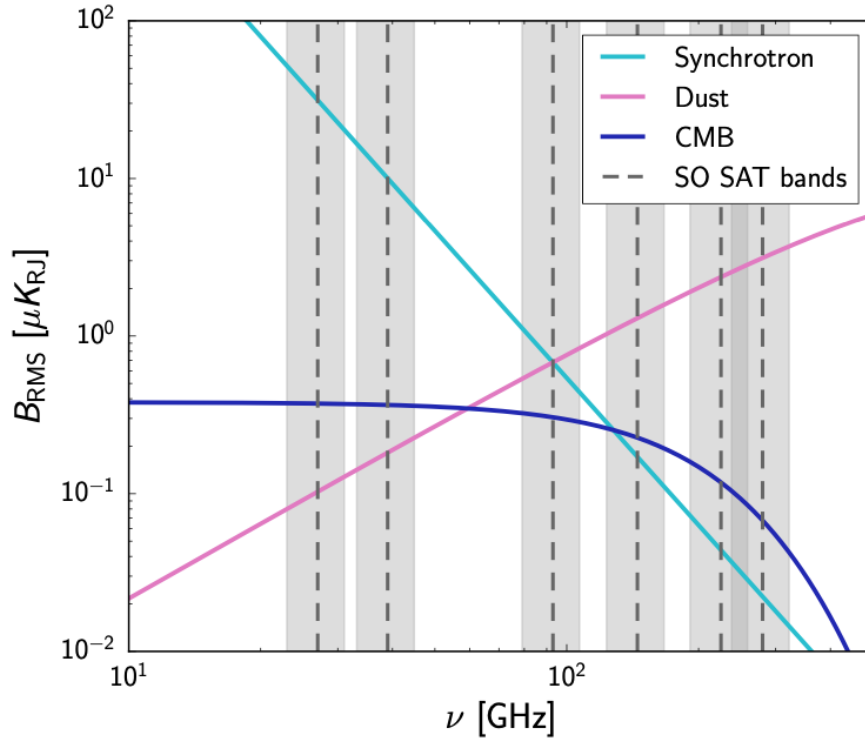
Figure 1.12: Dominant polarized foregrounds in CMB measurements, plotted with the SO SAT bandpasses and the expected CMB signal. Dust and synchrotron emission are the largest sources of polarized foregrounds, and they dominate the CMB signal by several orders of magnitude. Characterizing these foregrounds across a wide frequency range will help accurately remove them from our polarization maps, enabling the recovery of primordial B-modes [38].

CHAPTER II

Instruments

The Advanced ACTPol (AdvACT) Experiment is a current-generation experiment measuring the temperature and polarization of the CMB with $\sim 5,000$ detectors and coverage from 27-220 GHz. Simons Observatory (SO) is a next-generation experiment that will have $\sim 60,000$ detectors measuring the temperature and polarization of the CMB from 27-270 GHz. SO is scaling up by an order of magnitude in detectors compared to AdvACT, and CMB-S4 will scale up an order of magnitude further to $\sim 500,000$ detectors. The work in this thesis focuses largely on current measurements with AdvACT and specific advancements for SO. In this chapter I describe the site chosen for the AdvACT and SO telescopes and each experiment's observation strategy, optical design, cryogenic receiver system, focal plane, and readout system.

2.1 Site

AdvACT and SO are both positioned on top of Cerro Toco in the Atacama Desert in Northern Chile, at an altitude of 5,190 m. The thin, dry atmosphere is ideal for ground-based astronomical measurements, and at a latitude of 23° S, this location also allows for access to ~20,000 square degrees of the sky. This sky coverage enables both experiments to overlap with surveys at other wavelengths, including BOSS [39], DES [40], DESI [41], HSC [42], and LSST [43]. Access to a large area of the sky is

also critical for improving measurements of the CMB power spectrum at high-ℓ as the large sky area enables more samples of these small angular scales, reducing the statistical error on the measurements.

The location also allows for cross-linking, which helps mitigate polarization systematic effects. Cross-linking is the technique of observing the same patch of sky using different scan directions. AdvACT and SO achieve this by observing the same patches of sky as they rise and set. This technique helps to separate instrumental polarization effects from the polarization we observe on the sky, and is an advantage that CMB experiments at the South Pole lack [44].

The site's high altitude and low precipitable water vapor (PWV) are ideal for millimeter wavelength transmission. Water in the atmosphere is a large source of millimeter wave absorption. A dry climate has less water in the atmosphere, and the atmosphere is much thinner at high altitudes. Earth's atmosphere absorbs millimeter wavelengths at certain frequencies, creating atmospheric transmission "windows" that are optimal for ground-based CMB observations, shown in Figure 2.1 [45]. AdvACT and SO design our detector bandpasses to observe in frequency ranges with the highest atmospheric transmission. However, higher PWVs lead to lower transmission efficiency, even within the transmission windows where our bandpasses are observing, as seen in Figure 2.2. As such, the low PWV in the Atacama desert is hugely beneficial to ground-based CMB observations.

Even with a thin atmosphere and low PWV, a fluctuating atmosphere and PWV will change the transmission efficiency, illustrated in Figure 2.2. This fluctuating transmission efficiency leads to variations in our total detector bandpasses, which includes both the sky transmission and the transmission of the entire instrument (i.e. the telescope, receiver, focal plane, etc.) [45]. We therefore must characterize these bandpass variations with precision to account for the effects they will have on our CMB measurements.
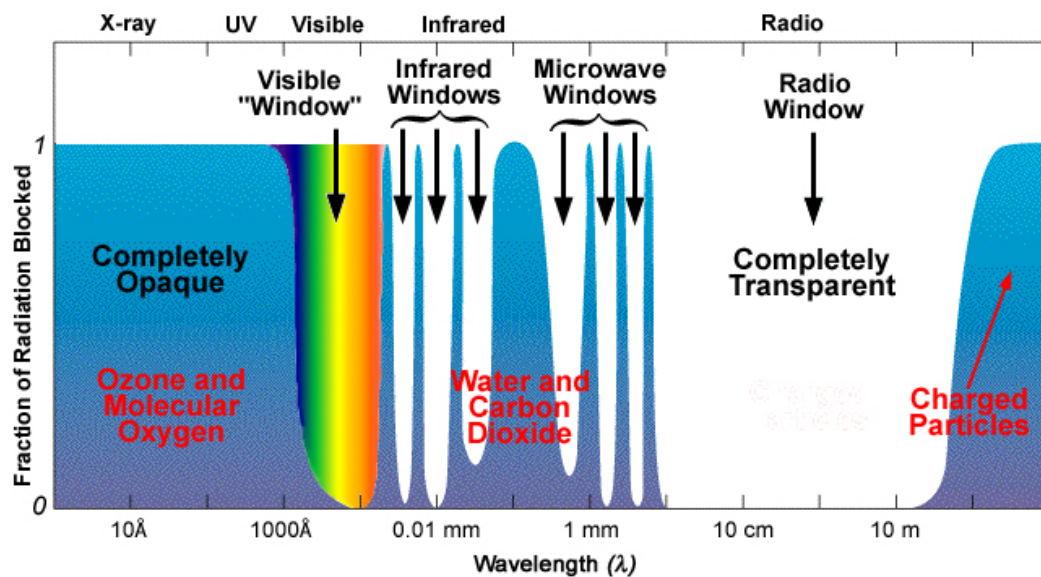
Figure 2.1: Atmospheric windows [46]. Incoming radiation is absorbed by particles in our atmosphere, and because different molecules absorb different wavelengths, some parts of the spectrum are completely opaque to observations. AdvACT and SO observe within the microwave windows—in the $20 - 300$ GHz range where the CMB signal is strong. The molecules and particles responsible for absorption are noted in their respective frequency ranges.
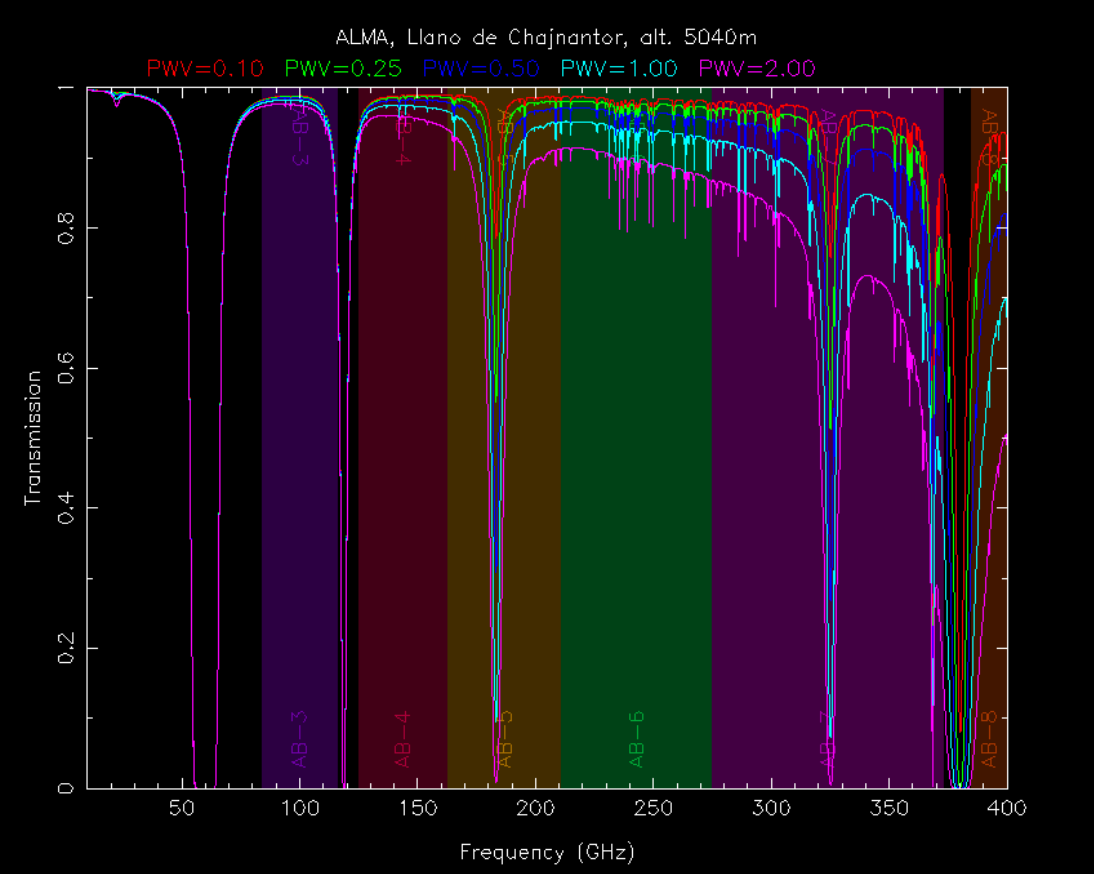
Figure 2.2: Simulated atmospheric transmission with varying PWV [47]. We see the highest transmission efficiency for the lowest PWV values. High PWV values can significantly reduce CMB signal transmission, so we choose extremely dry locations for ground-based observations.

2.2 Advanced ACTPol

The Atacama Cosmology Telescope (ACT) is a 6 meter off-axis Gregorian design with arcminute resolution. ACT was designed to take high angular resolution measurements across approximately half the sky, targeting CMB science in the $200 < \ell < 3000$ range [48]. This range enables both high-resolution CMB science and measurements of the primordial B-mode signal.

The first ACT receiver was fielded in 2008 (called the Millimeter Bolometer Array Camera, or MBAC); it observed the CMB temperature at 148, 218, and 277 GHz. The second generation experiment, Atacama Cosmology Telescope Polarimeter (ACTPol), was a polarization-sensitive receiver and saw first light in February 2015. This upgrade included the introduction of dichroic arrays: pixels that could observe at 97 and 148 GHz simultaneously. The next upgrade, called AdvACT, added 27, 39, and 230 GHz bands for a total of five frequency bands [48]. This expanded frequency coverage will enable the improved removal of foreground contamination from synchrotron and dust emission. The new AdvACT receiver also achieved slightly higher angular resolution than earlier iterations—1.4 arcmin at 150 GHz.

2.2.1 Observation strategy

The observation strategy for AdvACT was chosen specifically to probe small angular scale science across large areas of the sky [49]. Because our sky observation area overlaps with other surveys such as BOSS, LSST, and DES, we can perform cross-correlations at different wavelengths, which gives us additional information about large-scale structure and its formation, which can improve our understanding of dark matter and dark energy [49]. The AdvACT observation strategy was optimized to achieve uniform coverage across the sky and to avoid high-foreground areas like the galactic plane. The strategy also achieves good cross-linking (as described in 2.1) by taking constant elevation scans of patches of the sky as they rise and set.
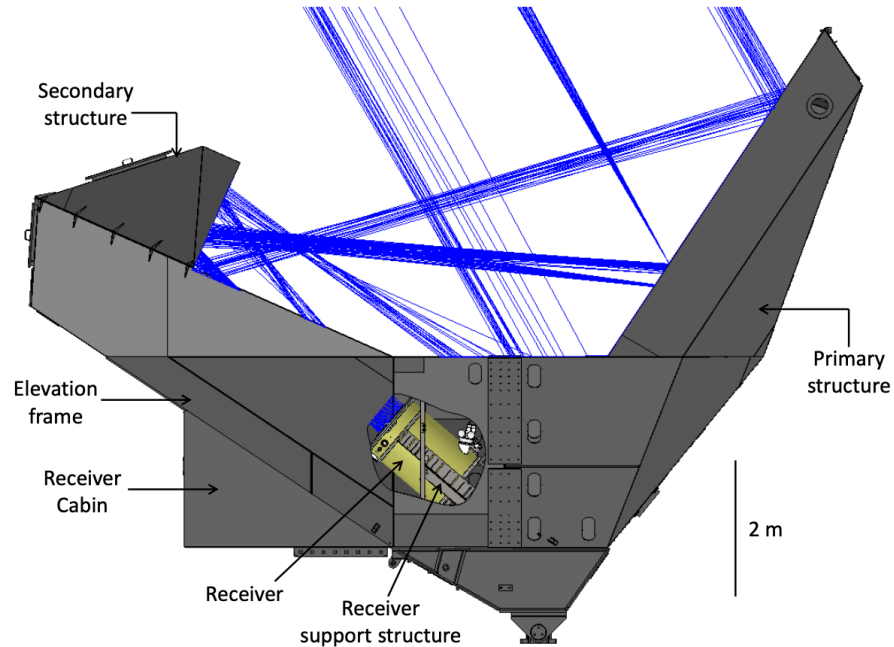
Figure 2.3: ACT and the AdvACT receiver [48]. A ray trace shows incoming light reflecting off two mirrors—the primary and secondary mirrors—and entering the receiver.

2.2.2   Optics

Telescope

ACT has an off-axis Gregorian design, shown in Figure 2.3. The design allows us to map the CMB across the sky with arcminute resolution [48]. As can be seen in Figure 2.4, the telescope mirrors are composed of adjustable aluminum panels— 71 make up the primary mirror, and 11 comprise the secondary mirror. A large ground screen surrounds the entire telescope structure to minimize ground pickup. Light enters the 6 m telescope aperture and reflects off the primary mirror, then the secondary mirror, which reflects the light into the receiver [48].

Receiver

A ray trace of the ACT receiver optics can be seen in Figure 2.5. Light enters the receiver through the cryostat window: a 6.4 mm thick piece of ultra-high molecular
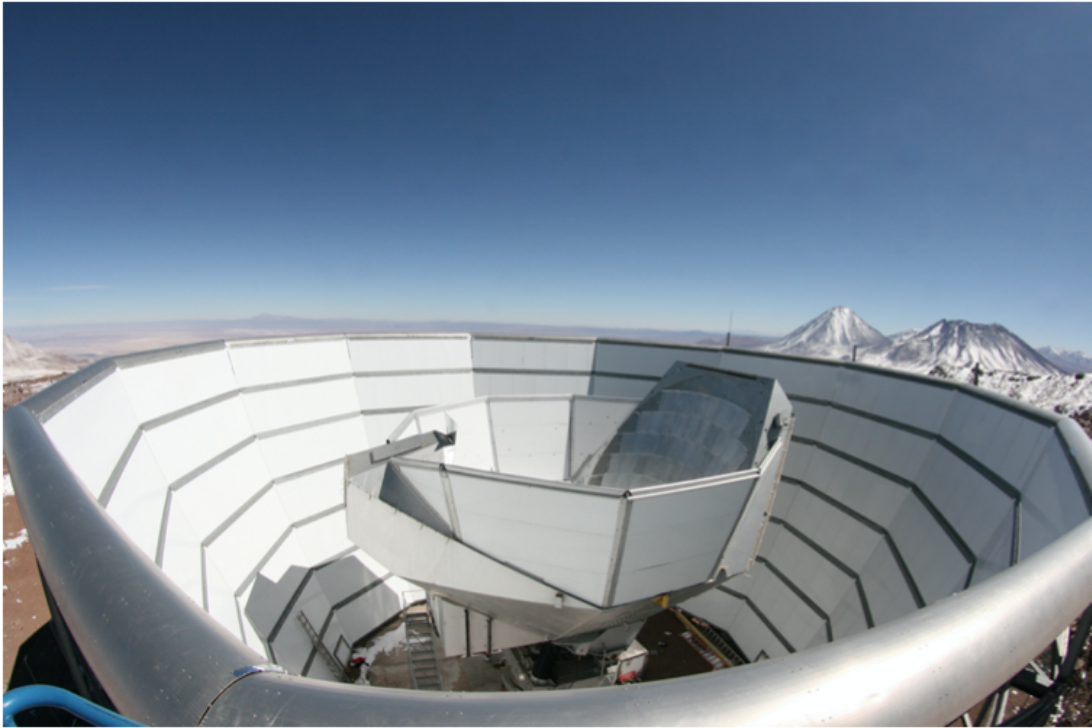
Figure 2.4: A drone shot of ACT [48]. The outer structure is the ground shield, which prevents stray light from the ground and surroundings from interfering with observations. The telescope is the central structure, and the face of the primary mirror is shown on the right side. The face of the mirror is made up of large aluminum panels tiled together.

weight polyethylene (UHMWPE) with an expanded Teflon AR coating. The receiver has 3 optics tubes, and each optics tube contains 3 silicon lenses that focus the light on the detector focal plane, shown in Figure 2.6 [48]. The silicon lenses have a metamaterial AR coating that cuts reflections down to $< 1\%$ (shown in Figure 2.7). The optics tube design also uses a Lyot stop at the 1 K stage to shape the beam. The light then passes through both a low pass and thermal filter. We use a low pass filter to eliminate potential harmonics in the detector bandpasses, and thermal filters are used to block excess IR radiation (heat) [48]. Each of these filters have their own spectral responses that affect our bandpass measurements when we characterize the detector bands.

2.2.3 Cryogenics

The receiver is located inside a cryostat, which keeps our transition-edge sensor (TES) bolometers at operating temperatures (~ 100 mK). A single Cryomech PT410 pulse tube refrigerator cools the outer stages to 40 K and 4 K, as seen in Figure 2.8. Both stages use thermal filter stacks to reduce heat transmission [48].

The remaining components are cooled below 4 K using a ^{3}He–^{4}He dilution refrigerator (DR) from Janis Research Corporation. These components include a Cryomech PT407 pulse tube, which cools the remaining stages to operation temperatures. The 1 K stage consists of a Lyot stop, two silicon lenses, thermal filters, and low-pass filters. The final stage contains the focal plane, which is cooled to 100 mK [48]. The instrument cool-down process takes a total of 14 days to complete, after which the DR can be run continuously without the need for recycling.

2.2.4 Focal plane

AdvACT has 4 total optics tubes, each containing one focal plane array. At any given time, three optics tubes are installed in the receiver for observations. The focal
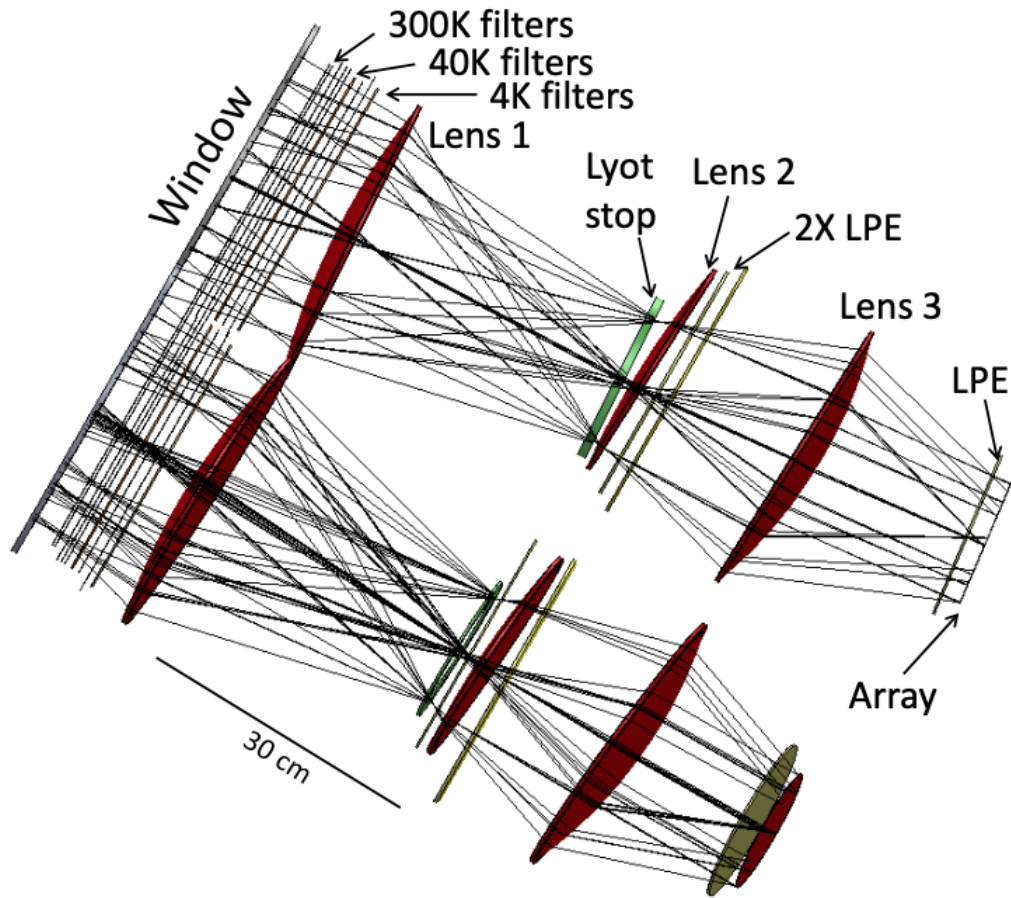
Figure 2.5: Ray trace of the ACTPol optics tubes, which are similar to those on AdvACT [48]. Light enters from the top left and passes through the half-wave plates just outside the cryostat window (not pictured). The light then passes through the window into the cryostat, through several of IR-blocking filters. Lens 1 creates an image plane at the Lyot stop, and the light then passes through Lens 2, low-pass filters, and Lens 3 (the final lens) before being imaged onto the focal plane feedhorn array.
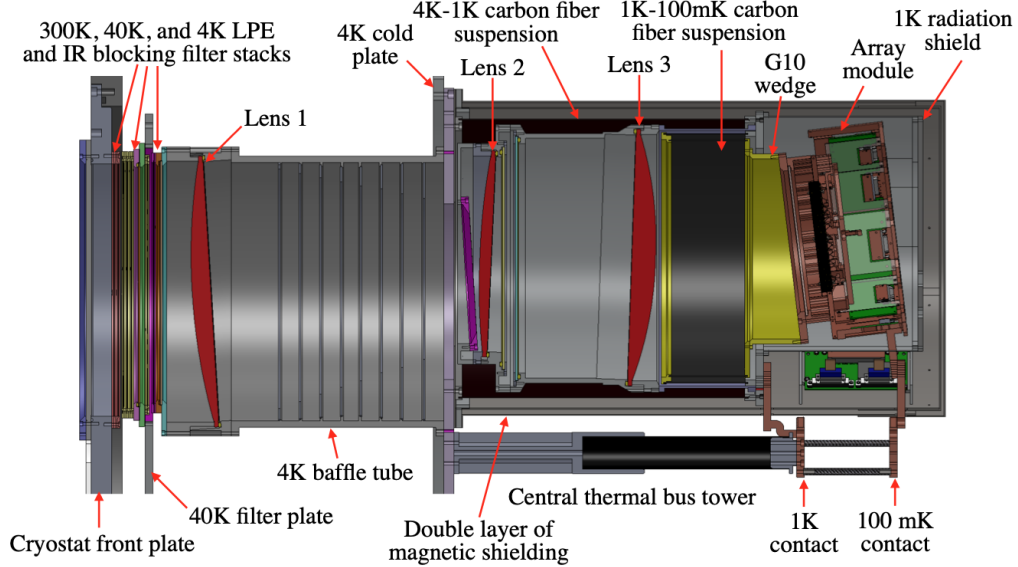
Figure 2.6: A CAD drawing of the AdvACT receiver [48]. The successively colder cryostat stages are marked.

plane arrays are maintained at 100 mK and consist of 6 inch hexagonal detector wafers stacked together with feedhorn and backshort structures. AdvACT is the first ACT experiment to use a single 150 mm detector wafer as opposed to several 3 inch wafers. This focal plane layout, shown in Figure 2.9, gives higher detector packing density and uniformity [51].

AdvACT uses one low-frequency (LF) array to observe at 27 GHz and 39 GHz simultaneously. Two mid-frequency (MF) arrays observe at 90 GHz and 150 GHz, and one high-frequency (HF) array observes at 150 GHz and 220 GHz [48]. These detector frequencies were chosen to be inside the atmospheric windows shown in Figure 2.1, and the broad frequency coverage is crucial for foreground removal in our maps [53].

The AdvACT detectors are shown in Figure 2.10. The light is focused on the detector focal plane, where spline-profiled feedhorns impedance-match the CMB signal to our detector array and define the detector beam. These feedhorns are micro-machined into silicon wafers (except the LF array, which is machined into CE7F, a SiAl alloy) [48]. Earlier stages of the ACT experiment utilized ring-loaded corrugated feedhorns, shown in Figure 2.11, which took up more aperture area and thus led to a
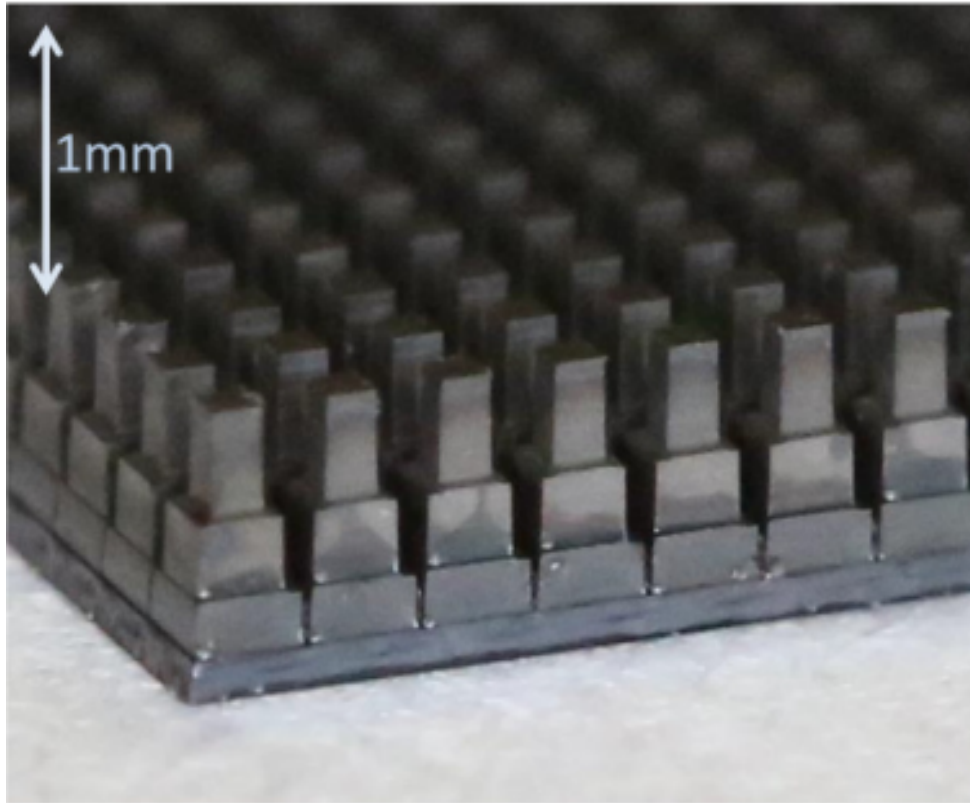
Figure 2.7: The metamaterial AR coating produced in the McMahon lab by Charles Munson, Kevin Coughlin, Joey Golec, and Fletcher Boone [50]. This is a tri-layer "coating" that has been cut into silicon using a custom dicing saw. This etched AR coating cuts surface reflections from $30 - 70\%$ down to less than 1%, giving us much higher signal transmission through the instrument.
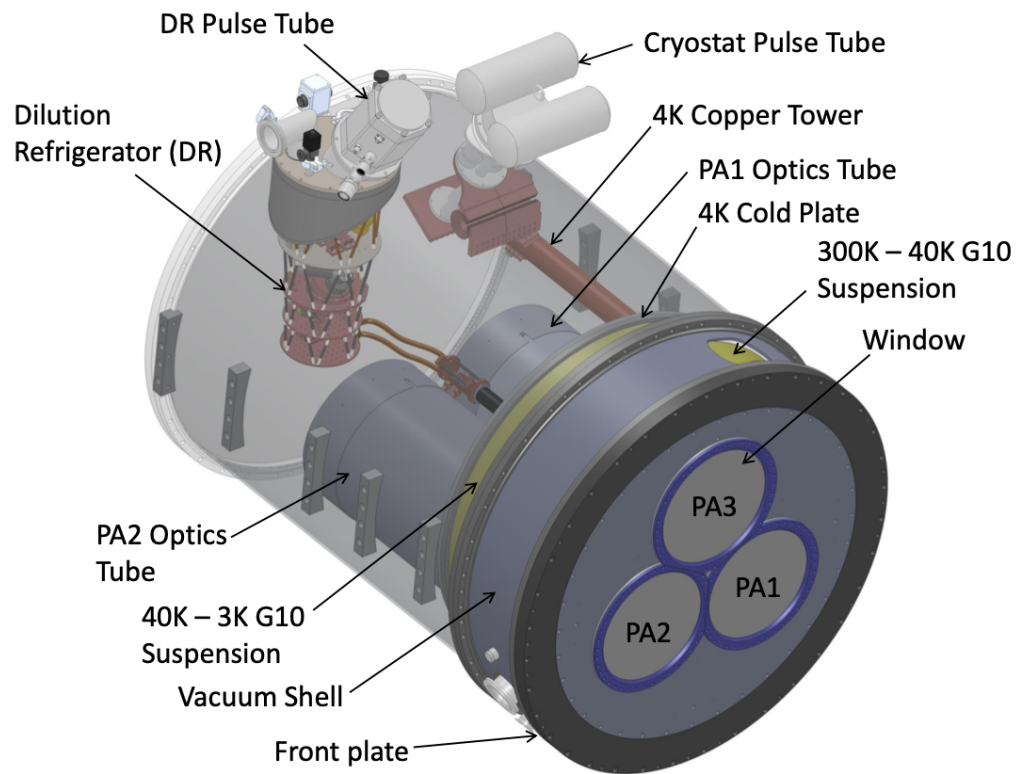
Figure 2.8: The receiver cryostat that houses the 3 AdvACT optics tubes (marked PA1, PA2, and PA3) [48]. The optics tube windows are shown at the front of the structure, and the signal is transmitted back towards the DR.
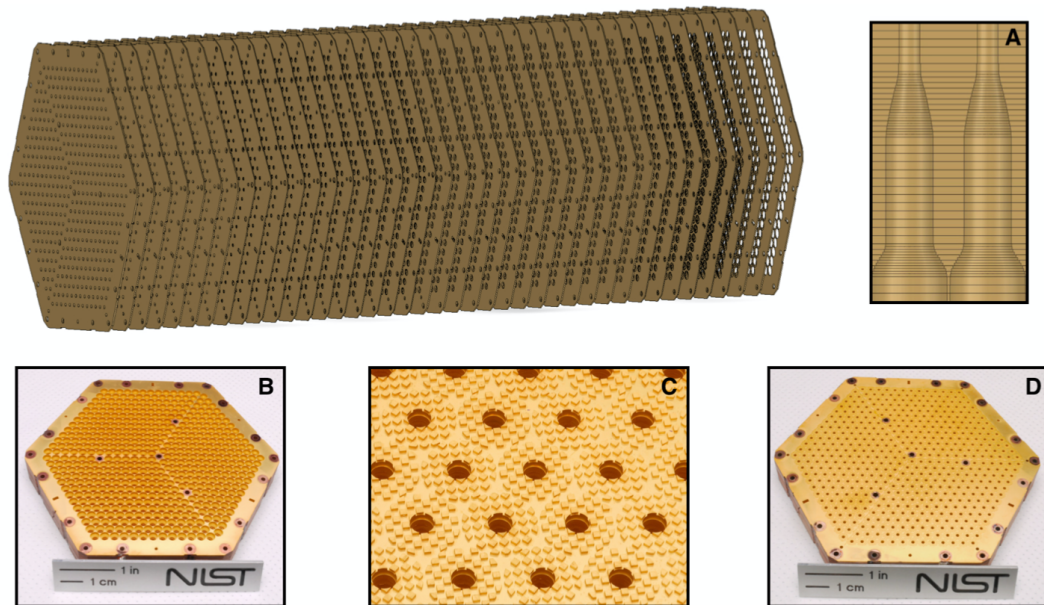
Figure 2.9: The AdvACT feedhorn array [52]. A) The spline profile of the feedhorns that define the detector beam. Circular diameters are machined into thin silicon wafers, and the wafers are stacked (shown to the left of Fig. A)—forming the spline profile. B) The front side of the feedhorn array (where the light enters). C) A close-up view of the back side of the feedhorn array showing the photonic choke structures designed to minimize leakage between the feedhorn and detector array. D) The back side of the feedhorn array.
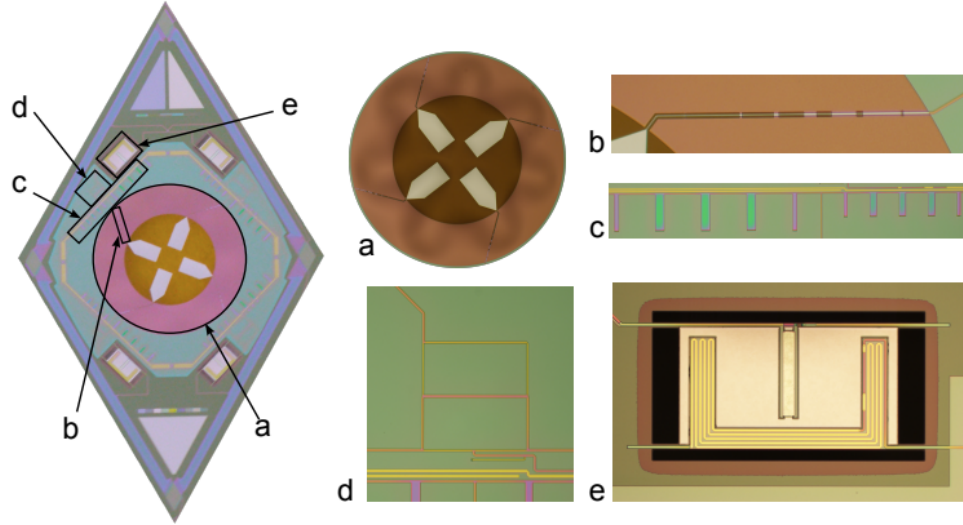
Figure 2.10: A close-up of an AdvACT detector chip [51]. The entire chip is shown on the left, and features are enlarged on the right. a) The OMT that first encounters the light and splits it into orthogonal polarization modes. b) superconducting Nb microstrip that feeds the signal to the bolometers. c) The diplexer; two different stub lengths allow for detection in two frequency bands simultaneously by different TESs. d) A hybrid tee removes higher order modes and couples the signals to the bolometers—the next component on the chip. e) A TES bolometer. There are 4 bolometers per chip—two for each frequency band and polarization.

lower signal transmission efficiency when compared to spline-profiled feedhorns [54]. Any feedhorn acts as a waveguide and will have an associated cutoff frequency, so we optimize these feedhorn cutoff frequencies to prevent interference with our signal in the chosen frequency bands [48].

Each detector pixel has one feedhorn, one orthogonal mode transducer (OMT), and four TES bolometers—one for each of the two polarizations in the two frequency bands measured in each pixel. The OMT, shown in Figure 2.10, separates orthogonal polarization modes in our beam and is impedance-matched to the microstrip on the detector chip [51]. Quarter-wave stubs on the chip define our detector bandpasses. Next, the signal passes through a hybrid tee, which rejects higher-order polarization modes, giving a cleaner polarization signal [48].

The signal then meets the TES bolometer, where it is finally measured. TESs
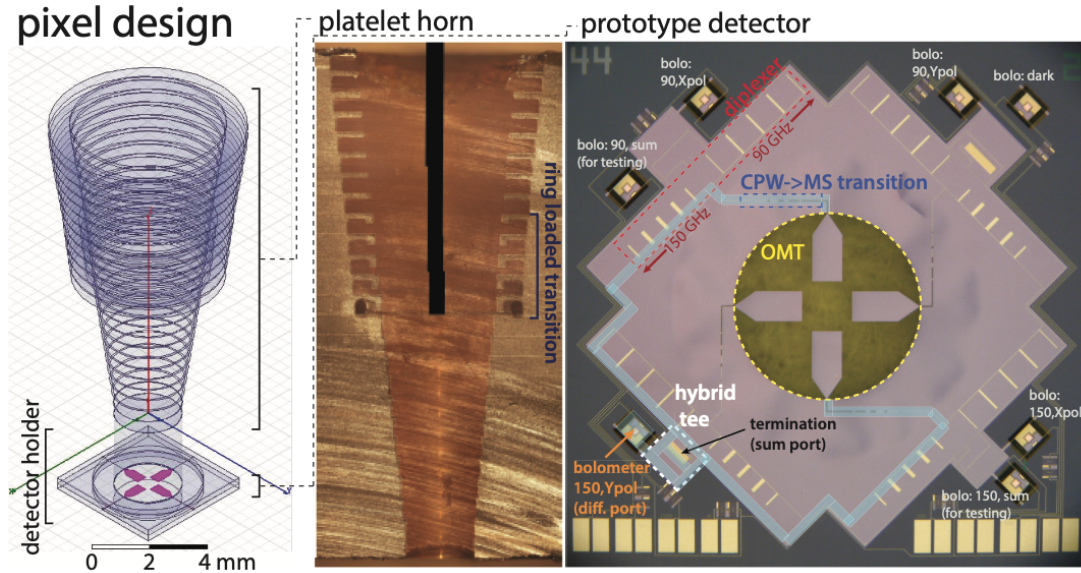
Figure 2.11: View of an ACTPol feedhorn, which has a corrugated profile [55]. Corrugated feedhorns take more space than the current spline-profile feedhorns. By switching to a spline profile, we were able to pack more detectors on a wafer, increasing our sensitivity.

are made of superconducting materials; AdvACT uses a single layer of AlMn alloy. This gives improved uniformity in performance over the Mo-Cu bilayers used in the ACTPol experiment, as a single layer can be deposited more uniformly across each detector array [48, 51]. The TES superconductor is biased at the steep transition state between zero resistance (superconducting) and normal resistance as shown in Figure 2.12. When a superconductor is held at its steep transition edge, the tiniest amount of heat absorbed by the superconductor leads to a dramatic change in its resistance. These TES bolometers are therefore ideal for detecting small fluctuations (< 100 nK) in the CMB photons—a small variation will heat the TES and cause a measurable change in resistance, which can be picked up and amplified by the semiconducting quantum interference devices (SQUIDs) in the readout system [48, 56].
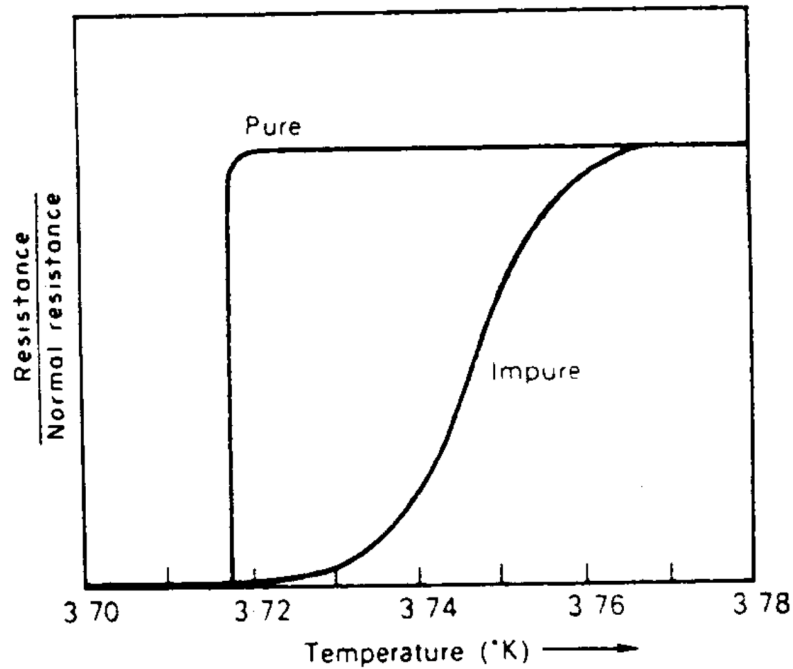
Figure 2.12: The resistance of tin (Sn) at low temperatures [57]. An ideal super-conductor has zero resistance below a characteristic transition temperature (critical temperature) and jumps to a roughly constant measurable resistance at temperatures higher than the critical temperature. This is marked in the plot as "pure"—the re-action of an ideal, pure superconducting material to cold temperatures. In reality, the superconductor transition looks more like the plot marked "impure." We uti-lize this property of superconductors in our TES bolometers by holding them at a temperature right in the middle of the sharp resistance transition (around 3.75 K for the material shown in this figure). A very small heat increment therefore causes a significant change in the material resistance, which can be measured. Our detectors are designed to have a critical temperature around 160 mK.

2.2.5 Readout

Each TES bolometer is wired in series with an inductor, so a change in TES resistance causes a change in the current through the inductor. This results in a change in magnetic field, which is measured by a SQUID—called the Stage 1 SQUID (SQ1). As shown in Figures 2.13 and 2.14, each TES has a SQ1, and 64 SQ1's are inductively coupled to a single read-out line, called a column. Each column is inductively coupled to a Stage 2 SQUID (SQ2), which amplifies the signal [58]. Inductors are chosen in each of these stages to reduce sources of electronic noise within the TES circuit. Each column is then read out using time-division multiplexing (TDM): the column's 64 signals are read out on a single channel successively in time [58]. This method is chosen to reduce the number of connections between the cryostat and the readout system, which is at room temperature, so the cold stage does not become thermally overloaded.

2.3 Simons Observatory

Simons Observatory is a next-generation CMB experiment being built nearby the AdvACT site: on top of Cerro Toco at an altitude of $5,200$ m. SO will take precision temperature and polarization measurements over six frequency bands: 27, 39, 93, 145, 225, and 270 GHz. The introduction of a 270 GHz band gives SO wider frequency coverage than AdvACT has; the additional ultra high-frequency (UHF) band will allow for more precise source detection and foreground removal in CMB maps [59].

SO will utilize over 60,000 TES bolometers (compared to the ∼5,000 on AdvACT) and take measurements covering angular scales between 1 arcminute and tens of degrees. With roughly diffraction limited telescope designs, the angular resolution of a telescope is set by its aperture size. Covering such a wide range of angular scales thus requires deploying two different telescope classes: the LAT, which will be
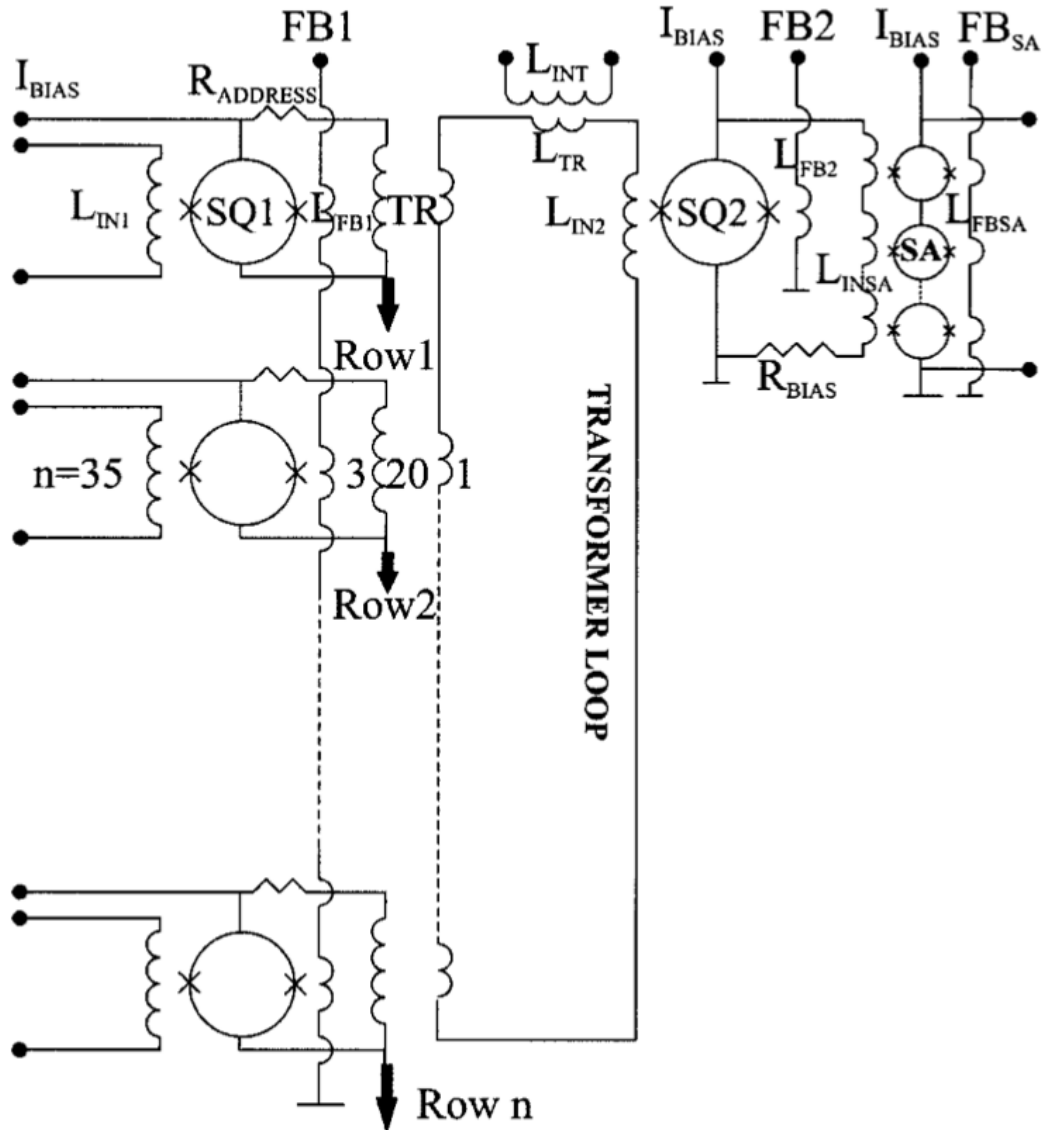
Figure 2.13: A circuit diagram of SQ1s coupled to a single SQ2 at the top, which forms a single column or unit in the readout system. Each SQ1 is inductively coupled to a single detector, and 64 SQ1s are coupled to a single SQ2. Inductive coupling is used throughout the circuitry to reduce noise in the system and minimize direct connections to the cold focal plane [58].
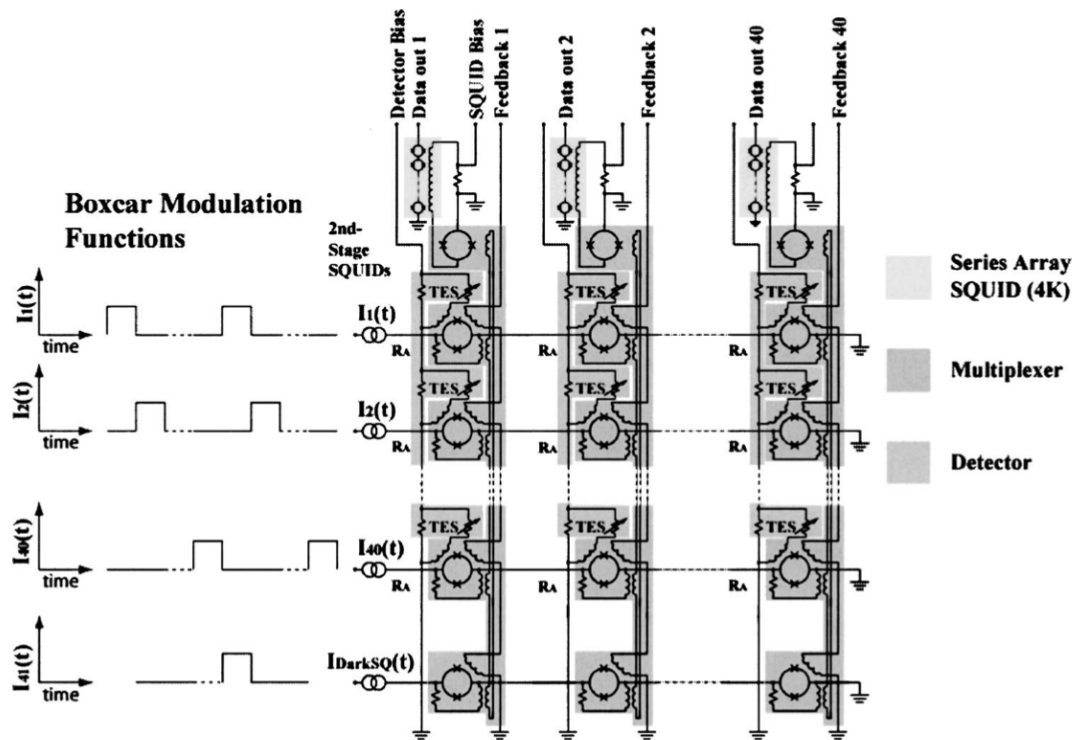
Figure 2.14: The SQUID readout system in the TDM architecture [58]. On each SQ2 (or column) each SQ1 (or row) is read out individually at a different time. This way, 64 detectors can be read out on a single line.

coupled to over 30,000 detectors and focus on small angular scale science, and the Small Aperture Telescope (SAT), which will be coupled to over 30,000 detectors and focus on large angular scales [59].

SO will have three SATs. The SATs will focus on constraining the tensor-to-scalar ratio, r, by measuring or constraining large-scale or low-ℓ ($50 < \ell < 500$) inflationary B-modes across small patches of sky [59].

The LAT will aim to measure small-scale or high-ℓ ($500 < \ell < 3000$) temperature anisotropies, E-modes, the lensing B-mode signal, SZ effects, and extragalactic sources. By measuring these signals, the LAT will help us constrain parameters such as H_0, Σm_ν, and N_{eff}. The LAT's broad sky coverage will overlap with other surveys such as DESI and LSST, as shown in Figure 2.15 [60]; we can therefore perform cross-correlations between these various surveys to help constrain our cosmological parameter estimates [38].

SO will significantly improve the constraints on many cosmological parameters, pushing them toward critical thresholds. Table 2.1 shows the science parameter forecasts for SO [38].

2.3.1   Observation strategy

SO uses different observation strategies optimized to the LAT and SATs' unique science goals. The LAT will target large areas of the sky ($\sim 40\%$) to focus on small angular resolution science. This strategy for the LAT targets the lensing B-mode signal, E-mode signal, and temperature anisotropies, from $500 < \ell < 3000$ [60]. The SATs will target the inflationary B-mode signal, which peaks around $\ell \sim 100$. To reach the deep levels of integration necessary to detect the faint B-mode signal, the SATs will scan much smaller sections of the sky ($\sim 10\%$). Focusing on smaller sections will also allow us to avoid areas with high galactic foreground contamination [60]. The sky coverage of the LAT and SATs is shown in Figure 2.15

Simons Observatory Science Forecasts						
	Parameter	SO Baseline (no syst.)	SO Baseline	SO Goal	Current	Method
Primordial perturbations	r $e^{-2\tau}\mathcal{P}(k=0.2/\text{Mpc})$ $f_{\text{NL}}^{\text{local}}$	0.0024 0.4% 1.8 1	0.003 0.5% 3 2	0.002 0.4% 1 1	0.03 3% 5	BB + ext delens $TT/TE/EE$ $\kappa\kappa \times$ LSST-LSS + 3-pt kSZ + LSST-LSS
Relativistic species	N_{eff}	0.055	0.07	0.05	0.2	$TT/TE/EE + \kappa\kappa$
Neutrino mass	Σm_ν	0.033 0.035 0.036	0.04 0.04 0.05	0.03 0.03 0.04	0.1	$\kappa\kappa$ + DESI-BAO tSZ-N $\times$ LSST-WL tSZ-Y + DESI-BAO
Deviations from Λ	$\sigma_8(z=1-2)$ H_0 (ΛCDM)	1.2% 1.2% 0.3	2% 2% 0.4	1% 1% 0.3	7% 0.5	$\kappa\kappa$ + LSST-LSS tSZ-N $\times$ LSST-WL $TT/TE/EE + \kappa\kappa$
Galaxy evolution	η feedback p_{nt}	2% 6%	3% 8%	2% 5%	$50-100\%$ $50-100\%$	kSZ + tSZ + DESI kSZ + tSZ + DESI
Reionization	Δz	0.4	0.6	0.3	1.4	TT (kSZ)

Table 2.1: SO science forecasts: 1σ forecast uncertainties on cosmological parameters for the baseline and goal noise levels [38]. All SO forecasts assume that SO is combined with Planck data. 'SO Baseline' is the nominal forecast, including instrument systematics. Key targets for the experiment are constraining the tensor-to-scalar ratio r, the effective number of relativistic species N_{eff}, the sum of the neutrino masses Σm_ν, and the Hubble constant H_0. The projection for r is obtained from the BB spectrum; both N_{eff} and H_0 come from TT/TE/EE and the lensing convergence power spectrum $\kappa\kappa$; the neutrino mass sum Σm_ν is constrained using $\kappa\kappa$ along with BAO measurements from the DESI [38].

2.3.2 Large Aperture Telescope

The LAT is a 6 meter crossed Dragone designed to have a large field of view (FOV) [61]. It is coupled to the LATR, which has the capacity to house 13 optics tubes. In the initial deployment, we will use 7 optics tubes, each with 3 150 mm detector arrays. We will have 2 HF optics tubes, 1 LF, and 4 MF. Each optics tube has a 1.3° FOV diameter, yielding a total FOV of 7.8° [59]. The optics tubes each contain 3 lenses (shown in Figure 2.17) to focus the light onto the detector focal plane. The LAT will be used to map around 40% of the sky with arcminute resolution, to a white noise level of 6 μK-arcmin [48].
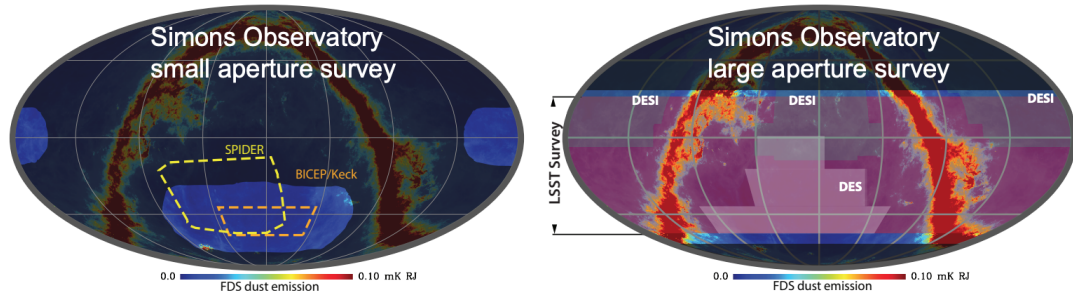
Figure 2.15: Left: The SAT observation patches. Overlap with SPIDER and BICEP/Keck surveys are marked. The galactic plane where foreground emission is the highest is represented by the curved reddish-brown emission on the map, and it is entirely avoided in the SAT scan area. Right: The LAT survey area. The LAT will map about 40% of the sky, and will have significant overlap with DES and DESI, as shown [49].
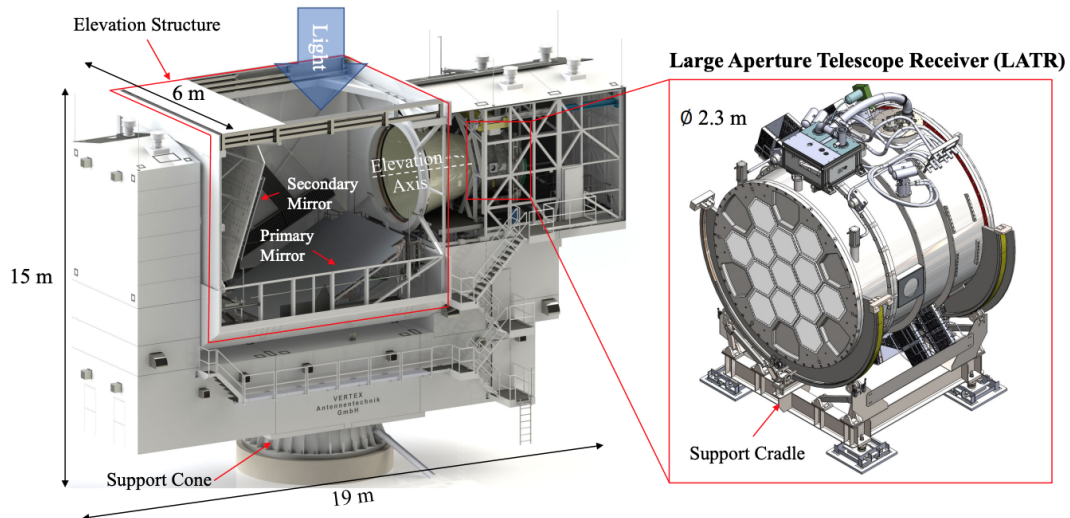
Figure 2.16: The LAT and its cryogenic receiver (LATR). The rendering of the LAT is shown on the left. The support cone and the elevation axis are noted, about which the telescope performs azimuth and elevation rotations during observation. The elevation structure is noted; it looks at the zenith through the opening at the top. Within the elevation structure, two 6 meter mirrors reflect light into the LATR. The right image shows the LATR from its light-receiving side [62]. The LATR is the largest sub-Kelvin steerable cryogenic receiver ever built, With a diameter of 2.3 m [63, 64]. The support cradle co-rotates the LATR with the elevation structure to mitigate optical systematics.
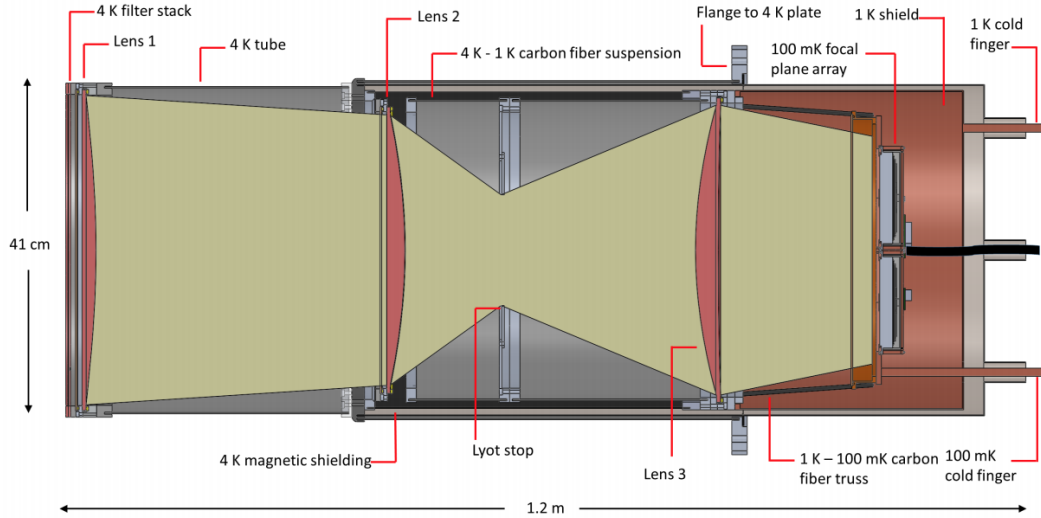
Figure 2.17: A LAT optics tube. Light enters the optics tube window on the left. Three lenses and a Lyot stop are used to focus the telescope beam onto the focal plane array on the right. The thermal filters and cryostat stages are also annotated. Image courtesy of Bob Thornton.

Focal plane and readout

The LAT detectors, shown in Figure 2.18, are TES bolometers that use a similar architecture to the AdvACT detectors. With over 60,000 detectors, SO needs to use two foundries to produce the detectors. Each of the foundries have different expertise in fabricating different detector architectures. SO will thus use two pixel architectures: the MF and HF detectors will be feedhorn and OMT coupled (fabricated by NIST), while the LF will use a lenslet coupled to a sinuous antenna (fabricated by the University of California at Berkeley). The DR cryogenic system is also similar to AdvACT's, but tuned for the larger cryostats used to house the LATR [61].

Instead of TDM, SO will use microwave multiplexing (μMUX) to read out all 60,000+ detectors. Where TDM steps through each detector signal successively on a single line, μMUX reads out all detectors on a single coaxial line using resonant frequencies [59]. Each detector will have a unique resonant frequency, and will be read out at that frequency. This will drastically reduce the number of wire bonds required to read out the detectors, which simplifies the assembly and packaging of
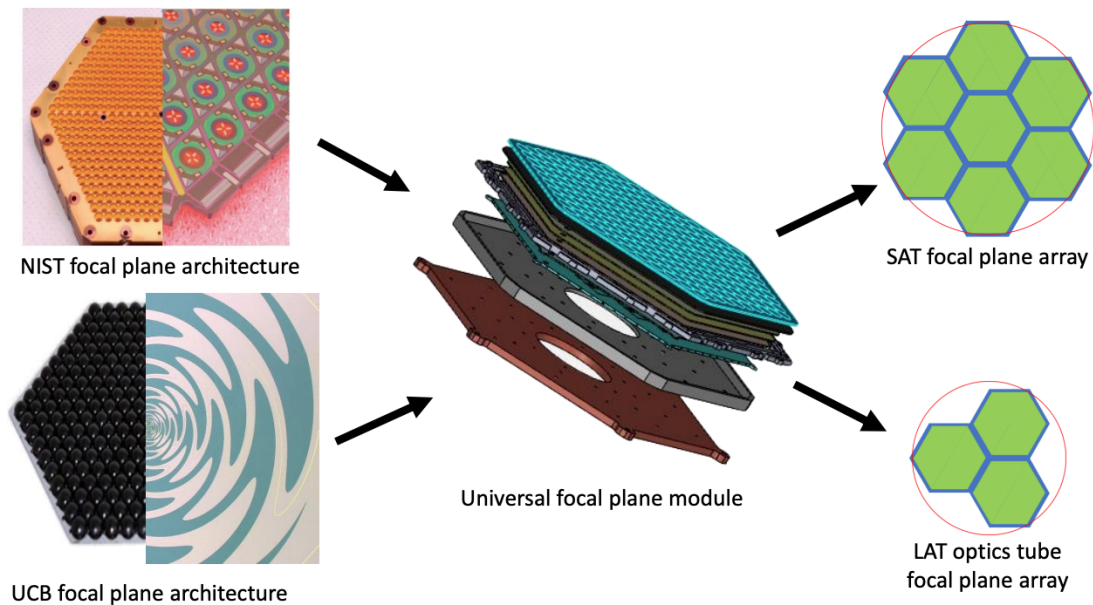
Figure 2.18: The SO detector focal plane arrays [59]. The top right image shows the horn and OMT coupled NIST focal plane with a close-up view of the detector chips. The bottom right image shows a UCB focal plane, which uses lenslets to couple the signal to a sinuous antenna, shown in the close-up half. Unlike the OMT, the sinuous structure has a frequency-dependent polarization angle that must be mitigated in the analysis. The universal focal plane module—a stack of the feedhorn array, detector array, backshort components, readout components and structural elements— is shown in the center. These individual modules are tiled together to form the SAT (top) and LAT (bottom) focal plane arrays, illustrated on the right.
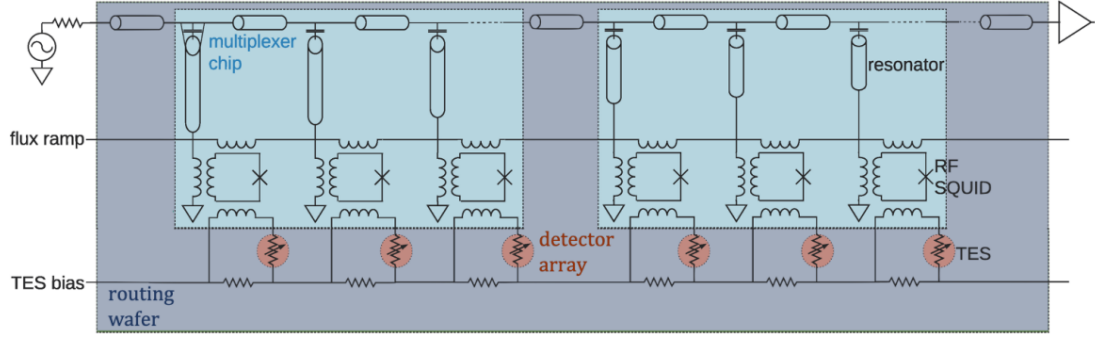
Figure 2.19: Schematic showing the microwave SQUID multiplexing (μMUX) circuit and implementation in the focal-plane module for SO [65]. The routing wafer is marked in grey, multiplexer chips blue, and TES detector array red.

the detector modules, increasing the yield.

2.3.3 Small aperture telescope

In addition to the LAT, SO will also deploy three 42 cm SATs to target large angular scales. Two telescopes will observe at 93 and 145 GHz and one will observe at 225 and 280 GHz. For one year, one of the MF telescopes will be switched out for a 27/39 GHz telescope [59]. Each SAT will have a single optics tube that houses 3 lenses and 7 detector wafers, shown in Figure 2.18. Each optics tube will also use a continuously rotating HWP, described below, to reduce slowly-varying noise fluctuations from the atmosphere in the measurements. The SATs will collectively map about 10% of the sky with 0.5° angular resolution, to a white noise level of 2 μK-arcmin [59]. Each SAT will use the same detector architecture and readout system as the LAT's, described in Section 2.3.2.

Half-wave plates

The SATs will each house a half-wave plate (HWP), shown in Figure 2.20, which will help mitigate systematic effects. The HWPs are made of 3 stacked layers of sapphire (seen in Figure 2.21) and continuously rotate at 2 Hz, which modulates the
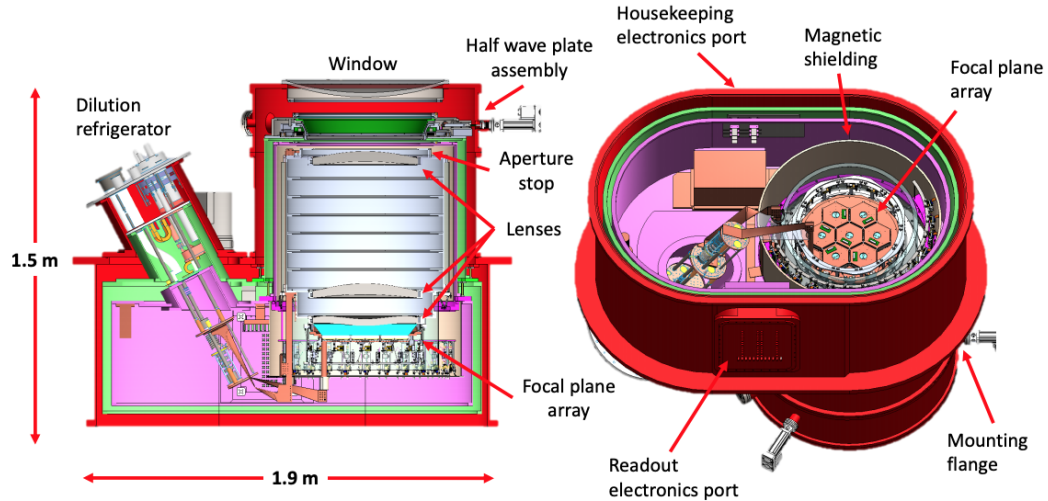
Figure 2.20: The SAT assembly [59]. The half wave plate is installed right below the cryostat window (on the inside of the cryostat). The focal plane array is at the base of the structure, shown from the bottom on the right.

polarization signal at 8 Hz. The largely unpolarized atmosphere is not modulated, so the long time-scale fluctuations from the atmosphere are separated from the polarized sky signal. Mitigating this atmospheric noise is critical especially at large angular scales, where the B-mode polarization signal is expected to peak [36, 66].

Typically CMB experiments get polarization sensitivity from subtracting the signals seen by two orthogonal detectors, but this "pair differencing" can introduce differential systematic effects in the beams, gain, polarization, and bandpasses. Because the HWP modulates the polarization signal, there is no need to pair difference for polarization sensitivity, so there are also no differential systematic effects [36, 66].
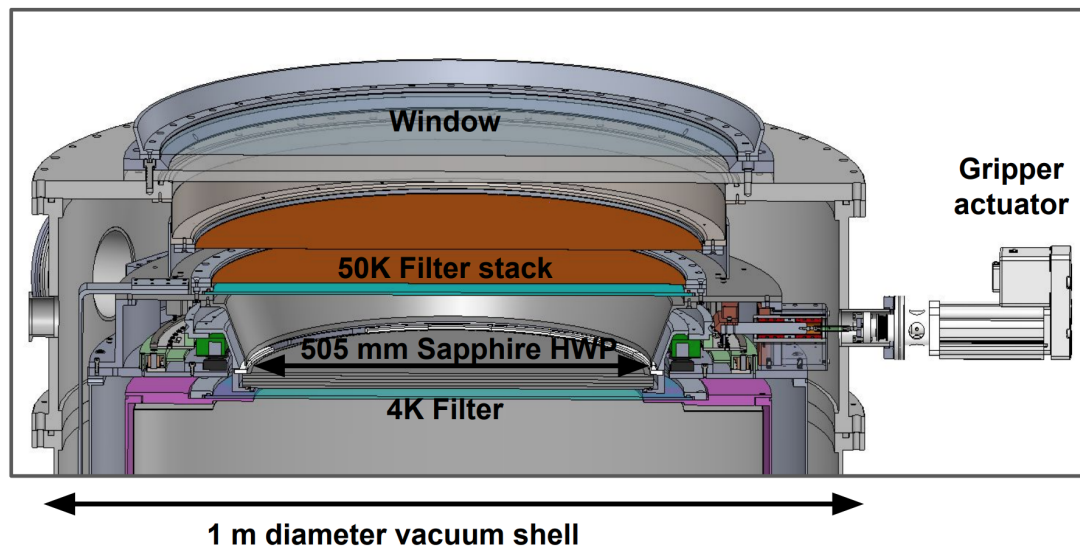
Figure 2.21: A closer view of the SAT cryostat window, thermal filters, and HWP assembly. All components under the window are cooled to 40 K. Image courtesy of Peter Ashton.

CHAPTER III

Bandpass Calibration Using a Fourier Transform Spectrometer

As discussed in Chapter I, the CMB B-mode signal is dominated by polarized foregrounds, namely dust and synchrotron emission. Figure 1.12 shows the different spectral shapes of the foreground components compared to the CMB B-mode signal. The differing frequency dependencies between the foregrounds aids in their removal— if we observe over a broad frequency range, we can characterize the foregrounds and precisely remove them from our maps, leaving a cleaned CMB B-mode signal.

Several sets of observations are required to make these foreground-cleaned maps. We perform pointing, beam, gain, polarization angle, and bandpass calibration measurements. These calibration observations are combined with CMB observations, which are data selected for noise properties and glitches, to create temperature anisotropy and polarization maps. These CMB maps give us our science results: power spectra, constraints for cosmological parameters, and lensing maps.

My work focuses on the detector bandpass calibration that contributes to these maps. AdvACT, SO, and the upcoming CMB-S4 experiment take measurements over several frequency bands to achieve an accurate characterization of foregrounds. To obtain a good fit for the foreground spectra, we must make an absolute measurement of the detector bandpass central frequencies to high precision. In this Chapter, I

describe how absolute bandpass measurements are made.

3.1 Bandpass Calibration

If detector bandpasses are not properly calibrated, the LAT and SATs can't achieve their science goals (further discussed below). It is therefore critical to have an accurate and precise calibration of the LAT and SAT detector wafers. Fabrication variations across a single fabrication wafer are negligible, but the variation between fabrication wafers is on the $\sim 1\%$ level. We thus require measurements of each fabrication wafer to characterize the wafer bandpass. A larger number of measurements on each wafer would decrease the statistical uncertainty of the measurements. However, current measurements are dominated by systematic effects in the measurements, which will be discussed in Chapter IV.

Accurate foreground removal is crucial for upcoming SO observations with the SATs, which will target the weak inflationary B-mode signal and provide the best constraints to date for the tensor-to-scalar ratio r ($\sigma(r) \sim 2 \times 10^{-3}$). If the SATs have uncalibrated bandpasses, we will not be able to properly remove polarized foregrounds, and there will be foreground contributions in our B-mode maps. This will lead to an incorrect measurement of the tensor-to-scalar ratio r. An acceptable level of bias on r for SO is $\Delta r \simeq 10^{-3}$. Reaching this constraint on r requires reducing uncertainty in the detector bandpass central frequencies. We must know the LF band centers to within 6.70%, MF band centers to within 0.90%, and the UHF band centers to within 0.46% of their true values. A more conservative value would be $1/10 \, \sigma(r)$, which would be $\Delta r \simeq 2 \times 10^{-4}$. This would require knowing the LF band centers to within 2.20%, MF band centers to within 0.33%, and the UHF band centers to within 0.20% [67]. With marginalization over all systematic effects, this requirement can be loosened to ± 3 %, but future experiments like CMB-S4 will be even more stringent [67]. These measurement requirements on bandpass calibration are shown

SO Bandpass Calibration Measurement Requirements		
Frequency Band	$\Delta r \simeq 10^{-3}$	$\Delta r \simeq 2 \times 10^{-4}$
LF	6.70%	2.20%
MF	0.90%	0.33%
UHF	0.46%	0.20%

Table 3.1: Calibration requirements for the LF (27/39 GHz), MF (93/145 GHz), and UHF (225/280 GHz) detector bands [67]. To obtain a sufficient level of bias on r (Δr), we must know our detector bandpass central frequencies to these accuracy levels.

in Table 3.1.

The LAT is expected to need a similar calibration level for removing the lensed B-mode signal from the inflationary signal. However, the LAT has a more stringent constraint on its bandpass calibration from source identification. To characterize and analyze contributions from the tSZ effect, we must separate it from both the CMB signal and signals from other point sources. The CMB and tSZ signals have distinct spectral dependencies that can be separated if characterized over several frequency bands, and we must know the detector bandpass central frequencies to exceedingly high accuracy to do so. Analysis of data from the SATs only involves separating foregrounds from the CMB signal; with the LAT analysis, however, we must characterize both the tSZ signal *and* the CMB signal, making calibration requirements much more stringent. Initial estimations place a calibration requirement of the band centers to a level of $\sim 0.1\%$ for the LAT[1]. Not reaching this calibration level will cause an error in the SZ source identification and cause difficulty when removing the lensed B-mode signal from inflationary B-modes.

The primary method for characterizing detector bandpasses is to use a Fourier transform spectrometer (FTS). An FTS is an interferometer that uses a source with a known spectrum to measure the spectral response of a system. We take absolute FTS measurements of our full system to calibrate the spectral response of the detectors

---

[1]Private correspondence with Colin Hill and Mat Madhavacheril.

and optics in the telescopes. The spectral response is dominated by the detector on-chip bandpass filters, but also includes contributions from free-space filters, lenses, and any other optics in the system. While many types of interferometers (Michelson, Fabry-Perot, etc.) can be used for Fourier transform spectroscopy [68], AdvACT uses a PIXIE-style FTS [69], which is an off-axis, symmetric Martin-Puplett design, shown in Figure 3.1, allowing for two inputs and two outputs, like the classic Martin-Puplett design.

This chapter will examine how a simple Fourier transform spectrometer is used to collect data and the mathematics that we use to transform raw data into spectra. I will begin by describing the beams within a typical Martin-Puplett FTS and forming a model for its output interferogram. I will then show how this output is transformed to produce a meaningful spectrum for the input source. The effects that discrete Fourier transforms have on the frequency resolution and range of the final spectrum will also be discussed. Finally, I will describe the unique PIXIE FTS design used by AdvACT and SO for detector bandpass calibration.

3.2 Basic Fourier Transform Spectrometer Design: Martin-Puplett

We can start by understanding the simplified design of a Martin-Puplett Fourier transform spectrometer. A Martin-Puplett interferometer is a variation of the Michelson interferometer. Both use an input beam, a beam splitter, and a set of mirrors to create an interference pattern in the recombined output beam, shown in Figure 3.2a. Analysis of an interferometer's interference pattern measurements can reveal properties of components in the interferometer system or be used to make precise distance measurements [70]. The output of an FTS is an interference pattern between two beams, called an interferogram, which can be Fourier transformed to extract the spec-
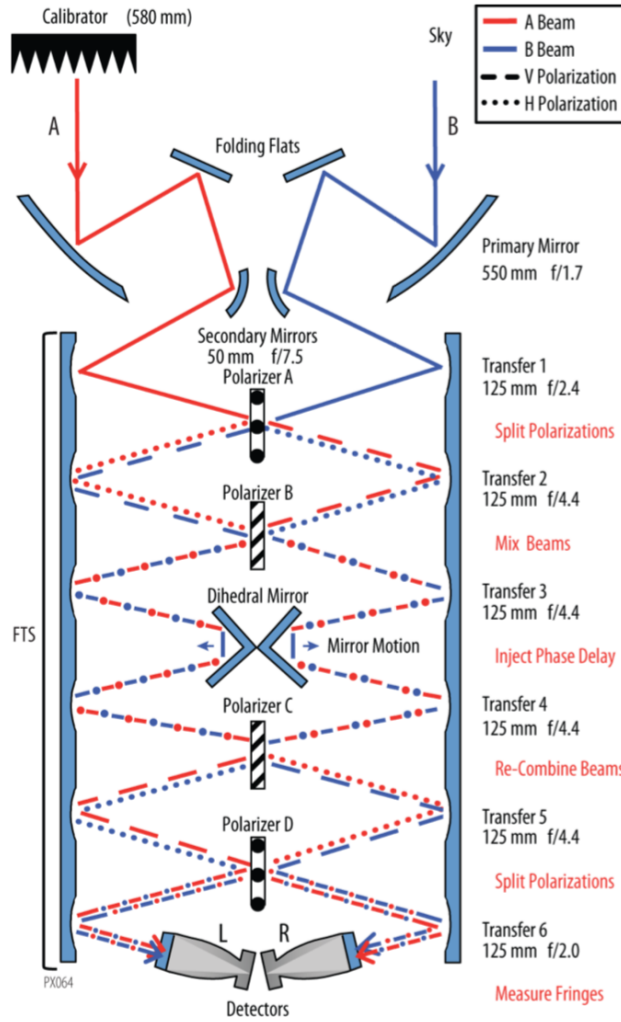
Figure 3.1: A PIXIE-style FTS [69]. Our AdvACT design does not include the transfer mirrors, primary mirrors, or folding flat, as shown in Figure 3.8. AdvACT couples the FTS signal to detectors in the cryogenic telescope receiver via a set of coupling optics.
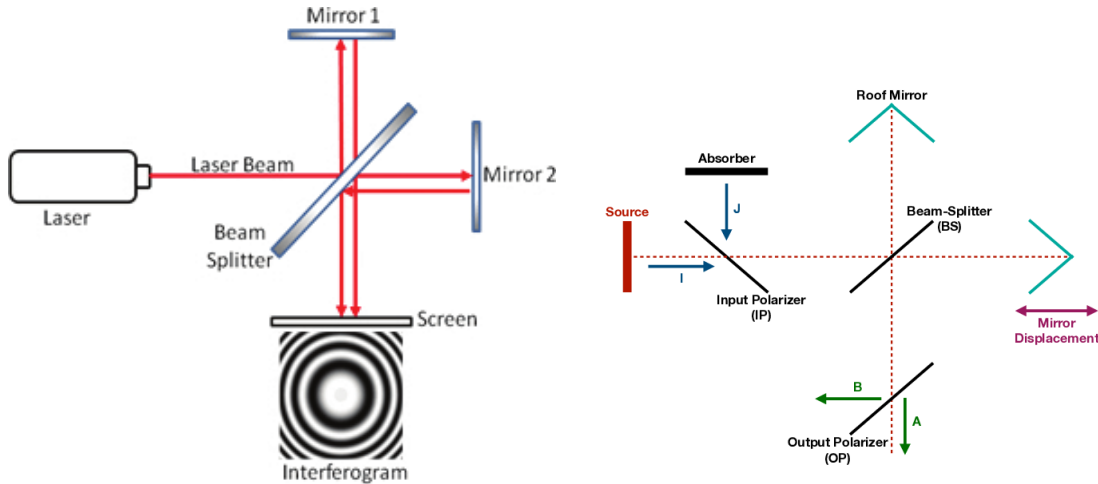
(a) Michelson interferometry [70]. A laser source is split by a beam splitter (typically a grating), which reflects half of the beam to be reflected off Mirror 1 and transmits the other half to be reflected off Mirror 2. The beams recombine when they meet back at the beam splitter, and any path difference between the two beams (created by varying distances to Mirror 1 and Mirror 2) results in interference patterns on the 'Screen', or measured by a detector.

(b) Martin-Puplett Fourier transform spectroscopy [72]. Two input sources (labeled I and J) combine at an input polarizer and are then sent to a beam splitter (typically a polarizing wire-grid). Each half of the split beam will then reflect off a 90° roof mirror, which flips one component of the original polarization. The reflected beams recombine at the beam splitter and are sent to the output polarizer, which gives two outputs (A and B).

Figure 3.2: Comparison of a traditional Michelson interferometer (a) and a basic Martin-Puplett interferometer (b).

tral response of the detector convolved with the source spectrum. The POLARBEAR experiment uses a classic Martin-Puplett FTS to calibrate their bandpasses [71].

3.2.1 Set-up and beam paths

The Martin-Puplett design modifies the Michelson configuration by using a polarizing wire grid as the beam splitter and two "roof top mirrors"—mirrors comprised of two faces that join at a 90° angle—as shown in Figure 3.2b. The use of wire grids yields highly efficient, polarized beam splitting with virtually no frequency dependence in transmission or reflection [72].

Unlike the Michelson design, Martin-Puplett interferometers have a polarized output and a total of four ports—two input and two output—shown in Figure 3.2b.

Orthogonal polarization modes of two sources are combined at an input polarizer; pairing a thermal source with an absorber at the input polarizer (as in the Figure) reduces broad-spectrum atmospheric noise. A two-port input is therefore useful for measurements that make use of a broad-spectrum or blackbody source. The two input ports are not necessarily advantageous when using a single-frequency source—a single-source input setup is shown in Figure 3.3. The two output signals of the Martin-Puplett interferometer are complementary, which allows for simple signal subtraction and continuous modulation techniques [72].

To illustrate the basic concept of Fourier transform spectroscopy, we can trace a beam's path through a Martin-Puplett interferometer and consider what a detector at one of the output ports would measure. In the following discussion, I'll refer to the beam paths labeled in Figure 3.3 and closely follow the derivation summarized in Lambert and Richards (1978) [68].

The source, shown at the bottom of Figure 3.3 in red, gets polarized at the input by a polarizing wire grid transmitting in the $-\frac{1}{\sqrt{2}}\hat{x} + \frac{1}{\sqrt{2}}\hat{z}$ direction, where $\hat{z}$ points out of the page. The transmitted beam t_0 thus has the form

$$\vec{E}_{t0} = E_0 \left(-\frac{1}{\sqrt{2}}, 0, \frac{1}{\sqrt{2}} \right) \exp\left[i \left(k\hat{y} \cdot \vec{r} - \omega t \right) \right], \tag{3.1}$$

where $k\hat{y} = \vec{k}$ is the beam's wavevector, which has magnitude $|\vec{k}| = k = \dfrac{2\pi}{\lambda}$, and $\omega = ck$ is its angular frequency.

The next polarizer that t_0 passes through is transmitting in the $\hat{z}$-direction and oriented in the xy-plane such that its surface normal points in the direction $\frac{1}{\sqrt{2}}\hat{x} + \frac{1}{\sqrt{2}}\hat{y}$. For an ideal polarizer, 50% of the beam is transmitted in the $\hat{y}$-direction and the other 50% is reflected in the negative $\hat{x}$-direction. The transmitted and reflected beams are
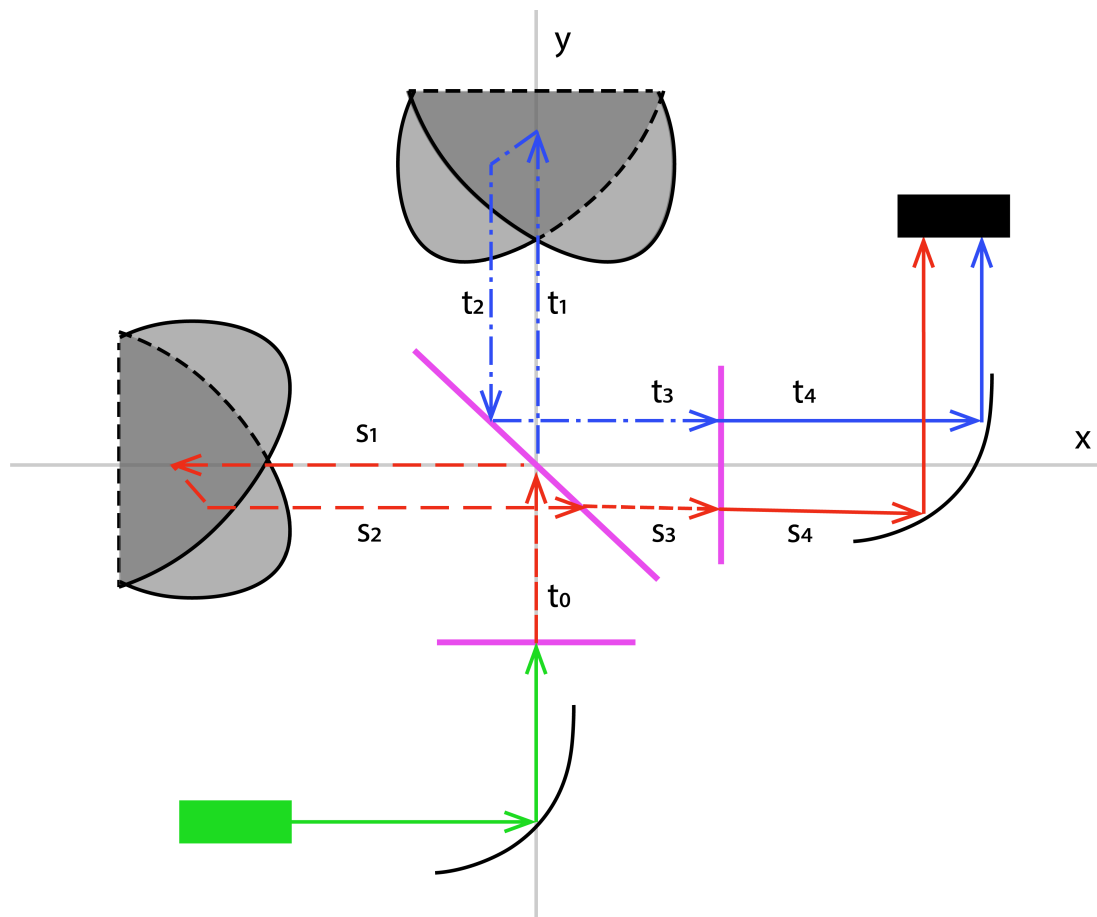
Figure 3.3: Martin-Puplett FTS schematic. The roof mirrors are shown in gray, and pink lines represent polarizers. The single input beam (green) is collimated and gets polarized at the input polarizer. It is then split by a polarizing beam splitter (positioned at a 45° angle in the xy-plane). 90° roof mirrors at the left and top of the figure are oriented such that the incoming beams have a 45° incidence on each roof mirror surface. After passing through a third polarizer, beams t_4 and s_4 are directed into a detector (the black box).

labeled t_1 and s_1, respectively. Their electric fields are

$$\vec{E}_{t1} = E_0 \left(0, 0, \frac{1}{\sqrt{2}}\right) \exp\left[i\left(k\hat{y} \cdot \vec{r} - \omega t\right)\right] \tag{3.2}$$

$$\vec{E}_{s1} = E_0 \left(0, -\frac{1}{\sqrt{2}}, 0\right) \exp\left[i\left(-k\hat{x} \cdot \vec{r} - \omega t\right)\right]. \tag{3.3}$$

where in Equation 3.3, our new wavevector is $\vec{k} = -k\hat{x}$.

Beam t_1 then gets reflected off a roof top mirror whose orthogonal faces meet along a line ("roof line") described by the vector $\vec{u}_{R1} = \frac{1}{\sqrt{2}}\hat{x} + \frac{1}{\sqrt{2}}\hat{z}$, and the reflected beam is labeled t_2. The effect of the roof top mirror on the incident beam can be seen in Figure 3.4. Since an input ray undergoes two reflections when interacting with the roof top mirror, the output ray's polarization is the same as the input's polarization, but with one component flipped. The polarization component that is parallel to the roof line remains unchanged, while the component perpendicular to the roof line flips direction. When an input ray with wavevector $\vec{k}_i$ and polarization $\vec{p}_i$ is reflected by a roof top mirror with a roof line aligned with unit vector $\vec{u}_R$, the output ray has wavevector and polarization

$$\vec{k}_o = -\vec{k}_i + 2(\vec{k}_i \cdot \vec{u}_R)\vec{u}_R \tag{3.4}$$

$$\vec{p}_o = -\vec{p}_i + 2(\vec{p}_i \cdot \vec{u}_R)\vec{u}_R. \tag{3.5}$$

This means that, in the case of Figure 3.3, the component of the electric field $\vec{E}_{t1}$ that remains unchanged by the roof top mirror upon reflection is in the direction of $\vec{u}_{R1}$, and the reflected beam t_2 can be described by

$$\vec{E}_{t2} = E_0 \left(\frac{1}{\sqrt{2}}, 0, 0\right) \exp\left[i\left(-k\hat{y} \cdot \vec{r} - 2ky_{R1} - \omega t\right)\right], \tag{3.6}$$

where the exponential term $-2ky_{R1}$ is included to account for the path distance y_{R1}
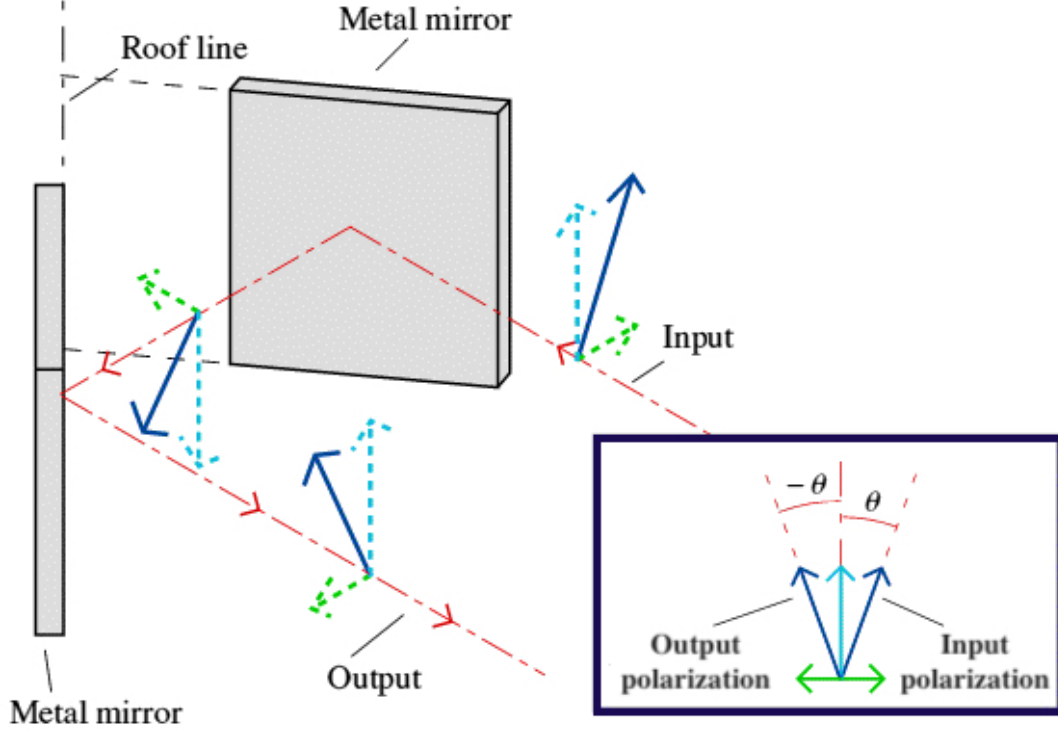
Figure 3.4: Roof mirror diagram. The input polarization component that is perpendicular to the roof line is flipped. This is the result of two reflections. Image by Andrey Baryshev, Netherlands Institute for Space Research.

traveled to the mirror and back. Similarly, the beam s_1 reflecting off the second roof top mirror, described by the roof line vector $\vec{u}_{R2} = -\frac{1}{\sqrt{2}}\hat{y} + \frac{1}{\sqrt{2}}\hat{z}$, produces the reflected beam s_2 with field

$$\vec{E}_{s2} = E_0\left(0, 0, \frac{1}{\sqrt{2}}\right)\exp\left[i\left(k\hat{x}\cdot\vec{r} - 2kx_{R2} - \omega t\right)\right],\tag{3.7}$$

where $2kx_{R2}$ accounts for the beam's path to the second roof top mirror and back.

Beams t_2 and s_2 are both directed towards the central beam splitter. Only the reflected component of t_2 and transmitted component of s_2 are directed towards the output. We will call these beams t_3 and s_3, respectively, and their electric fields are given by

$$\vec{E}_{t3} = E_0\left(0, \frac{1}{\sqrt{2}}, 0\right)\exp\left[i\left(k\hat{x}\cdot\vec{r} - 2ky_{R1} - \omega t\right)\right]\tag{3.8}$$

63

$$\vec{E}_{s3} = E_0 \left(0, 0, \frac{1}{\sqrt{2}} \right) \exp \left[i \left(k\hat{x} \cdot \vec{r} - 2kx_{R2} - \omega t \right) \right]. \tag{3.9}$$

We can see that both beams now have the same wavevector $\vec{k} = k\hat{x} \cdot \vec{r}$, but differ in polarization and phase (assuming $y_{R1} \neq x_{R2}$).

Finally, t_3 and s_3 encounter an output polarizer. For an experimental setup, it is advantageous to modulate the output signal by rotating the output polarizer with a known angular frequency ω_o because it greatly reduces slow fluctuations in the signals ($1/f$ noise). The transmitting axis of the output polarizer thus points in the direction $\sin\omega_o t \, \hat{y} + \cos\omega_o t \, \hat{z}$, and only the transmitted beams are directed towards the output. The transmitted output beams, t_4 and s_4, therefore have fields described by

$$\vec{E}_{t4} = E_0 \left(0, \sin\omega_o t, \cos\omega_o t \right) \frac{\sin\omega_o t}{\sqrt{2}} \exp \left[i \left(k\hat{x} \cdot \vec{r} - 2ky_{R1} - \omega t \right) \right] \tag{3.10}$$

$$\vec{E}_{s4} = E_0 \left(0, \sin\omega_o t, \cos\omega_o t \right) \frac{\cos\omega_o t}{\sqrt{2}} \exp \left[i \left(k\hat{x} \cdot \vec{r} - 2kx_{R2} - \omega t \right) \right], \tag{3.11}$$

making the total output electric field ($\vec{E}_{out} = \vec{E}_{t4} + \vec{E}_{s4}$) equivalent to the real part of

$$\vec{E}_{out} = E_0 \left(0, \sin\omega_o t, \cos\omega_o t \right) \left[\frac{\cos\omega_o t}{\sqrt{2}} e^{-2ikx_{R2}} + \frac{\sin\omega_o t}{\sqrt{2}} e^{-2iky_{R1}} \right] e^{i(kx - \omega t)}. \tag{3.12}$$

3.2.2 Analysis of output beams

Since the polarized beam t_0 has amplitude E_0, the initial unpolarized input beam power is $2E_0^2$, and the fractional power that reaches the detectors at the output is

$$\frac{P_{out}}{P_{in}} = \frac{\left| \vec{E}_{out} \right|^2}{2E_0^2} = \frac{1}{4} \left[1 + \sin\left(2\omega_o t \right) \cos 2k \left(x_{R2} - y_{R1} \right) \right]. \tag{3.13}$$
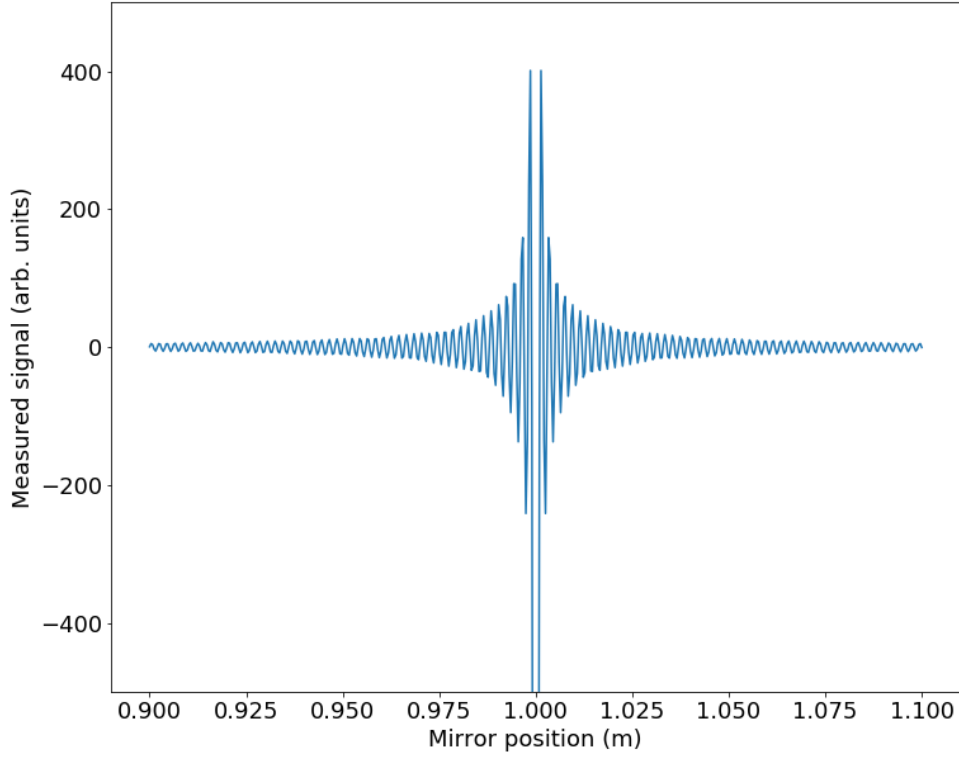
Figure 3.5: Interferogram obtained using Eq. 3.16 at each step of the roof mirror (512 steps). Note that the interferogram is symmetric and peaks at the center (a minimum, in this case).

Demodulating this output at frequency $2\omega_o$ using a lock-in amplifier would then give us the output signal

$$F_{MP}(x_{R2} - y_{R1}) = \frac{1}{4}\cos 2k(x_{R2} - y_{R1}). \tag{3.14}$$

If we only move the top mirror (at position y_{R1}) to create a path difference between the split beams, Eq. 3.14 becomes a function of y_{R1} only. Moving this mirror in small increments along the y-axis and taking a measurement of F_{out} at each y_{R1} position gives us an interferogram—an example of which is shown in Figure 3.5.

Eq. 3.14 only describes the output when using a single-frequency input source.

This can be generalized to describe the output for a source with any spectrum. For a thermal source with a blackbody spectrum, the spectral radiance is

$$B(k) = \frac{hck^3}{4\pi^3} \frac{1}{\exp\left[hck/2\pi k_B T\right] - 1},$$

(3.15)

where $k = 2\pi\nu/c$ is the wavenumber of the thermal radiation, T is the absolute temperature of the source, h is the Planck constant, and k_B the Boltzmann constant. Wien's law tells us that the source spectrum peaks at $k_{max} = T \cdot (2\pi \cdot 196 \text{ m}^{-1}\text{K}^{-1})$, and we can define $B_{max} \equiv B(k_{max})$.

The normalized intensity of our input source at wavenumber $(k + dk)$ is $\frac{B(k)}{B_{max}} dk$. We would therefore expect the Martin-Puplett output signal to have the form

$$F_{out}(\xi) = \int_{-\infty}^{\infty} \frac{B(k)}{B_{max}} \cdot \frac{1}{4} \cos\left[2k\xi\right] dk$$

(3.16)

where $\xi = (x_{R2} - y_{R1})$ is the beam path difference. Note that we are summing over all wavenumbers, and the spectral radiance weighting is normalized by dividing by B_{max}. The simulated output is shown in Figure 3.5.

We can rewrite Eq. 3.16 in exponential form as

$$F_{out}(\xi) = \Re\left\{ \frac{1}{4} \int_{0}^{\infty} \frac{B(k)}{B_{max}} \cdot \exp\left[i\,2k\xi\right] dk \right\}.$$

(3.17)

Here we can see that our measured interferogram function $F_{out}(\xi)$ is simply the inverse Fourier transform of our input signal $B(k)$. By the Fourier integral theorem, we can therefore extract the original input signal from our interferogram by taking a Fourier transform:

$$\frac{B(k)}{B_{max}} = \Re\left\{ 4 \int_{0}^{\infty} F_{out}(\xi) \cdot \exp\left[-i\,2k\xi\right] d\xi \right\}.$$

(3.18)

Note that this signal extraction method will work for any source with spectrum $S(k)$:

$$S(k) \propto \mathcal{F}\left\{F_{out}(\xi)\right\}, \tag{3.19}$$

where $\mathcal{F}$ denotes the Fourier transform operator.

3.2.3 Frequency resolution and range

Because data is taken at each step ($\Delta\xi \equiv -\Delta y_{R1}$) of the FTS mirror, we actually only acquire N discrete samples of the output interferogram $F_{out}(\xi)$ described by Eq. 3.16. We therefore must use a discrete Fourier transform (DFT) to extract an input signal $S(k)$:

$$S(m\Delta k) = \sum_{n=0}^{N-1} F_{out}(n\Delta\xi) \cdot \exp\left[-i\,mn/N\right]. \tag{3.20}$$

In the above equation, $S(m\Delta k)$ is a set of points sampling the true signal spectrum $S(k)$ every Δk, where m indexes each point. The DFT will return N complex output points; however, its output is not a single spectrum, but a spectrum and its mirror image. We therefore only get $N/2$ output points from N input points.

The spatial frequency resolution Δk of the resultant spectrum is related to the FTS step size $\Delta\xi$ by

$$\Delta k = \frac{2\pi}{N\Delta\xi}, \tag{3.21}$$

corresponding to a temporal frequency resolution

$$\Delta\nu = \frac{c}{N\Delta\xi}. \tag{3.22}$$

Periodic, modulating patterns in an interferogram—like those shown in Figure 3.6—are indicative of neighboring spectral lines or features in the resulting spectrum (after Fourier transformation). Two spectral lines separated by a distance d in frequency

WAVENUMBERS CM-1

1/d

X ⟹
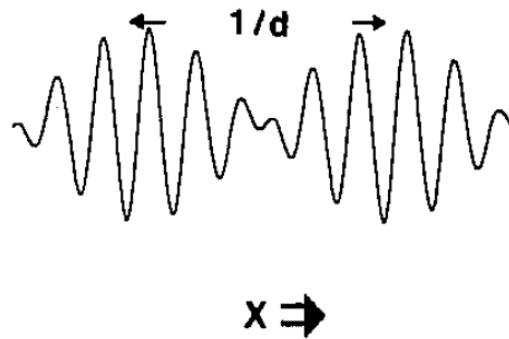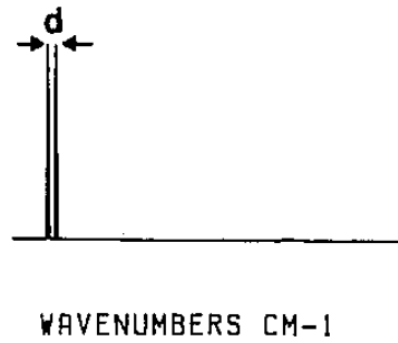
Figure 3.6: Two spectral lines separated by distance d appear as patterns spaced $1/d$ in the interferogram [73].

space can be resolved from an interferogram that shows periodic patterns every $1/d$ in the FTS mirror path (ξ space), as illustrated in Figure 3.6. Therefore, we must step the FTS mirror over a total path length of at least $1/d$ in order to resolve spectral features spaced d apart. This is known as the Rayleigh criterion, and it is used to optimize FTS design parameters.

One may also control the frequency range of the DFT output spectrum simply by changing the FTS step size $\Delta\xi$:

$$\nu_{max} = \frac{N}{2} \cdot \Delta\nu = \frac{c}{2\Delta\xi}. \tag{3.23}$$

The resolution and frequency range of the desired spectra can thus be chosen by changing the FTS scan parameters N (the number of steps) and $\Delta\xi$ (the step size).

3.2.4   Summary

The above analysis techniques form the basis of Fourier transform spectroscopy. Martin-Puplett interferometers are advantageous for use in Fourier spectroscopy for several reasons. Notably, the circular apertures used in the interferometer design have a much greater area than the linear slits used in traditional interferometry, yielding a much higher throughput of radiation. This is known as the Jacquinot advantage.

Additionally, the wire grid polarizers used in the Martin-Puplett design provide nearly perfect beam splitting for frequencies below the cut-off frequency of the grids. This eliminates frequency-dependent systematics caused by the beam splitters, which usually complicate traditional Michelson interferometry. The Martin-Puplett's polarizing beam splitters also allow the instrument to have four ports—two input and two output. The two output ports provide complimentary signals that can be added, subtracted, or otherwise manipulated to suppress spurious noise in the source and output signal.

The basic Michelson interferometer (shown in Figure 3.2a) has output

$$F_{MI}(\xi) = \frac{1}{4}[1 + \cos(2k\xi)], \tag{3.24}$$

differing from the Martin-Puplett output (Eq. 3.14) by an additive constant signal. When the Michelson interferometer output is modulated with a chopper wheel, this extra constant term is known to make fluctuations in the source intensity or detector sensitivity appear as spurious Fourier modes in the measured interferogram. This can cause errors in the final measured spectrum [68]. The lack of extra constant signal in the classic Martin-Puplett's output gives it another advantage over traditional

Michelson spectroscopy.

3.3 PIXIE Design for Calibration Measurements

A "PIXIE-style Fourier transform spectrometer" is designed after the FTS system used by the Primordial Inflation Explorer (PIXIE) team[69], shown in Figure 3.1. FTS measurements for CMB experiments like AdvACT and SO are used to characterize detector bandpasses and precisely determine weighted band centers for each detector array. This process is different from PIXIE's original application, which made comparative measurements of CMB spectra using the FTS as a nulling polarimeter [69]. Nulling the two outputs allows for tight systematic control, as many systematics in the FTS system get cancelled by signal subtraction. Unlike relative measurements, absolute measurements like those required by CMB experiments such as AdvACT and SO are more challenging to perform as they must contend with the systematics of the FTS itself. The following discussion will describe the PIXIE-style FTS set-up as it is used in AdvACT and SO detector calibration. The AdvACT FTS is shown in Figure 3.7.

3.3.1 Set-up and beam paths

As depicted in the simplified diagram in Figure 3.8, we place a thermal IR source at one of the inputs of the FTS (t_0), with the other input blocked (i.e., a blackbody at room temperature). The source radiation enters the FTS, is modulated by a chopper wheel, and is split by a polarizing wire-grid beam splitter. Several reflections and beam splits occur on the path through the FTS, which are traced in Figure 3.8. In the middle of the instrument, a dihedral mirror is stepped along one axis to create a path difference between the split beams before they recombine.

The following discussion of the PIXIE FTS's optical signal path follows Appendix A of Kogut and Fixsen et. al [69]. A plane wave incident on the first wire
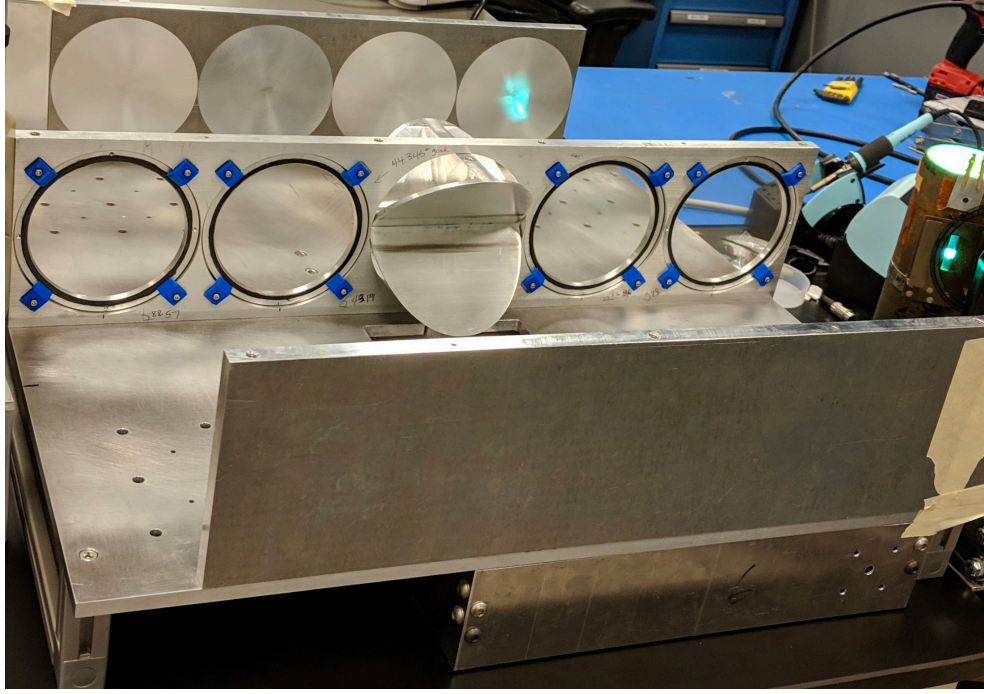
Figure 3.7: The AdvACT FTS with its top plate removed. The first mirror is illuminated by a mercury arc lamp. The dihedral mirror in the center is a double roof mirror.

grid polarizer from the right (the red ray in Figure 3.8) has the form

$$\vec{E}_{\text{source}} = E_x \exp\left[i(kz - \omega t)\right] \hat{x} + E_y \exp\left[i(kz - \omega t)\right] \hat{y} \qquad (3.25)$$

where $\hat{x}$ is in the plane of the diagram, $\hat{y}$ is normal to the page, and $\hat{z}$ is in the direction of propagation. For simplification we will express this as

$$\vec{E}_0 = A\hat{x} + B\hat{y} \qquad (3.26)$$

where $A = E_x$ and $B = E_y$, and we have dropped the term $\exp\left[i(kz - \omega t)\right]$ as it is common to all terms. The first polarizer's wires are oriented along the y-axis, in the plane of the center septum, such that the y-component of the electric field is reflected
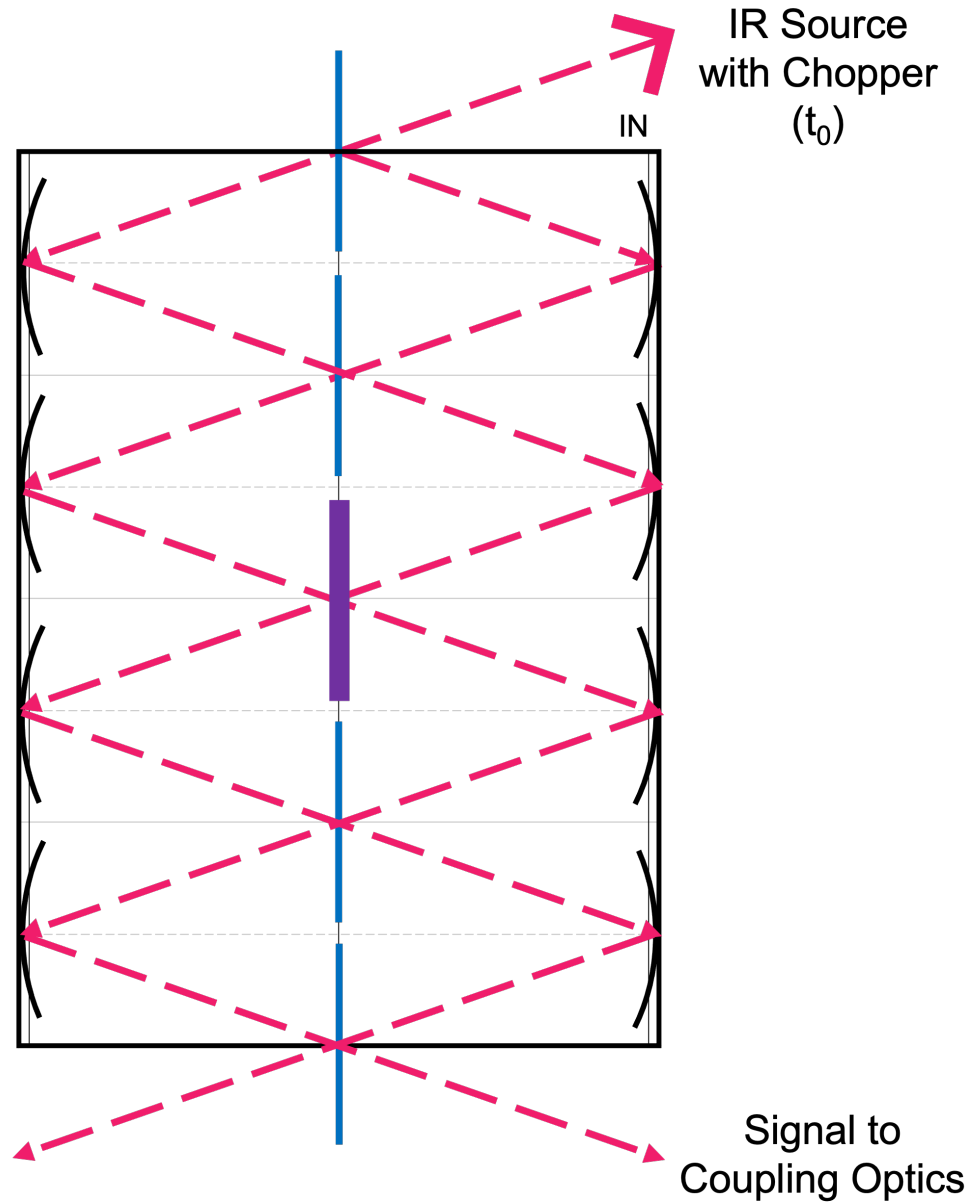
Figure 3.8: Simplified diagram of the PIXIE-style FTS used for AdvACT and SO, showing the beam paths that would eventually reach a detector. When any beam is incident on a wire-grid (blue), part will be reflected and part will be transmitted. The moving mirror surface, shown in purple at the center of the FTS, is parallel to the y-axis and travels along the x-axis. The dihedral mirror (purple) is two rooftop mirrors joined together. This design eliminates the need for two long perpendicular arms, making it much more compact than a traditional Martin-Puplett interferometer.

and the x-component is transmitted, splitting the beam:

$$\vec{E}_{L0} = A\hat{x} \qquad \vec{E}_{R0} = B\hat{y}, \qquad (3.27)$$

where L and R subscripts denote the left and right sides of the instrument, respectively. Each beam then reflects off a transfer mirror, flipping the x-component of the fields:

$$\vec{E}_{L1} = -A\hat{x} \qquad \vec{E}_{R1} = B\hat{y}. \qquad (3.28)$$

The next polarizer is oriented with its wires at a $45°$ angle, as seen by the incident radiation. (The wire grids are oriented at a $45.6°$ angle in the plane of the FTS center septum due to the $\sim 12°$ angle of incidence.) This polarizer reflects half the radiation and transmits half, imposing a new polarization basis that we will denote $\hat{u}$ and $\hat{v}$. The relationship between the $\hat{u}$, $\hat{v}$ basis and the $\hat{x}$, $\hat{y}$ coordinate system is

$$\hat{u} = (\hat{x} + \hat{y})/\sqrt{2}$$
$$\hat{v} = (\hat{x} - \hat{y})/\sqrt{2}, \qquad (3.29)$$

so we can rewrite Equations 3.28 in the new basis:

$$\vec{E}_{L1} = -A(\hat{u} + \hat{v})/\sqrt{2}$$
$$\vec{E}_{R1} = B(\hat{u} - \hat{v})/\sqrt{2}. \qquad (3.30)$$

The second polarizer is oriented to reflect the $\hat{u}$ polarization and transmit $\hat{v}$, so our left and right beams after the second polarizer are:

$$\vec{E}_{L2} = -(A\hat{u} + B\hat{v})/\sqrt{2}$$
$$\vec{E}_{R2} = (B\hat{u} - A\hat{v})/\sqrt{2}, \qquad (3.31)$$

and after reflection off the next transfer mirrors,

$$\vec{E}_{L3} = (B\hat{u} + A\hat{v})/\sqrt{2}$$

$$\vec{E}_{R3} = (A\hat{u} - B\hat{v})/\sqrt{2}.$$

(3.32)

Next, the beams reflect off a dihedral mirror, which is stepped to create an optical path difference. Each beam reflects twice off the dihedral mirror, leaving the x-component of the electric field unchanged, but flipping the y-component. For a step ξ to the right, the right beam path is shortened by 2ξ and the left beam path is lengthened by 2ξ, creating a phase delay. In the $\hat{x}$, $\hat{y}$ basis, the beams after reflection off the dihedral mirror are:

$$\vec{E}_{L4} = [(A + B)\,\hat{x} + (A - B)\,\hat{y}]\exp[-i2k\xi]/2$$

$$\vec{E}_{R4} = [(A - B)\,\hat{x} - (A + B)\,\hat{y}]\exp[i2k\xi]/2.$$

(3.33)

After reflecting off the third transfer mirror, the fields can be expressed in the $\hat{u}$, $\hat{v}$ basis as

$$\vec{E}_{L5} = -(B\hat{u} + A\hat{v})\exp[-i2k\xi]/\sqrt{2}$$

$$\vec{E}_{R5} = (-A\hat{u} + B\hat{v})\exp[i2k\xi]/\sqrt{2}.$$

(3.34)

The beams then meet the third polarizing wire grid, oriented to transmit the $\hat{u}$ polarization and reflect $\hat{v}$ (opposite of the second polarizer). After interacting with the third polarizer, the fields are

$$\vec{E}_{L6} = -A(\exp[i2k\xi]\,\hat{u} + \exp[-i2k\xi]\,\hat{v})/\sqrt{2}$$

$$= -A(\cos[2k\xi]\,\hat{x} + i\sin[2k\xi]\,\hat{y}),$$

(3.35)

and

$$\vec{E}_{R6} = -B(\exp[-i2k\xi]\,\hat{u} - \exp[i2k\xi]\,\hat{v}/\sqrt{2}$$

$$= B(i\sin[2k\xi]\,\hat{x} - \cos[2k\xi]\,\hat{y}).$$

(3.36)

Reflection off the final transfer mirror will again flip the x-component of each beam, and direct the beams to the 4th polarizer, which reflects $\hat{y}$ polarization and transmits $\hat{x}$ polarization (like the first wire grid). Our final recombined beams are then:

$$\vec{E}_{L7} = -i \sin\left[2k\xi\right] \left(B\hat{x} + A\hat{y}\right)$$

$$\vec{E}_{R7} = \cos\left[2k\xi\right] \left(A\hat{x} - B\hat{y}\right). \tag{3.37}$$

3.3.2 Analysis of output beams

A detector placed at either output of the FTS measures incident power in orthogonal polarization modes $\hat{x}$ and $\hat{y}$. For the purposes of AdvACT and SO, we only use one output of the FTS to calibrate our detectors; for an input beam incident from the right (as in Figure 3.8), we take the right output:

$$P_{Rx} = A^2 \cos^2\left[2k\xi\right] = \frac{A^2}{2}(1 + \cos\left[4k\xi\right])$$

$$P_{Ry} = B^2 \cos^2\left[2k\xi\right] = \frac{B^2}{2}(1 + \cos\left[4k\xi\right]). \tag{3.38}$$

Assuming an unpolarized input beam, such that $E_x = E_y = \frac{1}{2}E_0$, the fractional power measured by each detector is

$$F_{\text{out},x}(\xi) = \frac{1}{4}(1 + \cos\left[4k\xi\right])$$

$$F_{\text{out},y}(\xi) = \frac{1}{4}(1 + \cos\left[4k\xi\right]), \tag{3.39}$$

matching the output of the basic Michelson interferometer (Equation 3.24). While this design still has the additive constant of the Michelson equation, it is much more compact than the classic Martin-Puplett design, making it ideal for in-field measurements. This is the primary reason the PIXIE FTS was used for AdvACT and is planned for SO.

We couple the output of the FTS to detectors in the telescope receiver using a custom set of coupling optics, which focuses the FTS beam on the detector array

and fills the full solid angle of the detector feedhorns. For every step of the FTS dihedral mirror, we take a measurement with the detectors. We can then plot a single detector's response as a function of the mirror position or displacement ξ to obtain an interferogram. The analysis of interferograms will be discussed Chapter IV.

CHAPTER IV

Advanced ACTPol Measurements

Detector bandpass calibration data for AdvACT was taken in December 2016 on the HF (150/220 GHz) and MF (90/150 GHz) arrays using our first-generation PIXIE-style Fourier transform spectrometer (FTS) by the telescope site crew. Section 4.1 describes the instrumental set-up and measurements, and Section 4.2 gives an overview of the analysis methods I developed to process the interferograms and the resulting bandpasses. I identify several uncertainties present during the measurements that could be improved for future measurements, and present these with my final analysis results in Section 4.3.

4.1   Measurement Set-up

The Fourier transform spectrometer is mounted with its source, chopper wheel, and coupling optics on the AdvACT telescope in the configuration shown in Figure 4.1. To account for the angled output of the FTS, it is tilted to $24° \pm 1°$ on the mount so that the output is at normal incidence with the optics tube. A set of optics that couple the FTS signal to the receiver optics is shown in Figure 4.2. These coupling optics are attached to align with the FTS output, and positioned such that the final lens is approximately 5 inches from the window of the cryogenic optics tube. This positioning ensures that the output of FTS and coupling optics system is focused

on the detector focal plane. The assembly used for positioning the FTS and coupling optics can be seen in Figure 4.3.

The FTS chopper wheel is controlled by an Arduino that ramps up the frequency to 5 Hz for data acquisition. The thermal source is fixed in front of the chopper; two sources were used for the AdvACT measurements, shown in Figure 4.1. The heat lamp source emits 873 K radiation well-approximated by a blackbody. A cold source was also tested to investigate which source would produce better signal-to-noise (S/N). Eccosorb HR-10 is an absorber that is also well-approximated by a blackbody, and cooling it to liquid Nitrogen (LN2) temperatures can reduce thermal loading on the TES detectors. When comparing the cold load measurements to those taken with the heat lamp, we saw no significant improvement in the S/N. Moving forward, we only used heat lamp sources as they are easier to mount on the FTS. Measurements shown in this chapter were taken using a heat lamp source.

A laptop is used to control the FTS. It has the control software for the linear stage in the FTS, and a viewer code that aids in aligning the FTS to maximize the S/N. An Aerotech linear stage is used to step the central mirror inside the FTS. At the beginning of each measurement, the translating mirror is aligned with the row of wire-grids as a reference. The detector data is read out by the telescope control system (the MCEs). Code on these MCEs demodulates the chopped FTS signal picked up by the detectors and records the raw demodulated data.

While we only illuminate a portion of the detector array at a time with the FTS beam, the entire detector array is read out continuously. We step the FTS mirror discretely and integrate at each position, as opposed to continuously slewing the mirror; the discrete method is used to improve the S/N. Data was taken on AdvACT's HF and MF arrays at different positions to illuminate as many of the detectors as possible. Approximately 4% of the detectors are illuminated by each individual measurement.
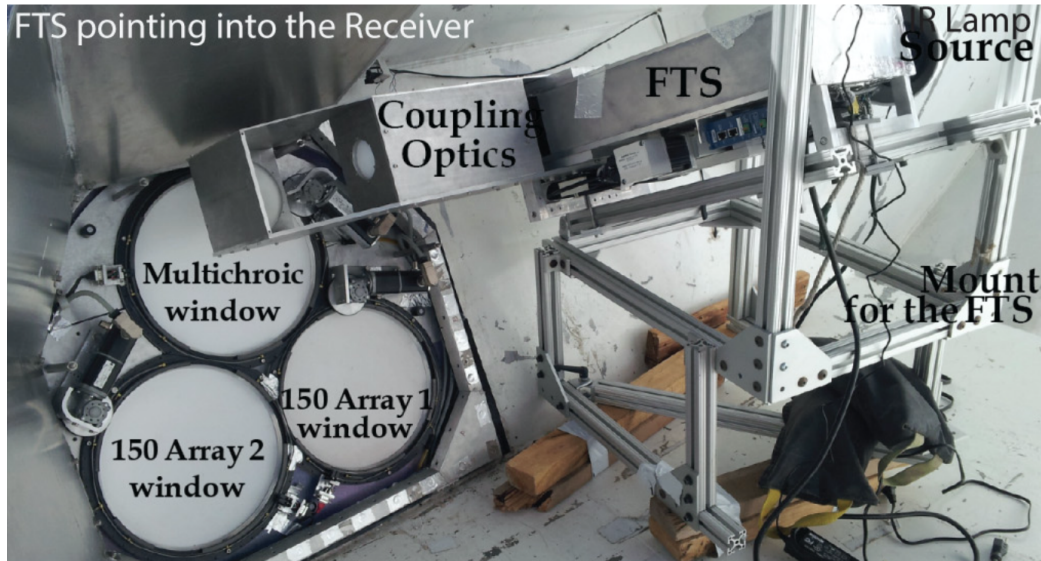
Figure 4.1: FTS and coupling optics set-up at the AdvACT site [55]. The FTS rests on a mount that angles such that the detectors are illuminated at normal incidence. The top image shows the set-up using a heat lamp source, and bottom shows the set-up using HR-10 Eccosorb immersed in LN2 as a cold source. Preliminary data analyses showed that both sources produced around the same S/N in the measurements. The heat lamp was used for subsequent measurements due to its convenience.
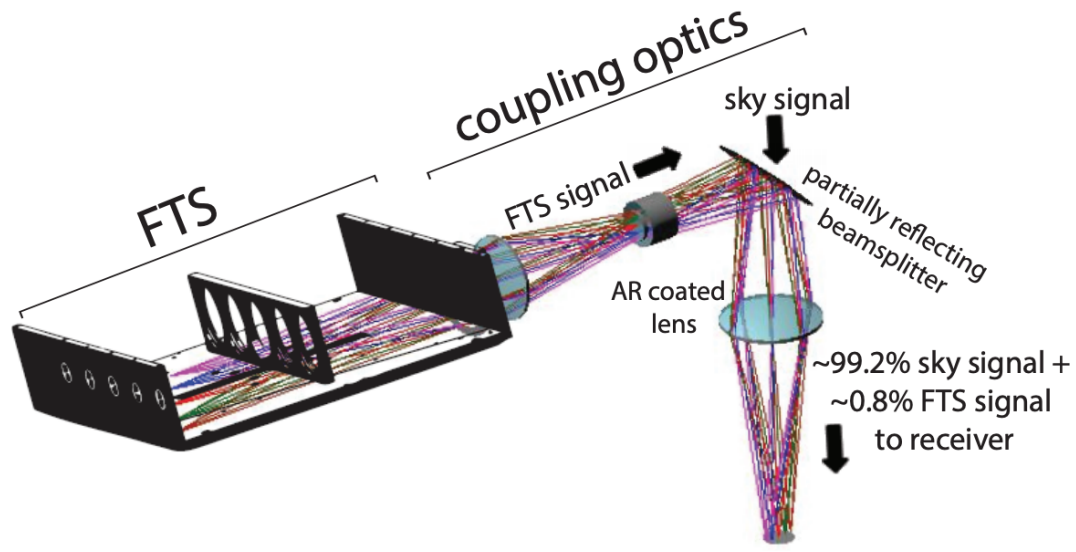
Figure 4.2: A 3D ray-trace diagram of the original ACT FTS and coupling optics system used to calibrate the ACT HF and MF detector arrays. Coupling optics were designed and built by Rahul Datta [55]. The 45° angled mirror in the coupling optics reflects only a small percentage (less than 1%) of the FTS beam into the telescope receiver so as to not saturate the sensitive TES bolometers. All lenses in the coupling optics are made of HDPE and are AR coated to minimize reflections within the system as much as possible.
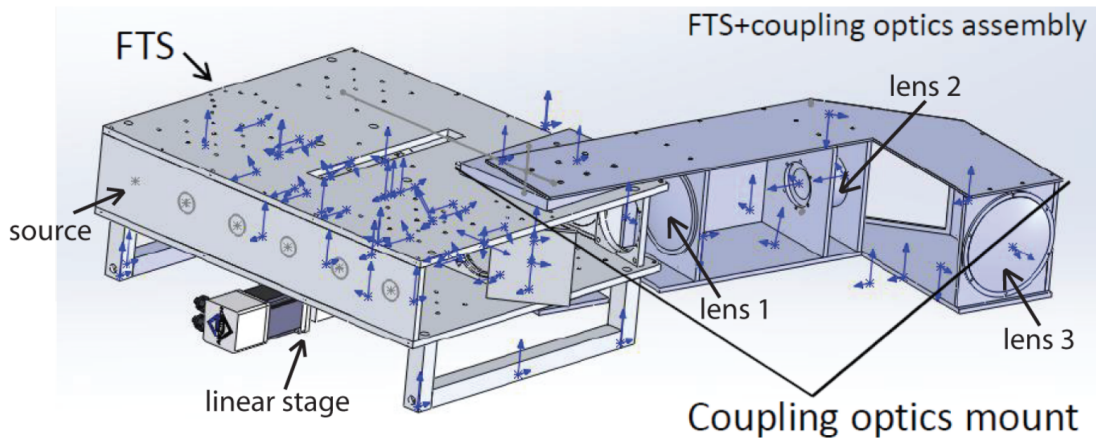
Figure 4.3: Drawing of the AdvACT FTS and coupling optics assembly [55]. Vectors in the figure represent surface normals of optical components and surfaces. The FTS is propped up with legs to make room for the linear stage underneath that controls the moving central mirror in the FTS. The last lens in the system, lens 3, is positioned about 5 cm away from the optics tubes housing the detector arrays.

4.2 Bandpass Analysis

Measurements were taken at six different locations on the AdvACT HF array (PA4), and several sets of measurements were taken at each location. Measurements were taken at two locations on PA2 (a monochroic array) and PA3. The FTS illuminates about 4% of the detector array for each measurement. The patches of illuminated detectors seen in Figures 4.11, 4.12, and 4.13 show the different measurement locations on each array. High-resolution, low-frequency measurements were taken by stepping the FTS mirror a total distance on the order of $10 - 100$ mm, using steps on the order of 0.1 mm; this process takes around 10 minutes to complete.

My data analysis includes the FTS analysis processes outlined in Chapter III and adds additional steps to account for the complexity of real data.

4.2.1 Filtering and cut statistics

Since we collect data (interferograms) from all the detectors on an array at once, we must filter out only the detectors that were sufficiently illuminated by the FTS before processing the dataset. I developed a Python program to sort through FTS data and identify which detector channels had been illuminated. This filtering is completed in three stages:

1. **Interferogram S/N cut:** I sorted raw interferograms by comparing the root mean square (RMS) of the middle two quarters of the interferogram where the signal is expected to peak to the RMS of the outside quarters. I used a cutoff ratio of 2.5 to identify interferograms:

$$\frac{(\text{Central Quarters})_{\text{RMS}}}{(\text{Outside Quarters})_{\text{RMS}}} > 2.5. \tag{4.1}$$

This cut statistic was empirically tuned to ensure only interferograms with sufficient S/N were analyzed.

2. **Sorting bands:** Since we read out the full dichroic focal plane of the AdvACT instrument, we must sort the passbands into their respective frequency bands. After Fourier transforming the interferogram data to obtain a passband (as discussed in Section 3.2.2), I roughly defined four detector tophat bands: 40 GHz (spanning $30 - 50$ GHz and used for comparison purposes in the analysis), 90 GHz ($70-120$ GHz), 150 GHz ($120-180$ GHz), and 220 GHz ($175-280$ GHz). I then calculated the normalized mean power of each passband within the four defined bands and sorted passbands using the following criteria:

$$\frac{(220 \text{ Band})_\text{avg}}{(220 \text{ Band})_\text{max}} > \frac{(150 \text{ Band})_\text{avg}}{(220 \text{ Band})_\text{max}} \text{ identifies a 220 GHz band,}$$

$$\frac{(150 \text{ Band})_\text{avg}}{(150 \text{ Band})_\text{max}} > \frac{(90 \text{ Band})_\text{avg}}{(150 \text{ Band})_\text{max}} \text{ identifies a 150 GHz band, and}$$

$$\frac{(90 \text{ Band})_\text{avg}}{(90 \text{ Band})_\text{max}} > \frac{(40 \text{ Band})_\text{avg}}{(90 \text{ Band})_\text{max}} \text{ identifies a 90 GHz band.}$$

These cuts eliminated data that did not produce a passband when Fourier transformed and sorted the passbands by frequency.

3. **Passband S/N cut:** Some detectors that were partially illuminated or illuminated from an angle produced spectra that made it through the first two cuts while still having low S/N. The low S/N is caused by a slanted bandpass shape from poor detector illumination. I used two final cut statistics to eliminate these bands from further analysis. Due to the chosen normalization, unusable data tended to have higher values in the high-frequency tail. I eliminated bands where the average power in the high-frequency tail was greater than 0.35. Lastly, I cut bands whose average in-band power was less than 0.4, successfully eliminating the rest of the low S/N detector measurements.

4.2.2 Removing large outlier spikes from raw interferograms

Spurious noise during data acquisition can cause peaks in the interferograms that are several orders of magnitude larger than surrounding features. These dominant spikes strongly impact the Fourier transformed data, so we mask them carefully before processing the data.

I filter through the interferogram data and detect spikes using a cut statistic that compares each value in the data to the RMS of the rest of the data:

$$\frac{\text{Value}}{(\text{Remaining Data})_{\text{RMS}}} > 8. \tag{4.2}$$

When an extreme value meets this criterion, it is replaced with the average of its two neighbor values, thereby masking large spikes in the interferogram.

4.2.3 Subtracting baseline polynomials from interferograms

Various atmospheric conditions and slow drifts in the timestream during data collection can cause a baseline polynomial dependence in the measured interferogram. This baseline arises in a wide variety of spectroscopic applications and can cause issues in analysis and interpretation. I correct for this baseline dependence while preserving the interferogram features by fitting a 7th-order polynomial function to the data and subtracting the fit function. The effect of this correction is illustrated in Figure 4.4

4.2.4 Apodization

Our interferograms are finite sets of data, which we can alternatively describe as infinitely long interferograms that have been truncated. This truncation introduces leakage when Fourier transforming the data.

We can mathematically describe a truncated interferogram, $F(x)$, as the product of an infinite interferogram $G(x)$ and a boxcar function $H(x)$, which has a value of 1
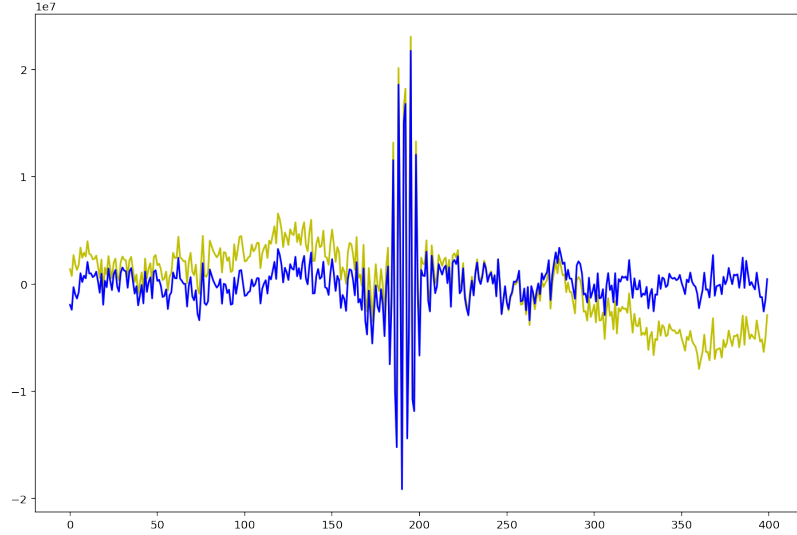
Figure 4.4: An interferogram before (yellow) and after (blue) polynomial subtraction. A 7th-order polynomial is fit to the raw interferogram data and subtracted.

over the optical path of the truncated interferogram and 0 elsewhere (see Figure 4.5):

$$F(x) = G(x) \cdot H(x). \tag{4.3}$$

By convolution theorem, when we take the Fourier transform of the product of two signals, we get the convolution of their individual Fourier transforms:

$$\mathcal{F}\{F(x)\} = \mathcal{F}\{G(x) \cdot H(x)\} \tag{4.4}$$

$$= \mathcal{F}\{G(x)\} \otimes \mathcal{F}\{H(x)\}. \tag{4.5}$$

The Fourier transform of the boxcar function is shown in Figure 4.5. When this is convolved with the Fourier transform of an infinite interferogram—the true bandpass, illustrated as a tophat band in Figure 4.6—the result is not a true representation of just the detector bandpass, as can be seen in Figure 4.7. This leakage can be mitigated by apodizing our interferograms, so they taper to zero signal smoothly.

We choose an "apodization window" to reduce the effects that the boxcar function
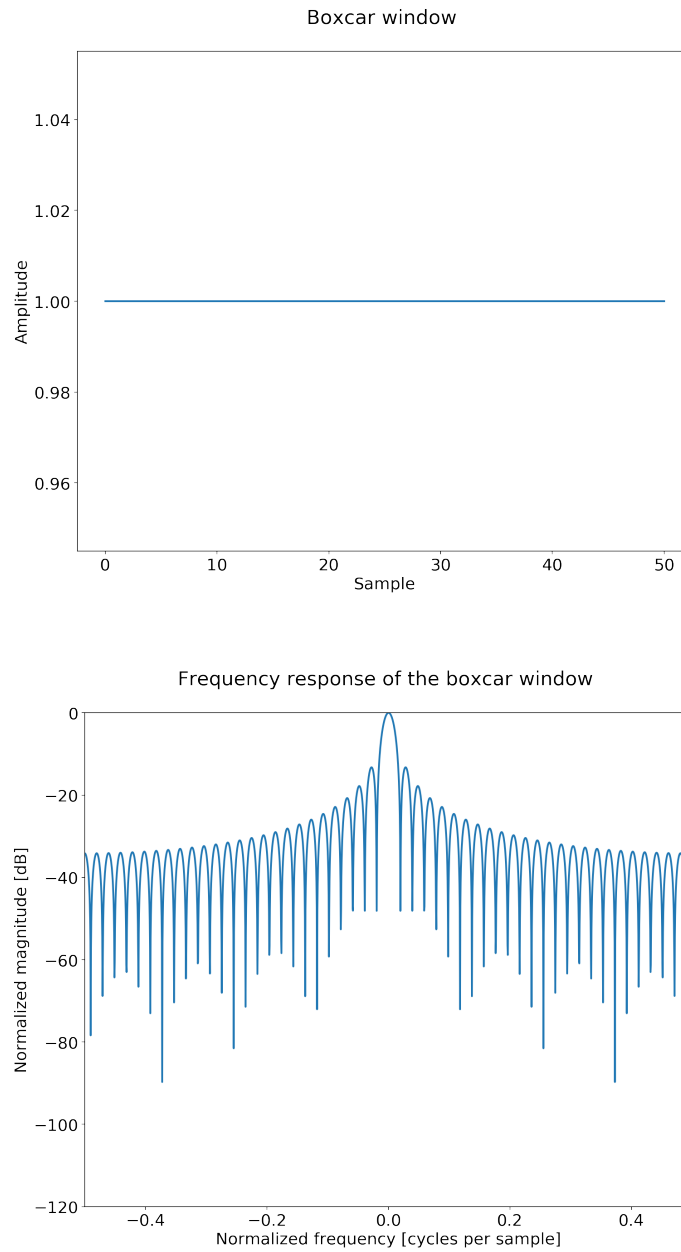
Figure 4.5: The boxcar window *(top)* and its frequency response *(bottom)*. The result of the FFT of a finite interferogram will be a convolution of the actual bandpass and this frequency response function.
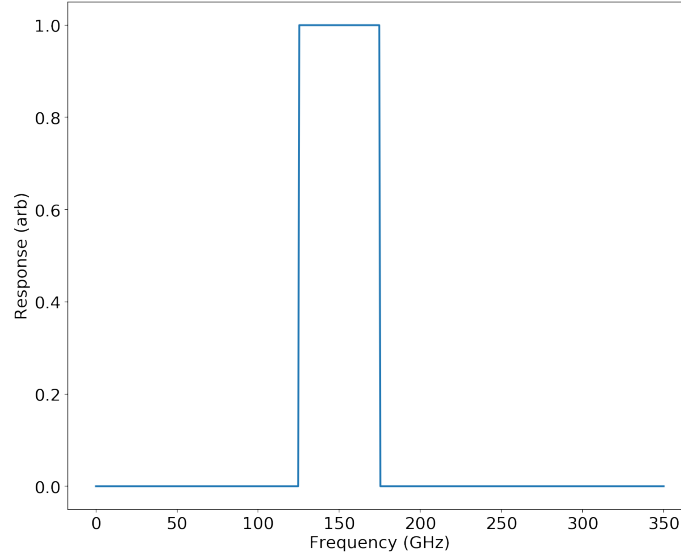
Figure 4.6: A simulated "perfect" bandpass for a 150 GHz detector—the tophat band.
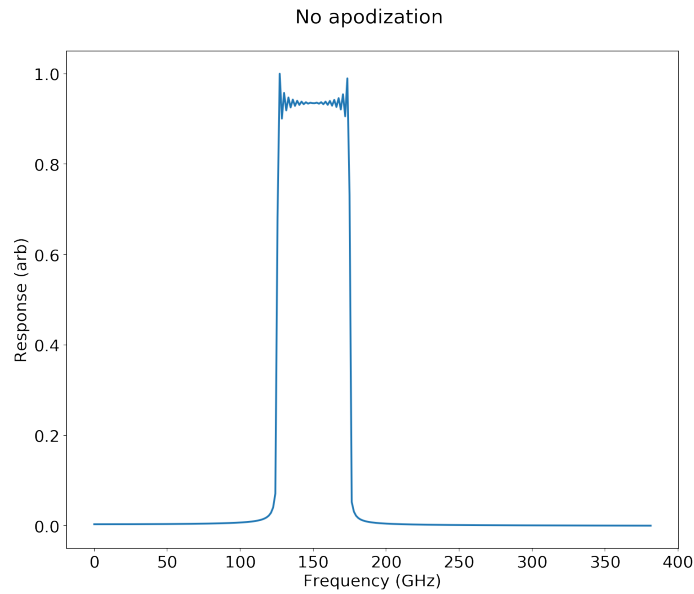
Figure 4.7: FFT of the interferogram with no apodization (or, apodized by the boxcar function). We can see notable distortion of the band shape at the top of the band caused by leakage. This is much less representative of the true band shape than the apodized result in Figure 4.9.

truncation has on the Fourier transform. The apodization window is a function chosen for its ability to reduce sidelobes in the Fourier transform. For the AdvACT data analysis, I apply the window function

$$w(x) = \left(1 - x^4\right)^2 \qquad -1 \le x \le 1, \tag{4.6}$$

shown with its Fourier transform in Figure 4.8. When we apodize with the $(1 - x^4)^2$ window, we see significant reduction of the distortion at the top of the band, shown in Figure 4.9

4.2.5 Fourier transformation and phase correction

I then Fourier transform the apodized interferogram using a DFT, as discussed in Section 3.2.3. In general, the Fourier transform of an interferogram will produce a complex spectrum $C(\nu)$ rather than a real spectrum $S(\nu)$, because the input to the Fourier transform is not perfectly symmetric about $x = 0$ due to several systematic factors [73]. The complex spectrum can be represented as the sum of a purely real spectrum and a purely imaginary spectrum:

$$C(\nu) = R(\nu) + iI(\nu), \tag{4.7}$$

Or alternatively as the product of a real amplitude spectrum $S(\nu)$ and a complex exponential:

$$C(\nu) = S(\nu)\, e^{i\phi(\nu)}, \tag{4.8}$$

where ϕ is the frequency-dependent phase. This phase can be calculated from the quantities expressed in Eq. 4.7 using the following relation

$$\phi(\nu) = \tan^{-1}\left[\frac{I(\nu)}{R(\nu)}\right]. \tag{4.9}$$
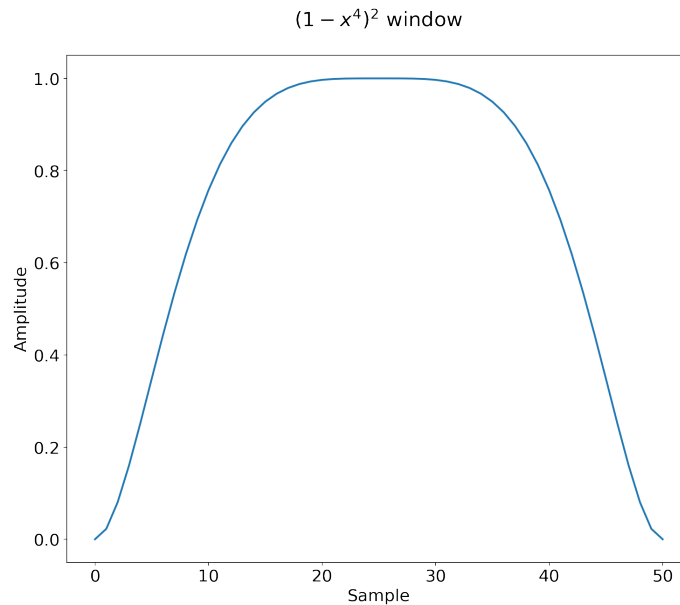
(a) The $(1 - x^4)^2$ apodization window used in AdvACT FTS analysis. We multiply our finite interferogram by this function to reduce leakage.
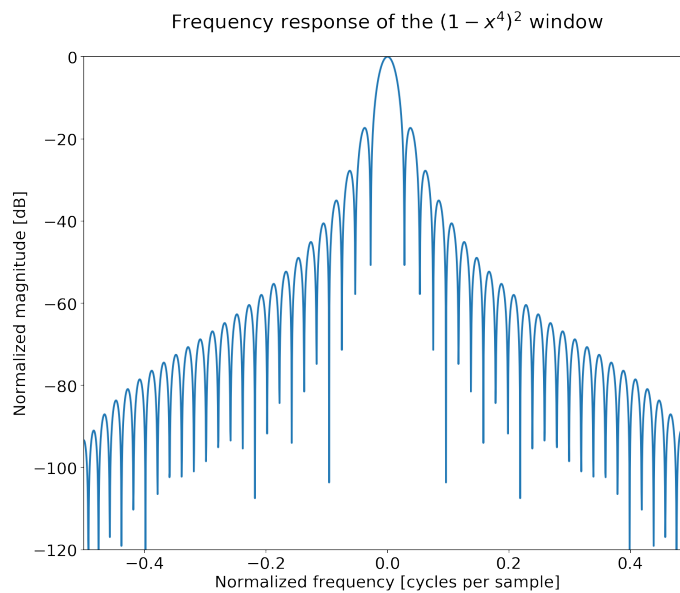
(b) Frequency response of the $(1 - x^4)^2$ window. Note the significant sidelobe suppression compared to the response of the boxcar window shown in Figure 4.5. The result of this suppression is shown in Figure 4.9.

Figure 4.8: The $(1 - x^4)^2$ apodization window and its frequency response.

With $(1 - x^4)^2$ apodization
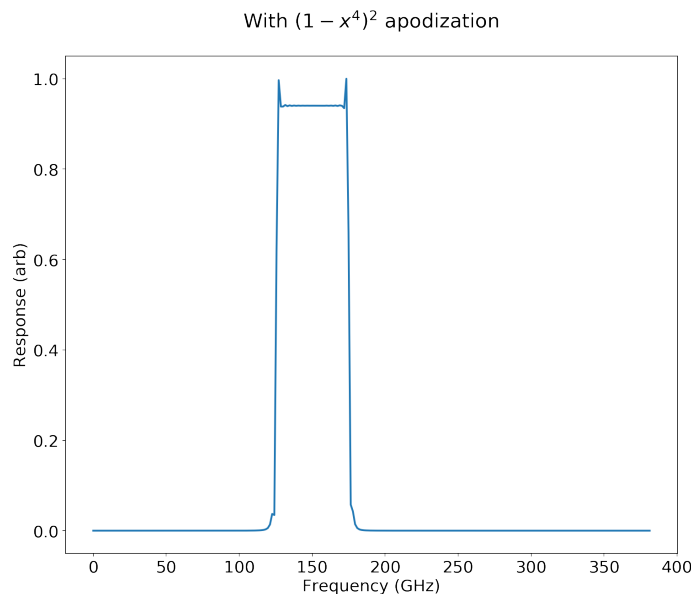
Figure 4.9: FFT of the interferogram apodized by the function $(1 - x^4)^2$. Aside from a few minor defects, this result is representative of the true shape of the actual bandpass.

I thus extract the true amplitude spectrum $S(\nu)$ from the complex output of the DFT $C(\nu)$ by applying a phase correction to $C(\nu)$:

$$S(\nu) = C(\nu) \, e^{-i\phi(\nu)}. \tag{4.10}$$

4.2.6 Correcting bandpass for Rayleigh-Jeans effect

The bandpass also needs to be corrected for the Rayleigh-Jeans spectrum of the source and ambient temperature of the room. We do this by dividing the bandpass spectrum by the following factor

$$RJ = \frac{2\nu^2 k_B}{c^2} \left(T_S - T_A \right), \tag{4.11}$$

where T_A is the ambient temperature and T_S is the temperature of the source, about 873 K. The effect of this correction can be seen in Figure 4.10. We can see that correcting for the thermal nature of the source induces a sloping low-frequency tail
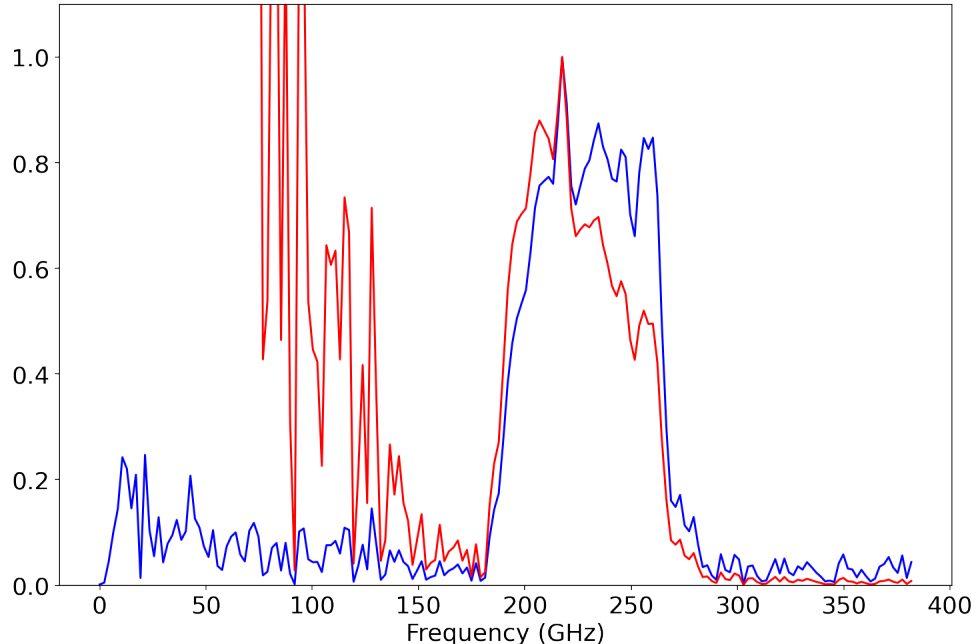
Figure 4.10: A 220 GHz bandpass before (blue) and after (red) correcting for the Rayleigh-Jeans nature of our heat lamp source. The correction introduces a decaying low-frequency tail outside the band.

because our detector response at low frequencies is not zero (as would be for an ideal tophat detector bandpass). This Rayleigh-Jeans correction causes a shift in the calculated weighted band centers (discussed in Section 4.3.1) and bandwidths (described in Section 4.3.2) on the order of $1-3\%$. The slopes in the bandpasses from uneven illumination of the spectra that pass the S/N criteria are also on order $1-3\%$.

4.3   Results

Accurate removal of dominating polarized foregrounds from CMB maps heavily relies on precise knowledge of our detector band centers. Foregrounds include contributions from dust and synchrotron radiation. Here I discuss how I calculate the weighted band centers and bandwidths for each type of foreground component, as well as the CMB spectrum, and discuss the current sources of uncertainties in our measurements.

4.3.1 Calculating detector weighted band centers

Our effective detector band centers can be calculated from the detector bandpasses (spectral response) using the following:

$$\nu_e = \frac{\int \nu \, f(\nu) \, \sigma(\nu) \, \nu^{-2} \, d\nu}{\int f(\nu) \, \sigma(\nu) \, \nu^{-2} \, d\nu}, \tag{4.12}$$

where $f(\nu)$ is the detector response as a function of frequency, $\sigma(\nu)$ is the frequency dependence of the spectral energy density (SED) of the source of interest, and the factor of ν^{-2} is introduced to account for the elliptical geometry of the FTS mirrors.

Foreground sources such as synchrotron radiation and dust have unique spectral dependencies, causing differing weighted band center measurements between sources. Dust is a thermal source with a temperature of 19.6 K (i.e. a 19.6 K blackbody). In the $0 - 400$ GHz range, this blackbody is well-approximated by a simple power law,

$$\sigma_{\mathrm{dust}}(\nu) = \nu^{1.53}, \tag{4.13}$$

where $\beta_d = 1.53 \pm 0.02$ is called the "spectral index" for dust [37]. Synchrotron polarized emission also follows power law SED at microwave frequencies with spectral index $\beta_s = -3.22 \pm 0.08$ [74]:

$$\sigma_{\mathrm{synch}}(\nu) = \nu^{-3.22}. \tag{4.14}$$

In this analysis we approximate $\beta_s = -3$ as in the Planck 2018 analysis [37]. Lastly, polarized CMB radiation has a 2.73 K blackbody SED in the microwave domain:

$$\sigma_{\mathrm{CMB}}(\nu) = \frac{\nu^3}{\exp\left[h\nu/k_B(2.73\mathrm{K})\right] - 1}. \tag{4.15}$$

Table 4.1 shows AdvACT's average weighted band centers for various foreground

Summary of AdvACT Detector Array Measurements					
Array	Nominal Band	Central Frequency by Source (GHz)			Bandwidth (GHz)
		Synchrotron	Dust	CMB	
PA2	150 GHz	140.33 ± 1.03	146.31 ± 0.94	140.72 ± 0.72	51.42 ± 1.39
PA3	90 GHz	87.82 ± 2.64	93.77 ± 2.67	93.51 ± 1.99	39.09 ± 2.66
	150 GHz	139.55 ± 2.85	143.87 ± 2.84	140.07 ± 2.39	43.66 ± 2.53
PA4	150 GHz	140.80 ± 1.77	145.70 ± 1.61	141.18 ± 1.36	46.44 ± 2.85
	220 GHz	210.19 ± 2.92	220.46 ± 3.51	223.59 ± 2.74	84.36 ± 5.05

Table 4.1: Average detector measurement results for the AdvACT PA2, PA3, and PA4 arrays. Most FTS measurements were taken on PA4 (152 150-GHz bands and 223 220-GHz bands, shown in Figures 4.12 and 4.13, respectively), while PA2 and PA3 produced much noisier results in addition to having fewer FTS measurements to begin with. PA2 results were calculated from 49 150-GHz bands, and PA3 results were calculated from 31 90-GHz bands (shown in Figure 4.11) and 38 150-GHz bands. Average bandpasses for PA3 and PA4 can be seen in Figures 4.14, 4.15, and 4.16.

spectra from the HF and MF arrays. The center frequency was calculated from the average bandpass (dicussed in Section 4.3.3) and uncertainties are the standard deviation of the individual detector weighted band centers.

Figures 4.12 and 4.13 display individual band center measurements across the HF array using the CMB as the source $\sigma(\nu)$. Each cluster of illuminated detectors represents a set of data taken at a single FTS position. Each measurement cluster shows a clear spatial gradient across the set, which can be caused by errors in our FTS alignment and/or uneven illumination of the feedhorns.

4.3.2 Detector bandwidth

The bandwidth is calculated using the Dicke bandwidth [75]:

$$\Delta \nu = \frac{\left[\int f(\nu) \, d\nu \right]^2}{\int f(\nu)^2 \, d\nu}. \tag{4.16}$$

Bandwidth measurements across the PA3 and PA4 arrays are shown in Figures 4.11, 4.12, and 4.13, and average bandwidths can be seen in Table 4.1, where again uncertainties represent the standard deviation of individual bandwidth measurements.
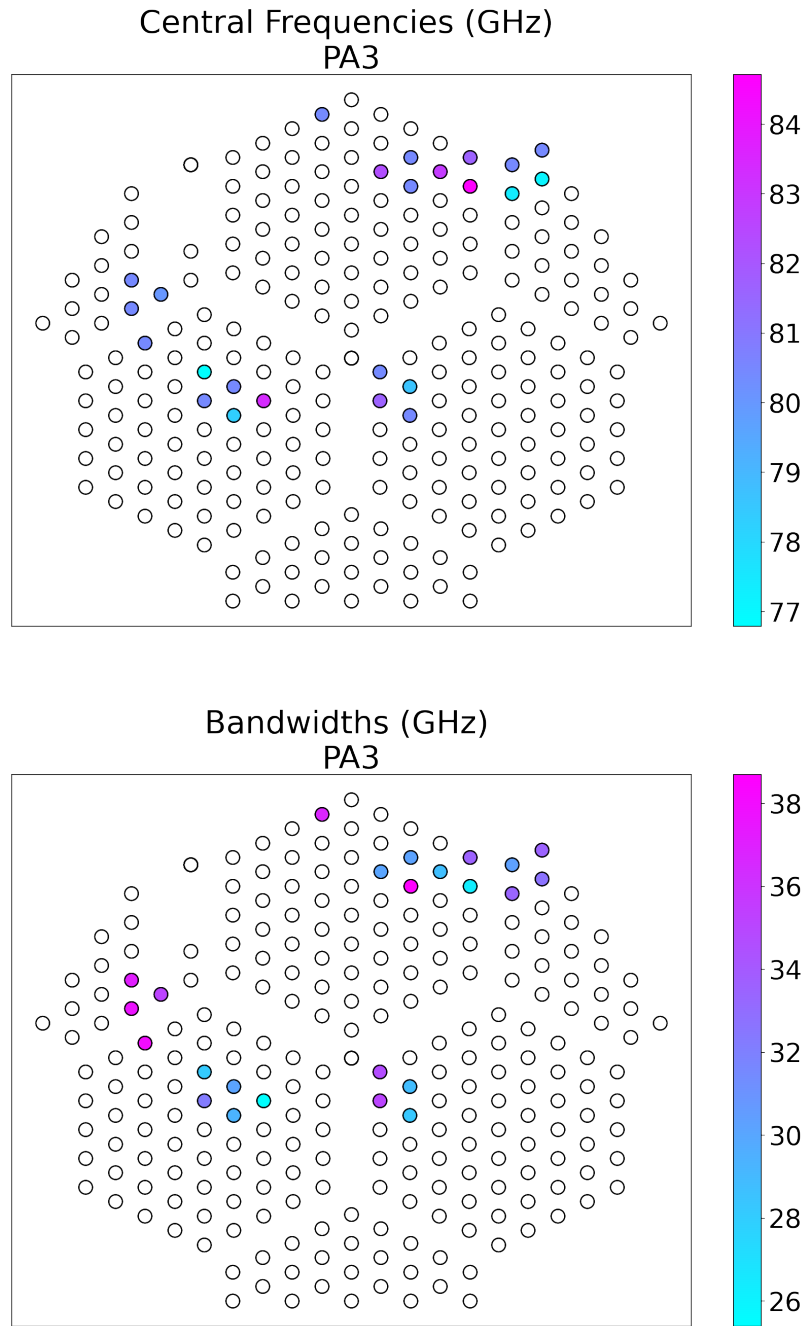
Figure 4.11: Measurements of 90 GHz detector central frequencies (with σ_{CMB}) *(top)* and bandwidths *(bottom)* plotted at their locations on the AdvACT MF array (PA3). Each cluster of measurements is a different FTS positioning (i.e. a separate measurement).
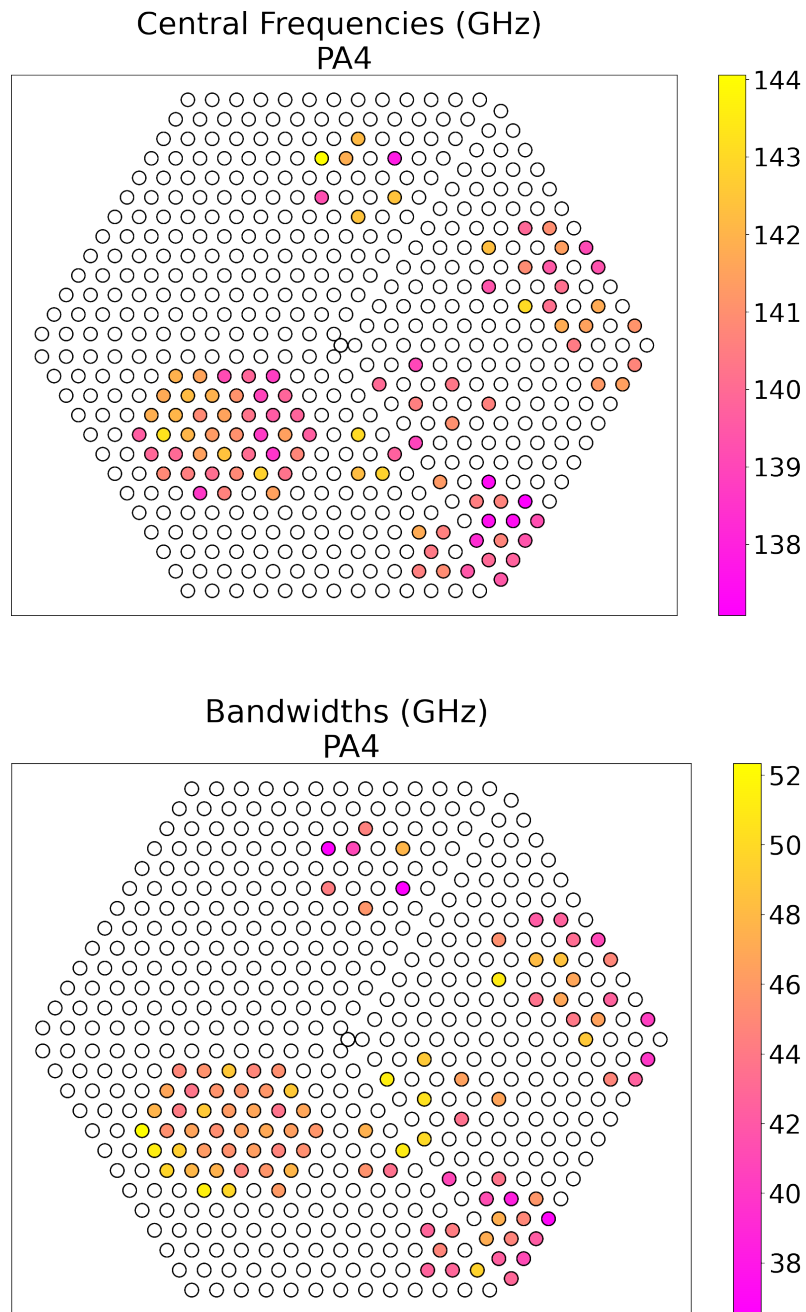
Figure 4.12: Measurements of 150 GHz detector central frequencies (with σ_{CMB}) *(top)* and bandwidths *(bottom)* plotted at their locations on the AdvACT HF array (PA4). Each measurement taken with the original ACTPol FTS only illuminates ~4 % of the array, assuming all data is useable (i.e. the illuminated detectors aren't oversaturated and have high S/N). In practice, much less than 4% of the array is illuminated per measurement as can be seen in 5 out of 6 of the above array measurements.
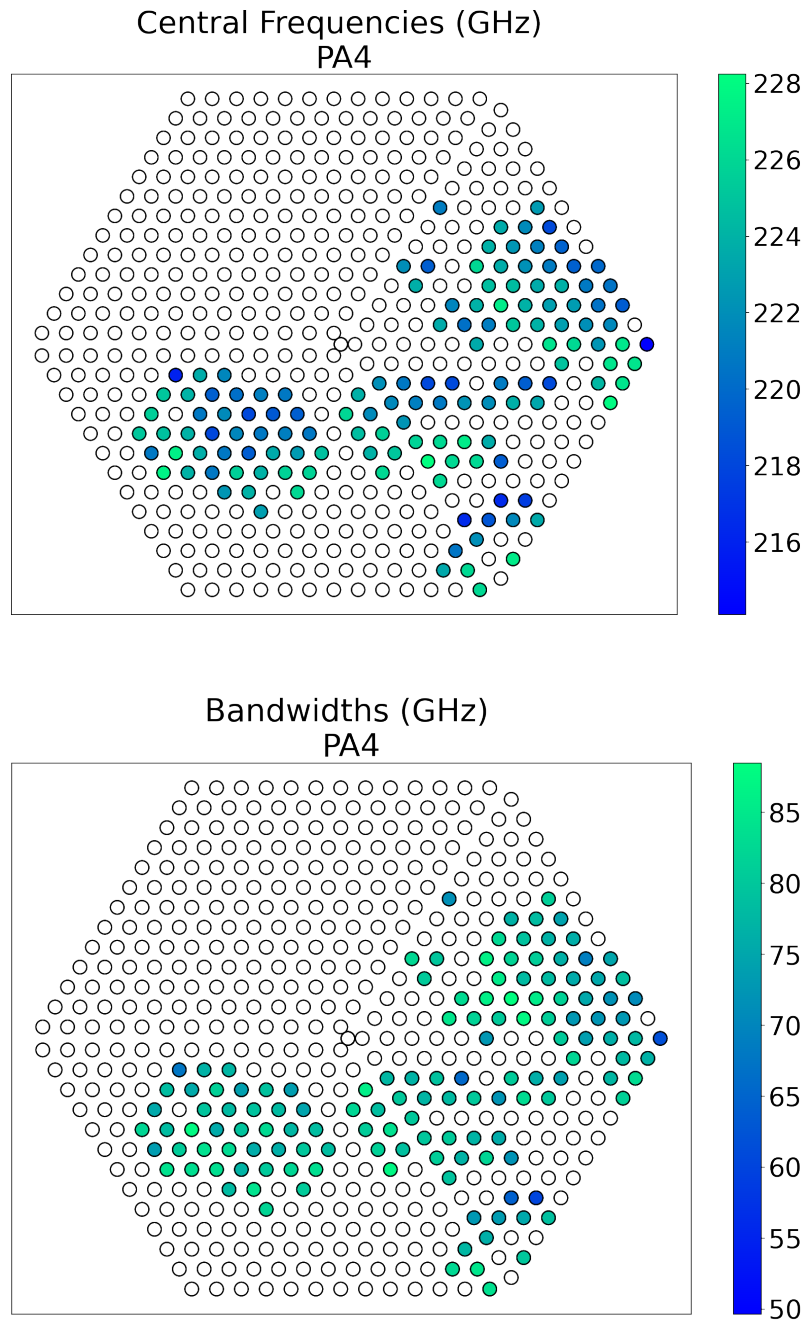
Figure 4.13: Measurements of 220 GHz detector central frequencies with(σ_{CMB}) *(top)* and bandwidths *(bottom)* plotted at their locations on the AdvACT HF array. There appears to be a strong spatial variation in each measurement, indicating the presence of systematic errors likely due to the inconsistency in the positioning of the FTS during measurements.
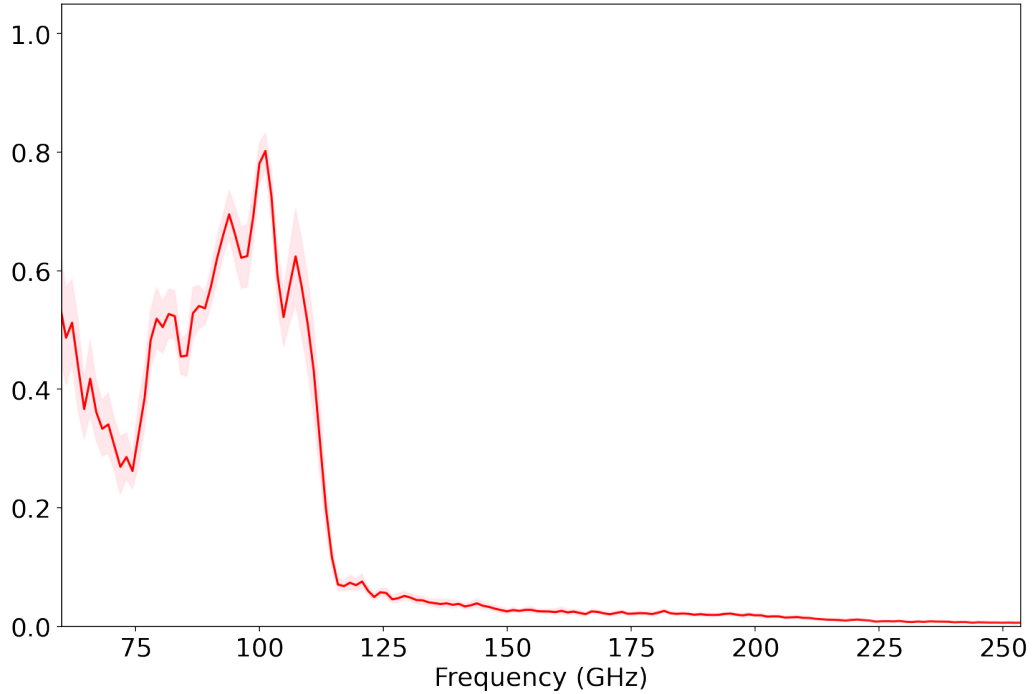
Figure 4.14: Average 90 GHz bandpass for the AdvACT MF array (PA3), shown with 95% confidence limits.

4.3.3 Average bandpasses

All detector measurements were averaged to produce an average bandpass for each AdvACT array. These are shown in Figures 4.15 and 4.16 with their 95% confidence limits. Confidence limits were calculated using the bootstrapping method, which iteratively resamples the data set randomly to infer characteristics of a full "population" (all the detectors on an array) only using sample data (our few illuminated detectors on each array). The low-frequency tail that we see in these average bandpass plots are due to the Rayleigh-Jeans bandpass correction amplifying low frequency noise. We neglect this low-frequency tail by constraining our integration limits as we are primarily concerned with in-band power.
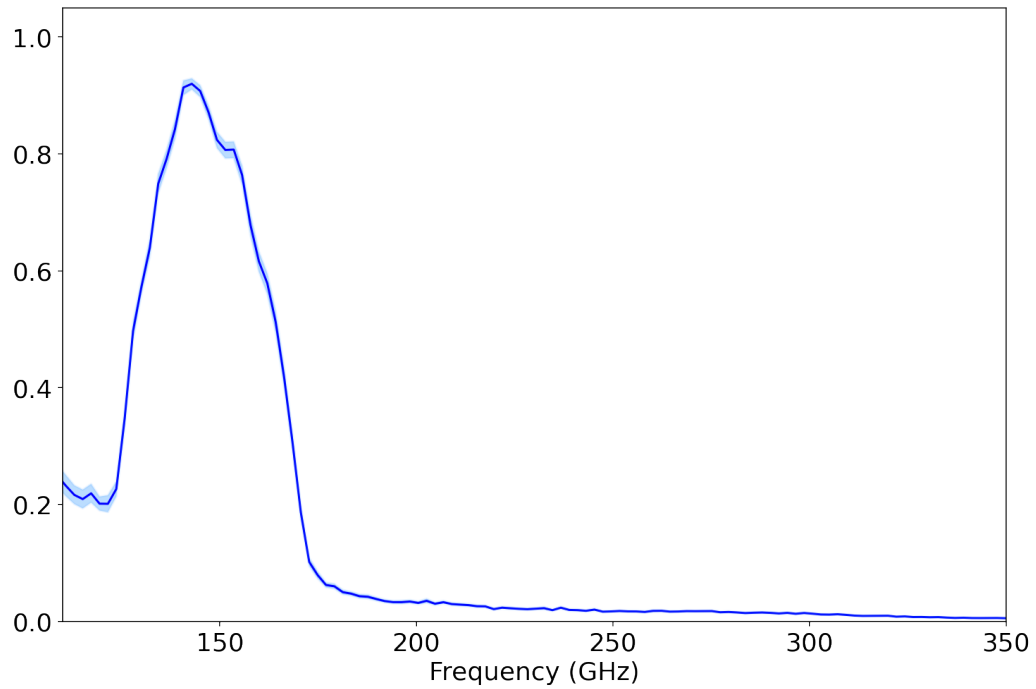
Figure 4.15: Average 150 GHz bandpass for the AdvACT HF array (PA4), shown with 95% confidence limits.
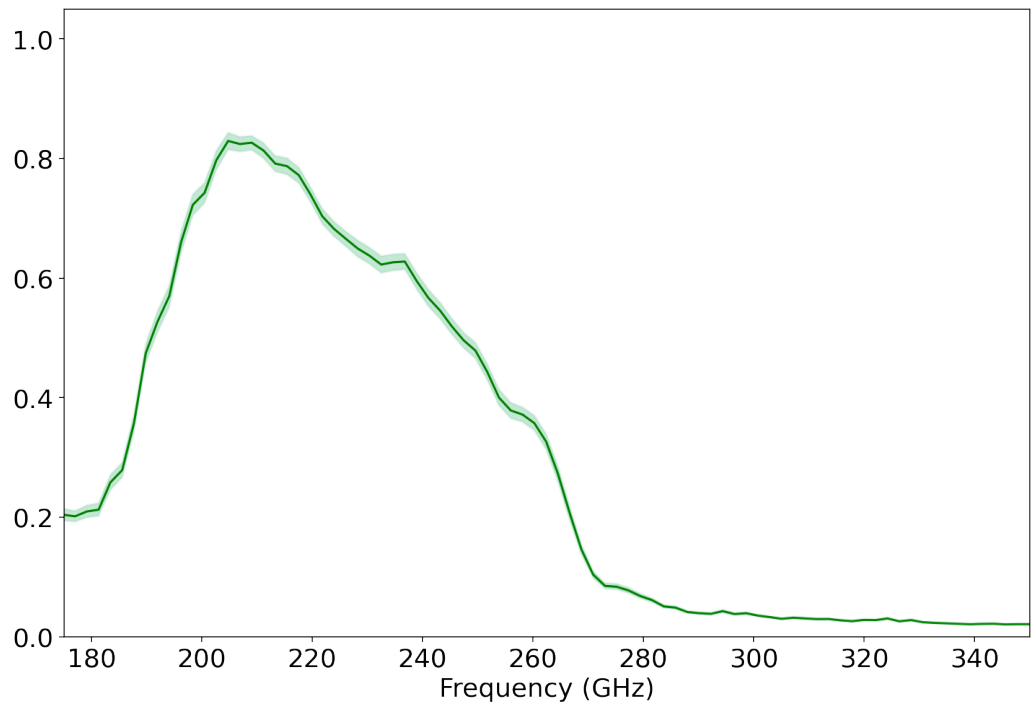
Figure 4.16: Average 220 GHz bandpass for the AdvACT HF array (PA4), shown with 95% confidence limits.

4.3.4 Potential measurement improvements

The FTS and coupling optics system shown in Figure 4.2 were sufficient for AdvACT data analysis; however, there are many sources of uncertainty in this setup that must be addressed as we move forward with SO and future CMB experiments. Figures 4.12 and 4.13 show that we are only illuminating about 4% of the detector array in each set of FTS measurements. If the FTS isn't aligned perfectly, off-axis illumination of the detectors can also cause distortion and angular dependence in our bandpass measurements. The FTS must be carefully positioned to minimize these effects and maximize the number of illuminated detectors, but we currently do not have a well-controlled positioning system for taking these measurements. The FTS and coupling optics are also quite heavy (around 30 kg), which greatly limits our ability to align the FTS for multiple quality measurements. Future experiments will need to characterize $\sim 10 - 100$ times the detectors with higher precision and more efficiently, so optical coupling designs that can illuminate more of the focal plane more evenly and improved positioning systems will be required.

The AdvACT FTS design uses a set of refractive coupling optics with high-density polyethylene (HDPE) lenses. The plastic lenses do not have perfect signal transmission. There are unwanted internal reflections at each lens surface, and the lenses absorb parts of the signal and re-radiate thermal emission. Because our detectors are kept at their superconducting transition state, any amount of excess thermal radiation will impact our sensitive measurements. The limited space at the site also constrains our optical design choices, requiring the very last lens in the coupling optics to be pushed as close to the cryogenic receiver window as possible. This is not ideal, and increases uncertainty in our measurements. Reflective coupling optics with no lenses could potentially improve performance.

The construction of the FTS and any misalignments within the system will also contribute to our measurement errors. The fragile, circular wire-grid polarizers are

difficult to produce with the desired wire spacing (100 μm). Inconsistencies in the wire spacing and alignment can cause frequency-dependent beam splitting, complicating the system's transfer function. The assembly is very delicate, as slight tilts in the parallel mirror totems and wire grid septum change our FTS output signal significantly. For future experiments, we will need to understand the form of the FTS signal, so we can remove systematic effects from the FTS itself from the bandpass calibrations. This will enable the precise calibration of our detector bandpasses and the successful removal of polarized foregrounds from CMB maps.

Moving forward, we need to upgrade the FTS system to mitigate these sources of uncertainty. We will use a fully motorized linear stage mount to position the FTS so we can illuminate the full focal plane at normal incidence. We will also switch to all reflective coupling optics to minimize internal reflections, illuminate more detectors, and reduce thermal loading. We can improve the FTS system's alignment tolerances for a more precise and secure hold on all optical elements to keep them consistently aligned. We will also fully characterize the transfer function of the FTS and coupling optics to account for their effects on our measurements. We plan to incorporate all these improvements into our SO FTS and coupling optics design. In Chapter V, I will explore the feasibility of these changes for future CMB experiments like SO.

CHAPTER V

Precision Fourier Transform Spectrometer

Based on results from ACTPol and similar experiments, the current bandpass calibration level achieved is $\sim 3\%$. If we marginalize over systematics, this bandpass uncertainty level could be sufficient for the SO SATs [67]. However, it will not be sufficient for the SO LAT and next-generation experiments like CMB-S4 that are significantly more sensitive. Table 5.1 shows the calibration requirements compared to our current abilities. To lower the bandpass uncertainty to the unprecedented levels required by the SO LAT and next-generation experiments, we must make several improvements to our Fourier transform spectrometer (FTS) design, coupling optics, and characterization methods to reduce all possible systematic effects introduced by the calibration system itself. In this section, I discuss initial steps I have taken to address these measurement challenges, and I assess the feasibility of these methods for improving future FTS measurements.

5.1 FTS Transfer Function Characterization

Characterizing the transfer function of the Fourier transform spectrometer to high precision is key to pushing the uncertainty in detector bandpass measurements to the sub-percent level. To see why transfer functions are useful in Fourier transform spectroscopy, we start with the superposition integral for an invariant system, which

SO Bandpass Calibration Measurement Requirements			
Frequency Band	Current Ability	$\Delta r \simeq 10^{-3}$	$\Delta r \simeq 2 \times 10^{-4}$
LF	—	6.70%	2.20%
MF	$1 - 3\%$	0.90%	0.33%
UHF	$1 - 3\%$	0.46%	0.20%

Table 5.1: Calibration requirements for the LF (27/39 GHz), MF (93/145 GHz), and UHF (225/280 GHz) detector bands [67] compared to our current calibration ability (estimated from Chapter IV).

describes an invariant optical system's output g_2 at position (x_2, y_2) as a function of the input g_1 and the point-spread function (or impulse response) h of the system:

$$g_2(x_2, y_2) = \int \int g_1(\xi, \eta) \, h(x_2 - \xi, y_2 - \eta) \, d\xi \, d\eta \tag{5.1}$$

where ξ and η are position variables integrated over the input beam area. Identifying the 2D or spatial convolution relation

$$f(x, y) \otimes g(x, y) = \int \int f(\xi, \eta) \cdot g(x - \xi, y - \eta) \, d\xi \, d\eta \tag{5.2}$$

we can rewrite Equation 5.1 as

$$g_2 = g_1 \otimes h. \tag{5.3}$$

This relation takes a much simpler form after Fourier transformation:

$$G_2(f_X, f_Y) = H(f_X, f_Y) \, G_1(f_X, f_Y) \tag{5.4}$$

where G_1 and G_2 are the Fourier transforms of the input g_1 and output g_2, respectively, and H is called the *transfer function* of the system. The transfer function is the Fourier transform of the impulse response h, and it describes the effects of the system in the frequency domain (f_X, f_Y), relating the input spectrum to the output spectrum.

A precise measurement of the transfer function of the FTS and coupling optics pro-

vides a precise measurement of FTS systematic effects that contribute to the detector bandpass calibration uncertainty. If the FTS systematic effects are well-characterized, we can both mitigate some of the systematic effects in the FTS system and remove these systematic effects during bandpass calibration. Current and past CMB experiments have not attained the sensitivity levels of next-generation experiments, so it has never been necessary to measure the transfer function of the FTS used in calibration. For experiments like SO and CMB-S4, fully characterizing the FTS transfer function to high precision will be critical to achieving our science goals. We can measure the FTS transfer function once in lab, and then use it to calibrate detector arrays in the field without needing to re-calibrate between measurements, since the FTS system will stay the same and the transfer function will not change between measurements.

In the frequency domain, the signal measured by our detector (receiver) from the FTS is

$$F_{\text{out}} = S \times FTS \times R, \tag{5.5}$$

where FTS represents the transfer function of the FTS, R represents the transfer function of the receiver, and S is the source spectrum. The ultimate goal is to measure the response of the receiver, R (the detector bandpass).

With two FTS systems (A and B), we can measure the quantities ($S \times FTS_A \times R$), ($S \times FTS_B \times R$), and ($S \times FTS_A \times FTS_B \times R$) if we put FTS A and FTS B in series. Then, R can be found by calculating

$$R = \frac{(S \times FTS_A \times R) \cdot (S \times FTS_B \times R)}{(S \times FTS_A \times FTS_B \times R)}, \tag{5.6}$$

as shown in Figure 5.1. With this information and information about our source, we can then calculate the exact transfer function of each FTS:

$$FTS_{\text{meas}} = \frac{F_{\text{out}}}{S \cdot R}, \tag{5.7}$$

where F_{out} is again the signal measured by the detector (Equation 5.5). Knowing the transfer functions of each of the FTS systems, we can then directly measure any bandpass R' using one FTS in the future:

$$R' = \frac{(S \times FTS_{\text{meas}} \times R')}{S \cdot FTS_{\text{meas}}} \tag{5.8}$$

where FTS_{meas} is the measured FTS transfer function from Equation 5.7

Using the AdvACT and SO FTS and an identically designed system at Cornell, I took several sets of single and double FTS measurements. To take double FTS measurements, we joined both FTS systems in series. We then stepped the Michigan FTS system's dihedral mirror, and at each step did a full sweep of the Cornell FTS system's dihedral mirror—thereby creating a 2D interferogram.

The experimental setups are shown in Figures 5.2 and 5.3. We used a mercury arc lamp source and measured the output of each FTS using a detector in a small cryostat. We set up the FTS systems for measurements by aligning our source, FTS transfer mirrors, optical components, and receiver to maximize the measured signal. We used a small chopper wheel to modulate our input signal, and a lock-in amplifier to recover our output signal.

I analyzed the acquired data from the single-FTS measurements using the techniques described in Chapter IV: subtracting a baseline polynomial, apodizing the interferogram, Fourier transforming, and correcting for phase. The results are shown in Figures 5.4, 5.5, and 5.6.

These single-FTS measurements revealed that the Michigan FTS had a bend in the dihedral mirror, which caused its measured interferograms to be almost unrecognizable when compared to those measured using the properly aligned Cornell FTS, both shown in Figure 5.4. Because the Michigan FTS measurements were much noisier and not producing clean interferograms like the Cornell FTS, we tested all of Michigan's

103
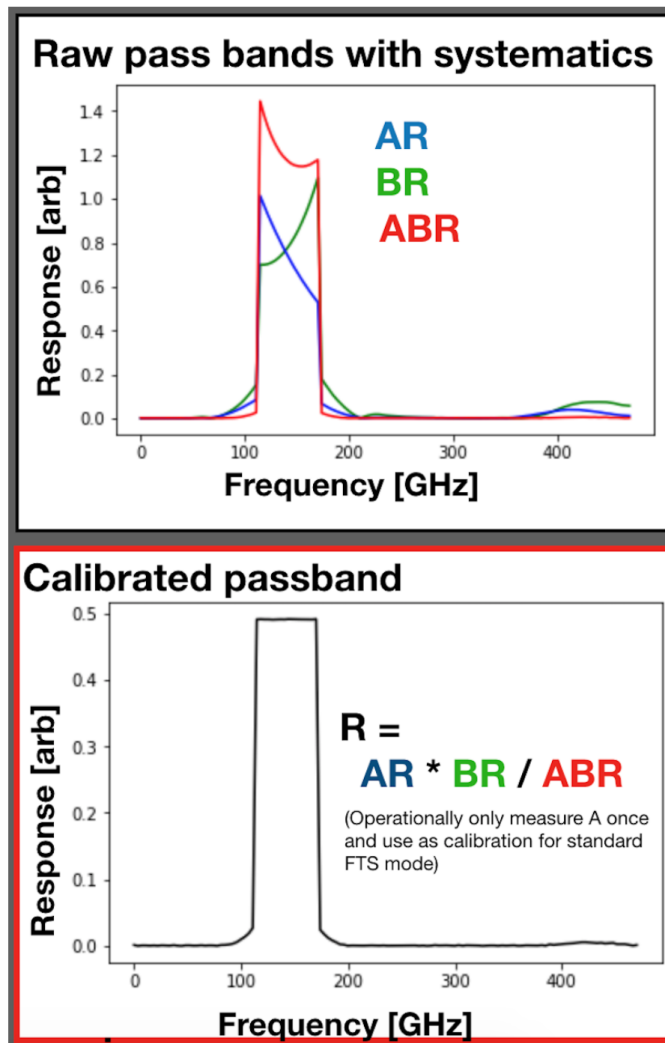
Figure 5.1: Simplified simulations of the double FTS method. A top hat band was used as the receiver response R, and the FTS transfer functions A and B were chosen such that harmonics would appear at the tail of the function *(top)*. We can recover the original top hat detector bandpass almost perfectly using this technique *(bottom)*. Image courtesy of Jeff McMahon.

(a) A view of the single FTS measurement setup, showing the brass cryostat that houses the detector and its window entrance at the bottom of the chamber. The mercury arc lamp can be seen on the left, illuminating a transfer mirror attached to the FTS. Another transfer mirror is positioned just at the end of the beam path to direct the signal into the cryostat.
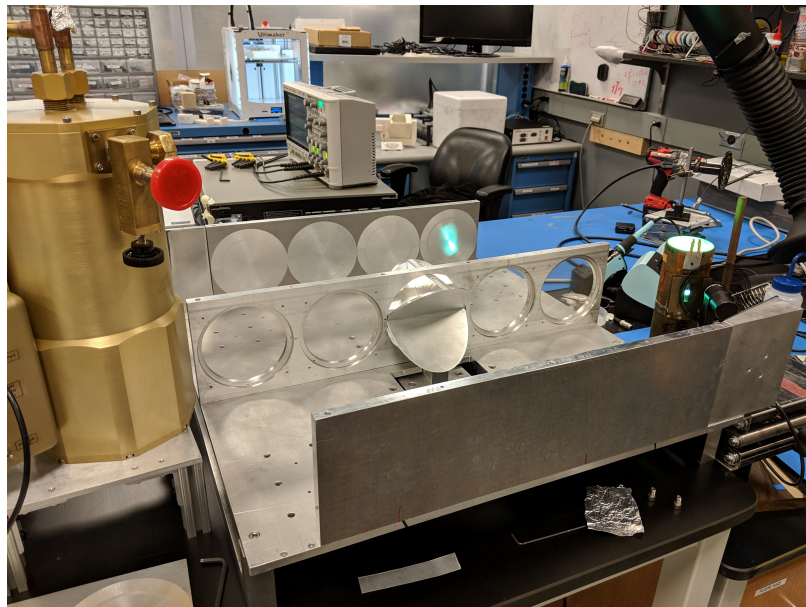
(b) Another view of the setup, showing the mercury beam on the first elliptical FTS mirror on the right of the instrument. We can also see a view of the FTS's dihedral mirror.

Figure 5.2: Setup for the single FTS measurements at Cornell. The FTS shown in this setup is Cornell's.
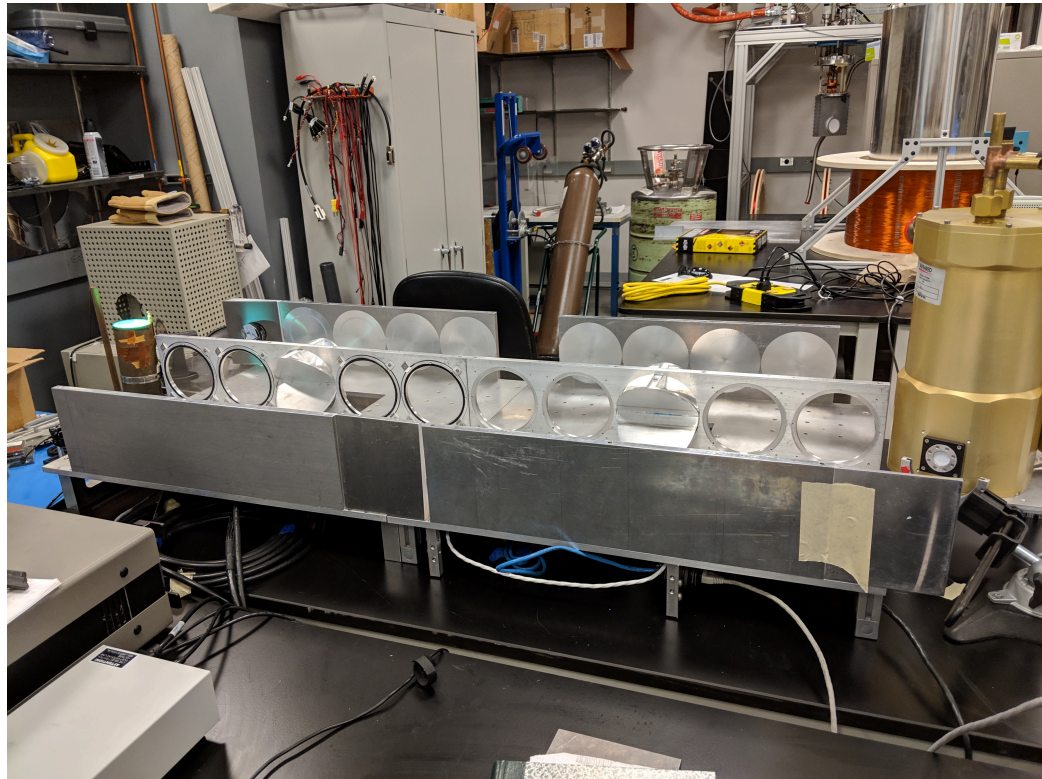
Figure 5.3: Setup for the dual FTS measurements at Cornell. Two FTS systems are joined in series, with a transfer mirror in between to redirect the output of the first FTS into the entrance of the next. Another transfer mirror is used at the end of the beam path again, to direct the signal into the cryostat. The Michigan FTS did not have an attachment interface for a transfer mirror like Cornell's did, so tape was used to position this transfer mirror. The flexibility of the tape allowed us to investigate the effects of minor positional deviations.
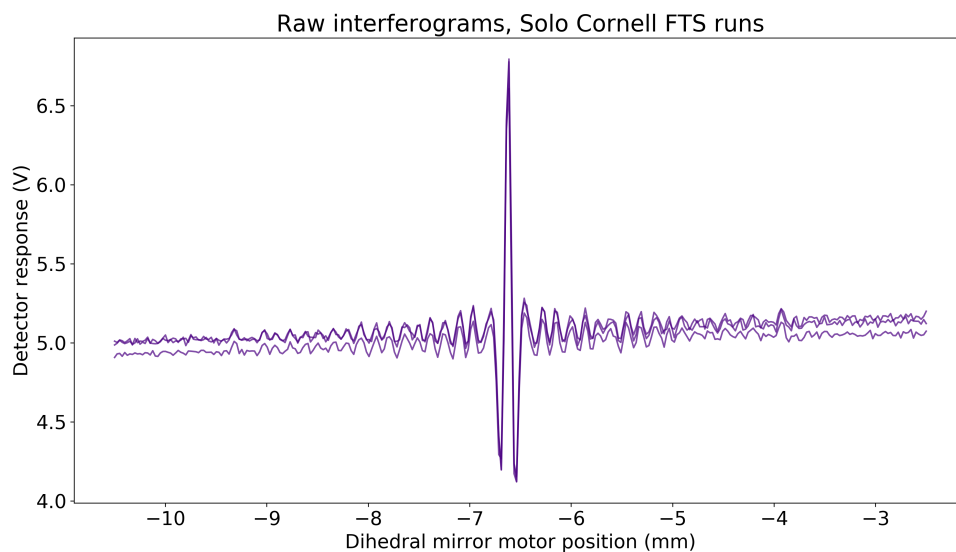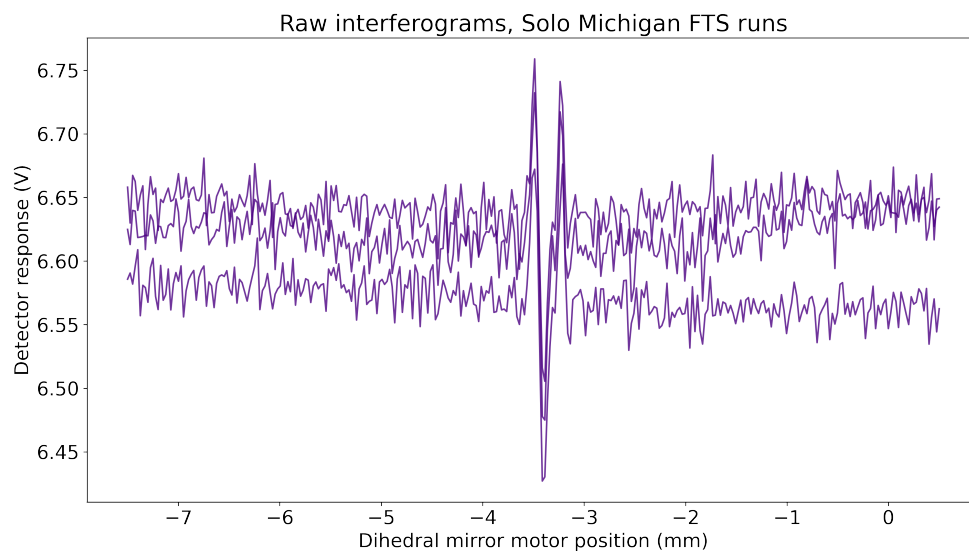
Figure 5.4: Raw interferograms taken with Michigan's FTS *(top)* and Cornell's FTS *(bottom)*. Three interferograms were taken using each machine, processed, and averaged before Fourier transformation. We can see that the Cornell FTS produced much cleaner and more consistent interferograms.
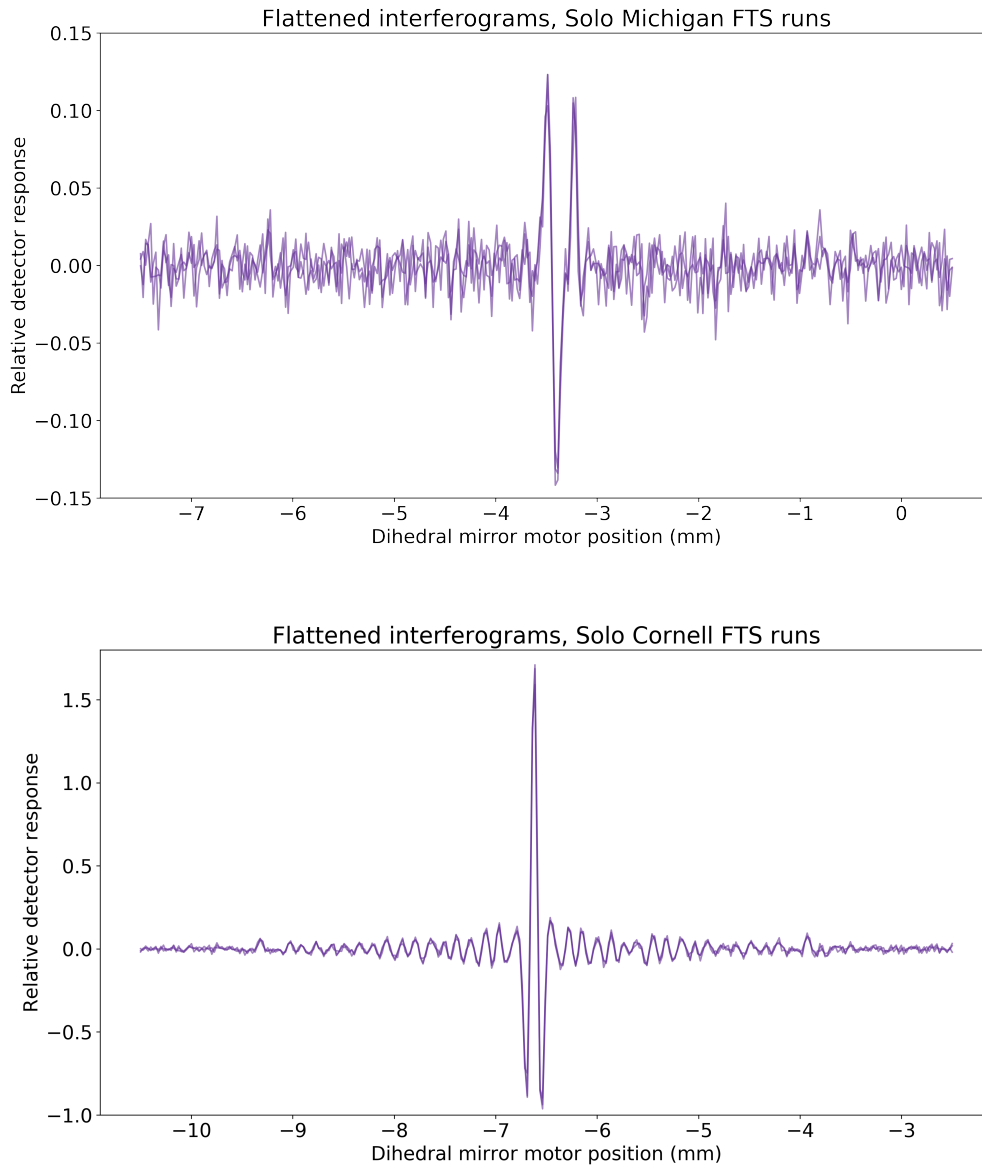
Figure 5.5: Flattened interferograms from Michigan's FTS *(top)* and Cornell's FTS *(bottom).* In this comparison, we can see how much noisier and more inconsistent the Michigan machine's data was. The Cornell interferograms align almost perfectly after basic correction.
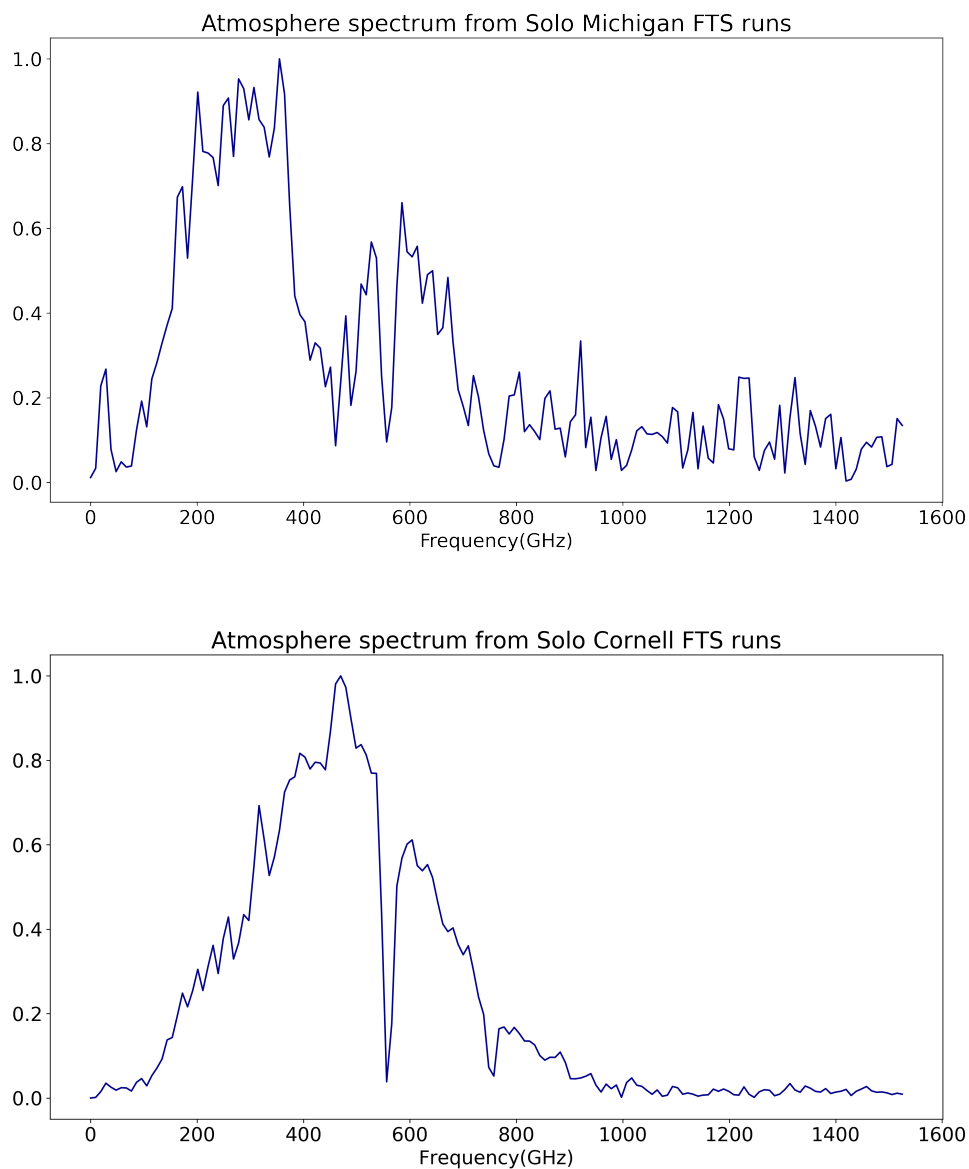
Figure 5.6: FFT of the average interferogram obtained using the Michigan FTS *(top)* and Cornell FTS *(bottom)*. These plots show the detector's spectral response to the FTS beam, which passes through the atmosphere. We see atmosphere absorption lines around 580 GHz and 780 GHz as expected. We can also see that Michigan's output was much lower quality than Cornell's.

optical components. Starting with Cornell's optical components in an FTS base, we swapped out components one by one until we discovered that Michigan's dihedral mirror was the source of the errors. We also discovered that the transfer mirror used to couple the source to the FTS was stretching one component of the beam's polarization, meaning that there was not a 50/50 beam split after the first polarizing wire grid. Even so, the spectra obtained from Cornell's FTS shown in Figure 5.6 could be used to investigate the effects of slightly tilting mirrors, changing the centering of polarizing wire grids, and making other small changes to the system—all of which significantly affected the FTS output beam's positioning and intensity. We found that slight mirror tilts on order $0.5°$ caused enough offset to greatly reduce the power received by the detector. It is therefore very important to construct FTS systems using pins to meet more stringent positioning tolerances in the design in order to improve the throughput of the signal.

Results from the double FTS measurements are shown in Figures 5.7 and 5.8. Because I collected a full interferogram from sweeping the Cornell FTS at every step of the Michigan FTS, I obtained a 2D interferogram from the measurements (Figure 5.7). With this method, we therefore cannot use the same analysis techniques that we use to process single-FTS interferograms. Instead of subtracting polynomials from individual interferograms, I did a plane subtraction on the 2D data. Figure 5.7 shows that fitting and subtracting a plane evens the data out and has a similar effect as a polynomial subtraction on a 1D interferogram.

I defined a 2D apodization window as the outer product of the $(1 - x^4)^2$ function with itself and applied this to the 2D data. I then performed a 2D DFT:

$$G(k_1, k_2) = \sum_{m=0}^{M-1} \sum_{n=0}^{N-1} g(m,n) \cdot \exp\left[-i(k_1 m/M + k_2 n/N)\right], \qquad (5.9)$$

where $G(k_1, k_2)$ is the Fourier transform of the 2D interferogram $g(m, n)$, k_1 and k_2

are spatial frequencies, and m and n are the dihedral mirror step indices for the Cornell FTS and Michigan FTS, respectively (with $m = 0$ and $n = 0$ corresponding to the start of a full sweep). The 2D FFT of the 2D interferograms is shown in Figure 5.8. We expect the 2D FFT to be approximately symmetric about the k_1 and k_2 axes (translated to frequencies ν_1 and ν_2 in the Figure)—the 1D FFTs of 1D interferograms are roughly symmetric, and we take the positive frequency data for bandpass calibration. Looking at positive frequency data in Figure 5.8, we can see the response of the Cornell FTS along the ν_1 axis, the response of the Michigan FTS along the ν_2 axis, and the response of the joint system along the $\nu_1 = \nu_2$ line. The individual FTS responses are shown in comparison to the single-FTS measurements in Figure 5.9. Data was taken up to a frequency of ~ 450 GHz, which encapsulates the full frequency range for ground-based CMB experiments.

While the bend in the Michigan FTS system's dihedral mirror contaminated the data in the double FTS measurements, I was able to find and correct physical errors in our FTS system (e.g. the dihedral mirror) and demonstrate that this is a viable technique for measuring an FTS transfer function. Improved measurements show a promising path forward for both identifying and correcting errors in the optical system of an FTS and for removing the systematic errors from the FTS system from bandpass calibrations. This technique will be critical for reaching the precise calibration levels needed for next-generation experiments.

5.2 Coupling Optics

For previous AdvACT FTS detector bandpass measurements, refractive coupling optics were used to couple the old FTS beam to the detectors (seen in Figure 4.2). To reduce the thermal load on the detectors, which can drive them out of their operational range, refractive designs are limited to few thin lenses.

The depth or sag z of an aspheric surface (to 4th-order), illustrated in Figure 5.10
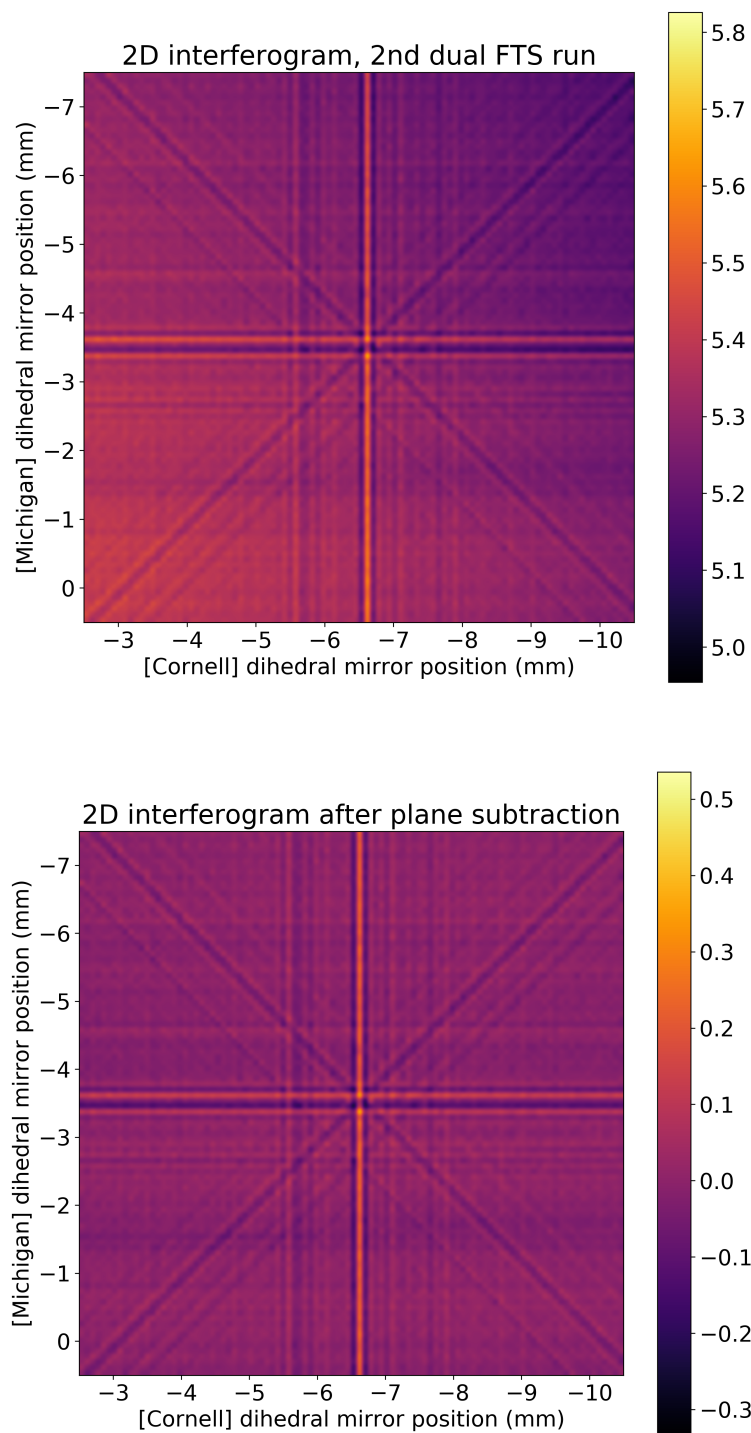
Figure 5.7: Raw 2D interferogram *(top)* and flattened 2D interferogram *(bottom)* from the first dual FTS run. For every mirror step of the Michigan FTS, a full mirror sweep was done on Cornell's FTS. A plane was fit to the 2D data and subtracted, flattening out the 2D interferograms. This subtraction removes the gradient seen in the top figure.
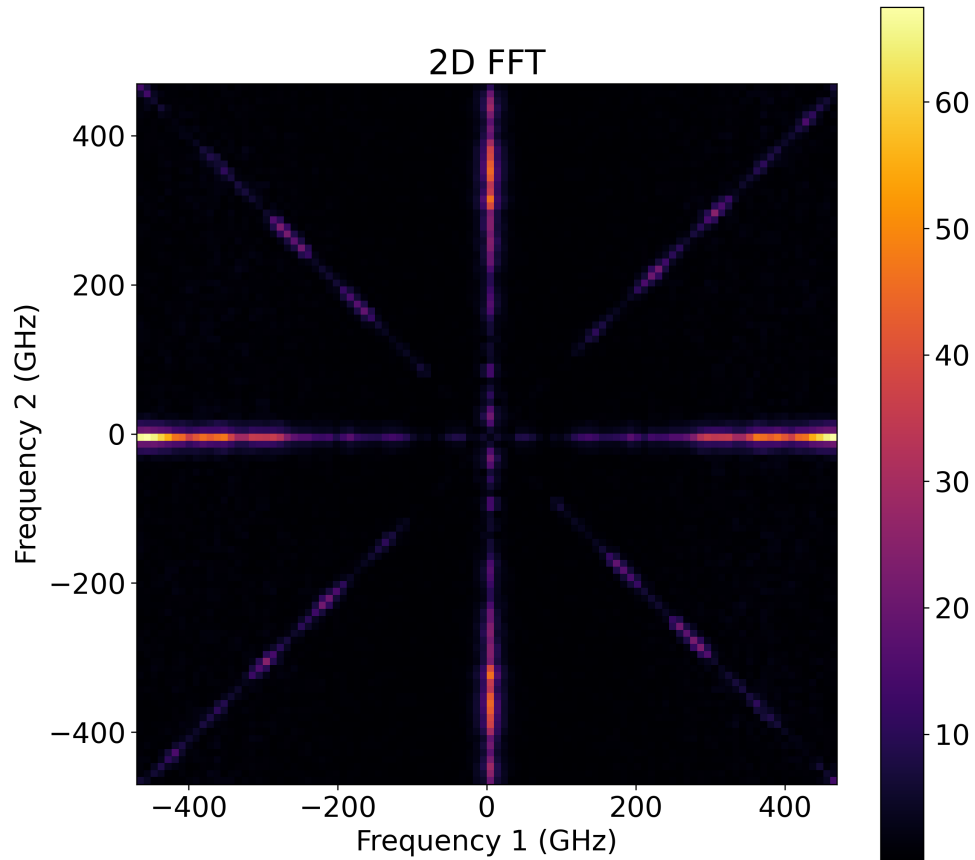
Figure 5.8: 2D FFT of our 2D interferogram data. We can see the response of Cornell's FTS along the ν_1 (frequency 1) axis, and the response of Michigan's FTS along the ν_2 (frequency 2) axis. These individual responses are shown in detail in Figure 5.9. The response of both FTS's in series is seen along the $\nu_1 = \nu_2$ line.
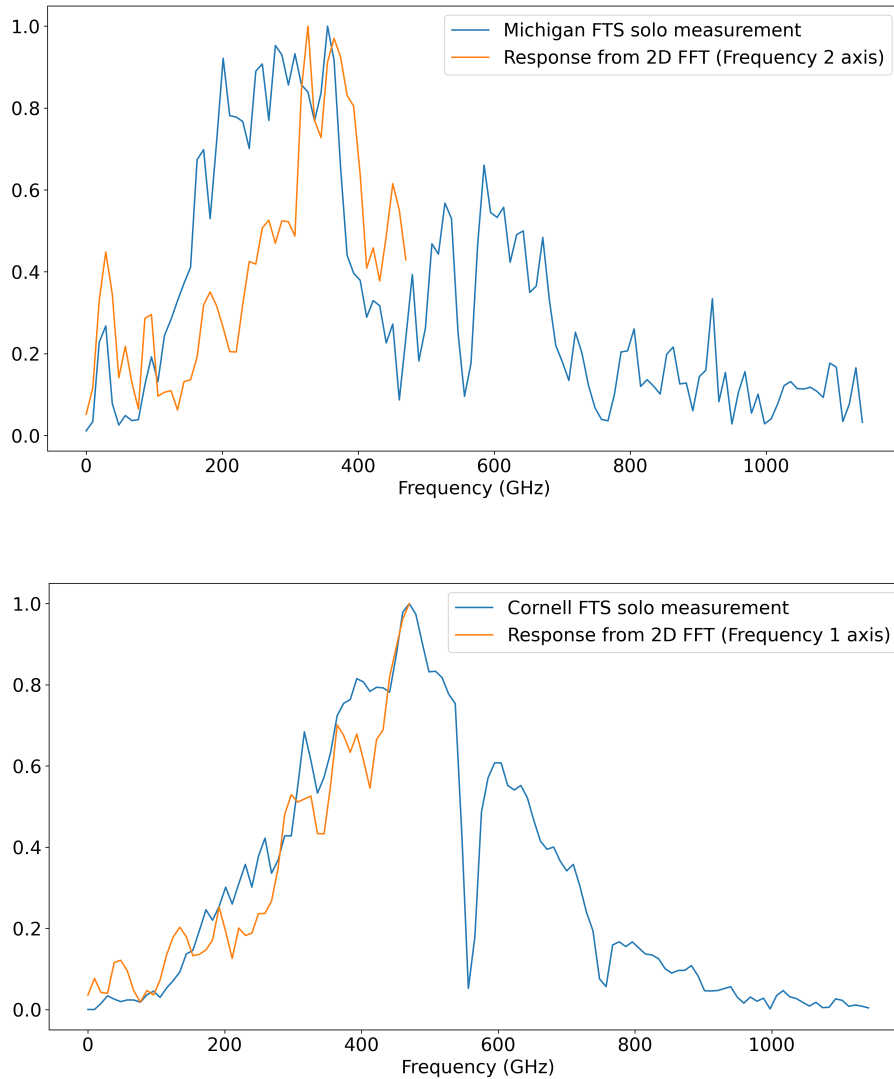
Figure 5.9: Spectra produced from the 2D FFT of our 2D interferogram. The Frequency 2 axis response from Figure 5.8 is shown compared to the spectrum produced from the Michigan single-FTS measurements *(top)*, and the Frequency 1 axis response is shown compared to the Cornell single-FTS spectrum *(bottom)*. We can see that the Cornell FTS spectra have similar characteristics (up to ~450 GHz where the 2D FFT measurements end), while the Michigan FTS spectra are much less aligned. Because the Michigan FTS had a dihedral mirror that was susceptible to deformation, this discrepancy could be due to small differences in the Michigan FTS optical path between measurements.
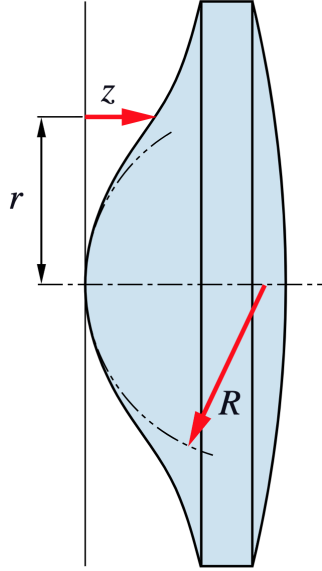
Figure 5.10: An aspheric surface defined by its depth or sag z, with the distance from the center r and radius of curvature R labeled [76].

is defined as

$$z = \frac{cr^2}{1 + \sqrt{1 - (1 + K)c^2 r^2}} + Ar^4, \tag{5.10}$$

where r is the distance from the center of the surface (aperture), c is the curvature (and $c = 1/R$ for radius of curvature R), K is the conic constant, and A is the 4th-order coefficient. (Note: a conic surface such as an ellipsoid can also be described by Equation 5.10, with $A = 0$. Conic constant $K > 0$ corresponds to oblate ellipses, $-1 < K < 0$ corresponds to prolate ellipses, $K = -1$ describes a parabola, and $K < -1$ describes hyperbolas.)

I designed new refractive coupling optics compatible with our new FTS, shown in Figure 5.11 with design parameters specified in Table 5.2. However, reflective coupling optics would reduce the thermal loading on the detectors, so for SO, I developed a reflective coupling optics design compatible with the SO LAT optics design (seen in Figure 5.12). My reflective coupling optics design is shown in Figure 5.13, and the design parameters are shown in Table 5.3. Several experimental constraints complicated the reflective coupling optics design. When coupling to the SO LATR (shown
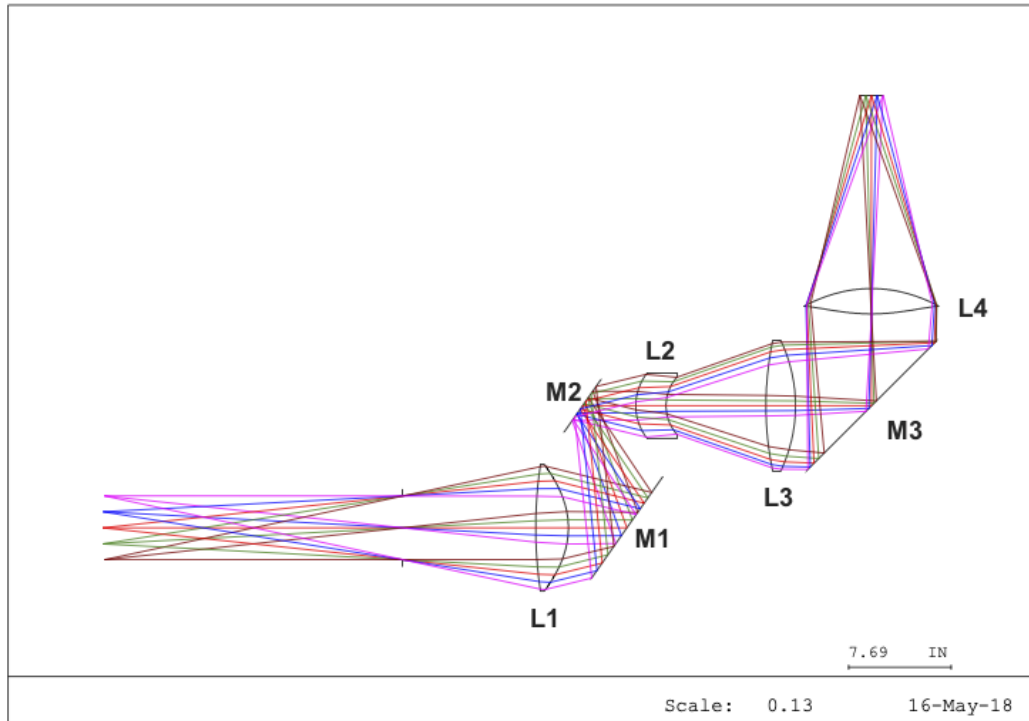
Figure 5.11: Ray diagram of the refractive FTS coupling optics design for AdvACT. The FTS beam enters the coupling optics system at the bottom left, and the beam is focused on the detector focal plane, on the top right. This design has a Strehl ratio of 0.99. While this design has great optical performance, I moved to reflective coupling optics to reduce any thermal loading on the cryogenic arrays. Mirror 3 (M3) is a partially reflective beam splitter, which reflects a small percentage towards the detector focal plane so as to not overload the TES bolometers.

Large Aperture Telescope - Simons Observ   Scale: 0.01
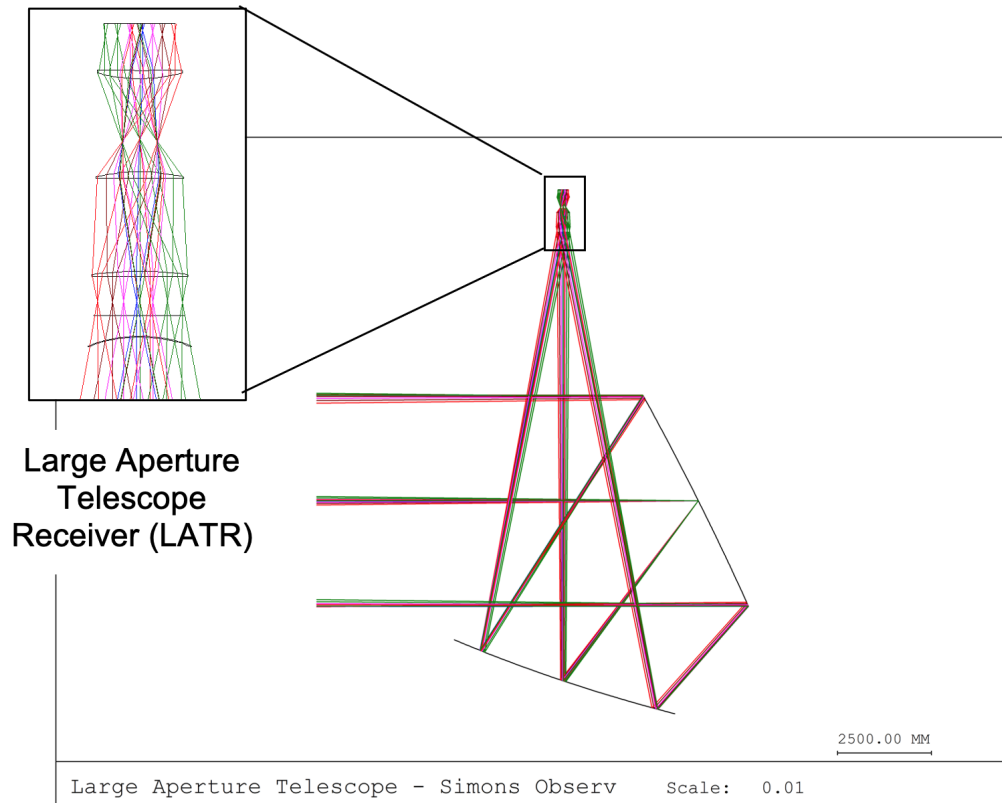
Figure 5.12: Code V optical design of the Simons Observatory Large Aperture Telescope (LAT). Light is focused onto detectors in the Large Aperture Telescope Receiver (LATR), shown in the zoom panel. The window to the cryogenic LATR is the curved surface appearing at the bottom of the zoom panel. The detector array is the flat surface at the top of the zoom panel, where the light comes to a focus.
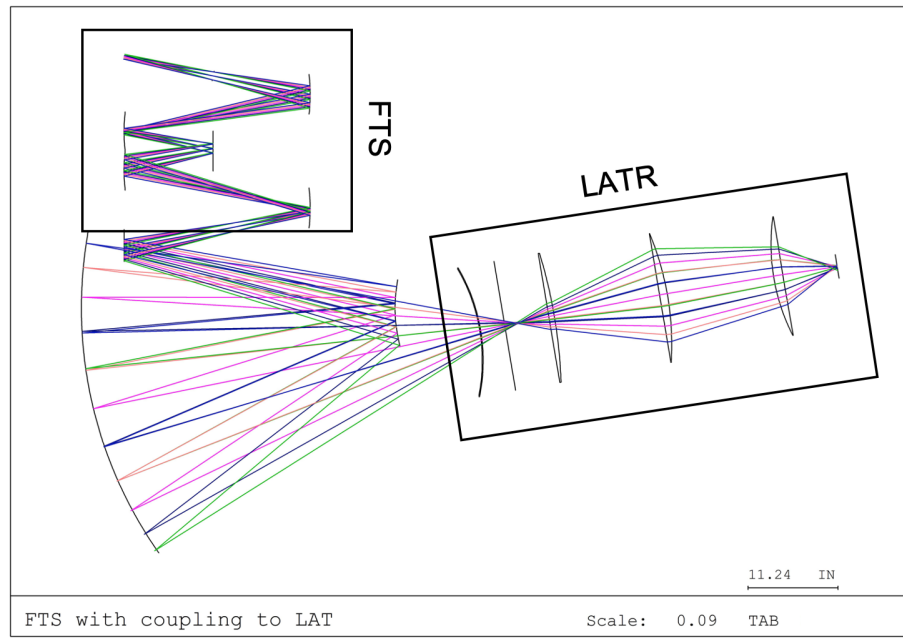
(a) A view looking at the top plate of the FTS.
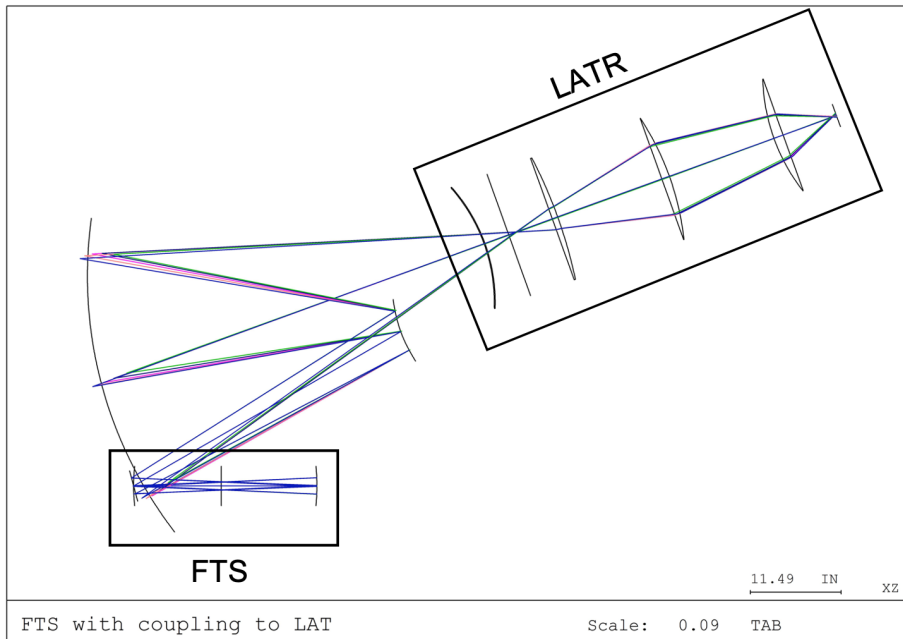
(b) A view looking at the FTS side-on.

Figure 5.13: Code V optical design cross-sections of the FTS coupled to the Simons Observatory Large Aperture Telescope Receiver (LATR) via my new reflective coupling optics. The coupling optics consist of 3 mirrors, and are shown between the FTS and LATR.

AdvACT Refractive Coupling Optics Design Parameters							
Component	Surface Type	Diam. (in.)	Radius of Curv. (in.)	K	α (°)	Material	Distance to Next Surface (in.)
FTS Mirror	Conic	4.8048	22.7470	0.0446	-12.194		22.5000
Stop	Flat	5.3000	∞				10.0000
L1 S1	Sphere	9.9454	32.1069			HDPE	2.4500
L1 S2	Sphere	9.9610	-6.0714				4.3921
M1	Flat	8.1773	∞		-25.000		9.7500
M2	Flat	3.3324	∞		25.000		4.0000
L2 S1	Sphere	5.3968	3.9685			HDPE	2.2725
L2 S2	Sphere	4.7446	3.2301				7.4949
L3 S1	Sphere	10.7537	23.7671			HDPE	2.2159
L3 S2	Sphere	10.7695	-10.0984				5.3000
M3	Flat	15.0817	∞		45.000		7.5000
L4 S1	Asphere	10.0272	-12.0113	-4.3584		HDPE	1.9000
L4 S2	Asphere	10.0157	11.6271	-0.2594			14.0000

Table 5.2: Design parameters for refractive coupling optics for coupling to the AdvACT receiver, shown in Figure 5.11. Here, K is the conic constant and α is the angular tilt from the x-axis (the rays travel along the z-axis). Lenses are denoted by 'L' (with each of their surfaces denoted by 'S') and mirrors are labeled 'M'.

SO LAT Reflective Coupling Optics Design Parameters								
Component	Surface Type	Diam. (in.)	Radius of Curv. (in.)	K	A	α (°)	β (°)	Distance to Next Surface (in.)
FTS Mirror	Conic	4.8048	22.7470	0.0446		-12.194	0.000	22.7470
M1	Flat	3.8250	∞			-12.194	-15.000	40.0000
M2	Asphere	8.0674	15.0000	1.0000	0.0004	14.000	10.000	40.0000
M3	Asphere	40.5848	51.4221	-0.9999		-3.037	-5.000	57.0661

Table 5.3: Design parameters for reflective coupling optics for coupling to the SO LATR, shown in Figure 5.13. Here, K is the conic constant, A is the 4th-order coefficient, α is the angular tilt from the x-axis, and β is the angular tilt from the y-axis (the rays travel along the z-axis). Mirrors are denoted by 'M'.

in Figure 5.12), we want the FTS beam to completely fill the detector feedhorns. To match the solid angle of the feedhorns, the coupling optics need to be $f/2.5$ or lower, putting a geometrical constraint on the size of the last mirror in the system. Since the detectors would be completely saturated by the full intensity of the FTS beam, the reflective coupling optics design must include a component that allows most of the beam to shine out to the sky. This is accomplished by a $\sim 45°$ flat "mirror" made of thin plastic—it will reflect a small percentage of the original beam (to stay in the system) and transmit most to the sky. The FTS and coupling optics must also fit in the tight space in front of the LATR. The design must also have good optical quality,

which is quantified by a high Strehl ratio $\mathcal{D}$—the ratio of the light intensity at the maximum of the point-spread function $H(f_X, f_Y)$ of the system with aberrations to that same maximum for the system in the absence of aberrations [77]:

$$\mathcal{D} = \frac{\int_{-\infty}^{\infty} \int_{-\infty}^{\infty} H(f_X, f_Y)_{\text{with}} \, df_X df_Y}{\int_{-\infty}^{\infty} \int_{-\infty}^{\infty} H(f_X, f_Y)_{\text{without}} \, df_X df_Y} \tag{5.11}$$

The coupling optics' focus will be sufficient if the system's Strehl ratio is above ~ 0.8. I developed a design that meets all of our requirements for detector calibration for the SO LAT, shown in Figure 5.13. The $\sim 45°$ flat mirror is located just opposite the exit of the FTS. Another mirror may be necessary to direct the stray light from the $\sim 45°$ flat out of the receiver. I achieved a Strehl ratio of 0.85, which was primarily driven by the low f-number required to fill the full solid angle of the detector feedhorns ($f/2.5$) and the tight fit in front of the LATR.

Another aspect of the coupling optics design is focused on improving the quality and number of detectors illuminated. Because of the poor coupling between the FTS and AdvACT detector arrays, as well as the small étendue of the FTS (100 mm²-Sr), we could only illuminate 4% of the focal plane in a single measurement. There is also not currently an FTS-array alignment system for ensuring normal incidence on the detector array. Because of this, we get an uneven illumination across the detectors, seen in Figures 4.12 and 4.13. This effect can be seen in individual bandpass measurements; the detectors are designed to have nearly top-hat bandpass profiles, but in our measurements we see slanted tops (see Figures 4.15 and 4.16), which don't appear during lab characterizations using the same FTS.

The improved reflective design illuminates a larger area of the focal plane more evenly, enabling more detectors to be measured at once as shown in Figure 5.13. In addition to redesigning the coupling optics, moving the FTS as little as possible during measurements and ensuring normal incidence will further reduce the uncertainty. This

could be achieved by implementing a set of stages to move and align the FTS between measurements, and based on this recommendation SO is developing linear stages for the FTS measurements. In addition to reducing the uncertainty in the measurements, it will also make measurements faster, which would enable taking measurements of more detectors across the focal plane. This is critically important for SO where we are moving from $\sim 5,000$ detectors (e.g. AdvACT) to over 60,000 and for CMB-S4, which will have over 500,000 detectors.

5.3   Wider Frequency Coverage

The FTS used for AdvACT measurements was sufficient to calibrate the HF and MF arrays to the desired level and achieve the experiment's science goals. However, this FTS is not optimized for LF array calibration, and the current measurement techniques will not yield a high enough precision for future experiments like SO and CMB-S4. It is therefore critical to design, build, and implement a new FTS that can achieve these next-level science goals.

The PIXIE-style FTS uses elliptical mirrors that are positioned at the foci of the mirrors on the opposite side, seen in Figures 5.14 and 5.15a. We can therefore scale the entire model up in size, changing the curvature of the elliptical mirrors to reflect the new mirror totem distances. The old and new FTS parameters are shown in Table 5.4 and illustrated in Figure 5.15. By scaling the FTS size up, we can achieve low-frequency resolution that will allow us to precisely calibrate the LF arrays without sacrificing high-frequency measurements. This makes the new model more compatible with the frequency band coverage for new CMB experiments. Additionally, scaling up will give the new FTS a larger étendue, allowing us to measure more detectors at once.

I built the new LF-compatible FTS. The new model will use a flat mirror in place of the dihedral mirror, as we found the dihedral mirror to be far too fragile and
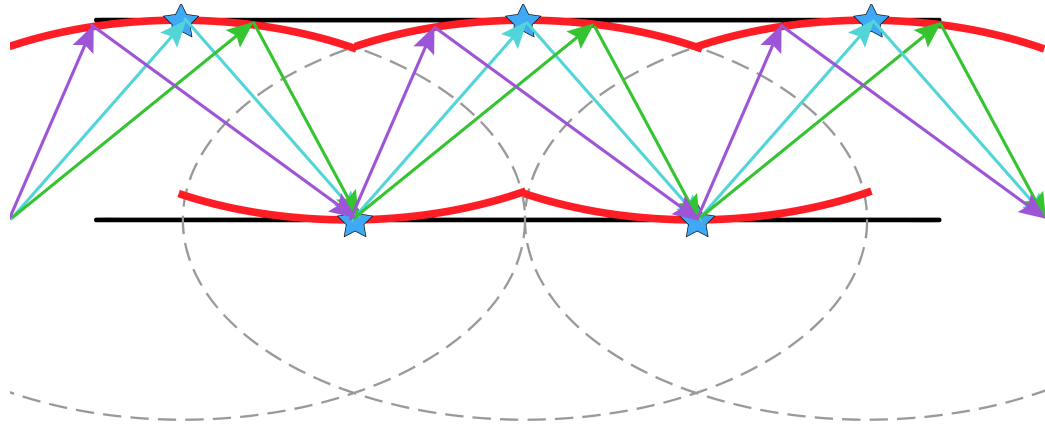
Figure 5.14: An exaggerated illustration of the FTS elliptical mirror geometry. The two black parallel lines represent the FTS mirror totems, with the red curves representing the elliptical mirrors. The full elliptical geometry is shown by the gray dashed lines. The PIXIE-style FTS is designed such that the center of each mirror lies at one of the foci (represented by the blue stars) of the opposite mirror. A basic ray trace shows how light from a point source propagates through the system using the elliptical mirror geometry.

prone to bends at the center. It has mirror totems machined by the University of Michigan machine shop. The wire grid polarizers were assembled by the Keating Lab at UCSD using 25 μm-diameter Tungsten wire with a pitch of 100 μm. Mirrors were polished to an optical finish to allow optical tests. This FTS will enable high precision measurements of the bandpasses across the frequency bands for SO and future CMB experiments.
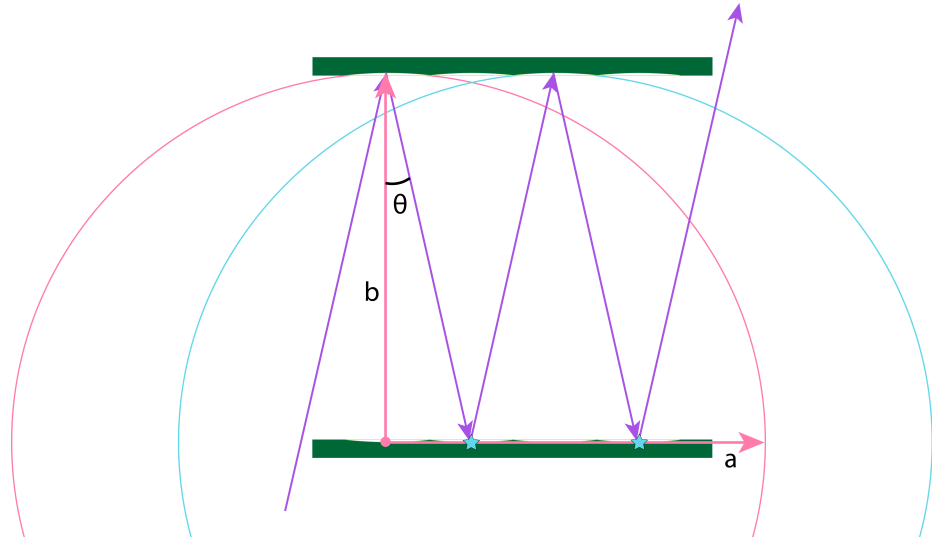
(a) Basic illustration of the PIXIE-style FTS used for AdvACT and SO calibration measurements and the elliptical mirror geometry. Purple lines represent rays propagating through the FTS. The semi-major and semi-minor axes (a and b, respectively) of the pink ellipse are labeled by the pink arrows, and the foci of the teal ellipse are labeled with teal stars at the bottom mirror totem. The angle θ between the mirrors is also shown.
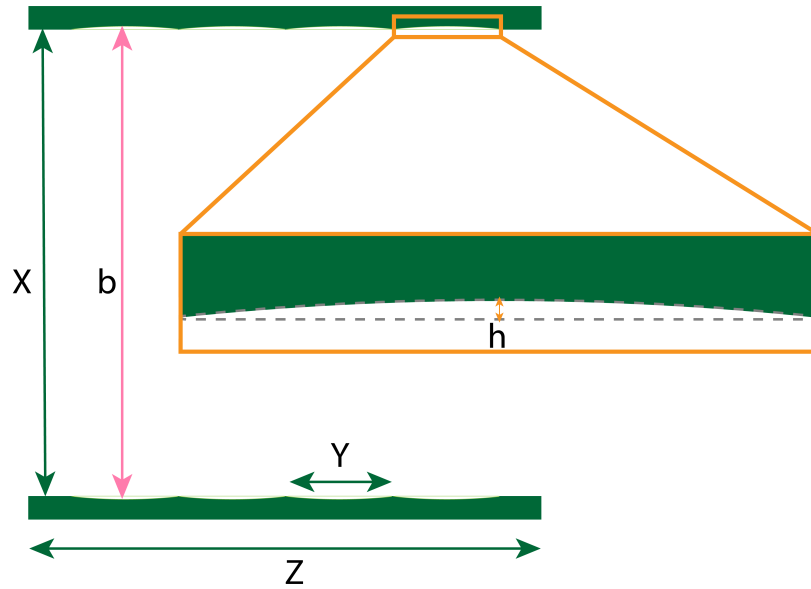
(b) Illustration of the FTS body (the parallel mirror totems) with a zoomed-in panel of the elliptical mirror depth. The semi-minor axis b is the distance between two opposite mirror centers, while the measurement X is the distance between the mirror *totems* (i.e., doesn't include the mirror sag). The mirror sag h is shown in the enlarged panel. The mirror diameter Y and FTS body length Z are also labeled along the bottom mirror totem.

Figure 5.15: Simplified illustrations of FTS design parameters.

FTS Design Parameters				
Parameter	Description		ACTPol FTS	SO FTS
Y	Mirror diameter (mm)		65.63	122.04
X	Distance between mirrors (mm)		330.59	558.43
Z	FTS length (mm)		328.19	610.21
θ	Angle between mirrors (°)		11.13	12.19
h	Mirror sag (mm)		1.56	3.16
a	Semi-major axis (mm)		340.1	577.8
b	Semi-minor axis (mm)		333.7	564.7
E	Étendue (mm^2 Sr)		100.00	420.00

Table 5.4: Comparison of design parameters for the original ACTPol MF/HF FTS and the new LF-compatible FTS. By scaling the original ACTPol model up by a factor of ~ 2, we are able to achieve ~ 4 times the optical throughput. Here the mirror sag (z in Equation 5.10) is labeled h. Parameters are illustrated in Figure 5.15.

CHAPTER VI

Conclusions

AdvACT is in its 5th year of observations, and its first results papers have been released (see [78], [79], and [80]). This exciting new data has allowed us to create high-resolution large area maps of the microwave sky in conjunction with Planck data [81], quantify the tSZ and kSZ effect [82] [83], create lensing mass maps [84], place constraints on cosmic birefringence [85], and perform cross-correlations with other data sets such as Dark Energy Survey (DES) [86], Sloan Digital Sky Survey (SDSS) [87] and WISE [88] to extract a wealth of information from the CMB.

Future experiments such as SO (fielding 2022) and CMB-S4 (fielding late 2020s) will have unprecedented sensitivity, which will enable us to:

1. Search for signals of inflation. Constraining or measuring r will directly measure the energy scale of inflation and allow us to narrow down the list of viable inflationary models or point to alternative models of the early Universe.

2. Test ΛCDM cosmology. Not only will upcoming experiments make precision measurements of ΛCDM parameters, they will also test the assumption that $w = -1$ for the dark energy equation of state, i.e. the "cosmological constant." We will also be able to search for parameters beyond ΛCDM such as r and ΔN_{eff}.

3. Search for particles beyond the Standard Model (BSM). Cosmological measurements of the number of relativistic species could reveal BSM physics like axions or sterile neutrinos [89].

4. Measure the sum of the neutrino masses. Measurements of the total sum of the mass are critical to our furthering our understanding of the elusive particles. The sum of the masses can help differentiate between the inverted and normal neutrino mass hierarchies, and it is highly complementary to neutrino oscillation experiments' mass difference measurements.

5. Uncover the nature of dark matter and dark energy. Large scale structure formed relatively recently, in the matter-dominated and dark energy-dominated eras, making it highly sensitive to the effects of dark matter and dark energy. Large scale structure measurements with the CMB can be combined with other large scale structure surveys at different wavelengths such as optical surveys (DES) to further understand these mysterious dark sectors.

To achieve the necessary sensitivity to make these science pursuits possible, these future experiments must have more detectors and wider frequency coverage. SO will have $\sim 60,000$ detectors, and CMB-S4 will have over $500,000$ detectors, improving the sensitivity by over an order of magnitude compared to current experiments. However, as sensitivity increases, so too does susceptibility to systematic effects. SO and CMB-S4 will add more frequency bands to characterize and remove polarized foreground contamination from the CMB signal and better identify SZ sources. The major systematic effect in this work is uncertainty in the calibration of detector bandpasses. To be able to (1) remove foregrounds to the high precision necessary to measure r and (2) identify galaxy clusters, we must meet extremely stringent requirements on the bandpass calibration.

I analyzed bandpass measurements taken on AdvACT and determined that the

current calibration uncertainty is a few percent. This is consistent with other current-generation experiments and is sufficient for their science goals. With its increased sensitivity, this level becomes very marginal on SO for r and not sufficient for source identification. For CMB-S4 the requirements will be even more stringent. Future experiments like SO, CMB-S4, and beyond will require new methods to reduce this uncertainty.

I identified and investigated several methods to improve bandpass measurements for these future experiments. Using a wider frequency coverage than past experiments will allow us to characterize and remove polarized foregrounds with exceedingly high accuracy, and SO and CMB-S4 plan to do this by adding more LF and UHF bands. I built a new FTS with a wider frequency coverage that can be used for detector calibration measurements across all bands for SO. To further reduce calibration uncertainty, I developed a method to characterize the FTS transfer function. The initial results are promising for identifying and mitigating systematic effects in bandpass calibration measurements. I also designed a new set of reflective coupling optics to accommodate the wider étendue of the new FTS and reduce thermal loading on the detectors. These optics will require larger components than previous refractive designs, but they will allow us to characterize more detectors on an array at once, and they are the most promising avenue for making precise measurements.

These improvements will be critical in achieving the very stringent bandpass requirements of future experiments. The bandpass calibration requirements are a critical calibration needed for CMB experiments. Other calibration requirements include beam, pointing, gain, and polarization angle calibrations, which will also need improvement at similar levels to the bandpass requirement. With improved calibration measurements, we can enable CMB measurements that will cross critical thresholds for discovering new physics and understanding the fundamental physics of our Universe.

BIBLIOGRAPHY

BIBLIOGRAPHY

[1] Barb Mattson. 100 years of general relativity. https://asd.gsfc.nasa.gov/blueshift/index.php/2015/11/25/100-years-of-general-relativity/, November 2015.

[2] Edwin Hubble. A Relation between Distance and Radial Velocity among Extra-Galactic Nebulae. *Proceedings of the National Academy of Science*, 15(3):168–173, March 1929.

[3] Planck Collaboration, N. Aghanim, Y. Akrami, M. Ashdown, J. Aumont, C. Baccigalupi, M. Ballardini, A. J. Banday, R. B. Barreiro, N. Bartolo, S. Basak, R. Battye, K. Benabed, J.-P. Bernard, M. Bersanelli, P. Bielewicz, J. J. Bock, J. R. Bond, J. Borrill, F. R. Bouchet, F. Boulanger, M. Bucher, C. Burigana, R. C. Butler, E. Calabrese, J.-F. Cardoso, J. Carron, A. Challinor, H. C. Chiang, J. Chluba, L. P. L. Colombo, C. Combet, D. Contreras, B. P. Crill, F. Cuttaia, P. de Bernardis, G. de Zotti, Delabrouille, J., Delouis, J.-M., Di Valentino, E., J. M. Diego, O. Doré, M. Douspis, A. Ducout, X. Dupac, S. Dusini, G. Efstathiou, F. Elsner, T. A. Enßlin, H. K. Eriksen, Y. Fantaye, M. Farhang, J. Fergusson, R. Fernandez-Cobos, F. Finelli, F. Forastieri, M. Frailis, A. A. Fraisse, E. Franceschi, A. Frolov, S. Galeotta, S. Galli, K. Ganga, R. T. Génova-Santos, M. Gerbino, T. Ghosh, J. González-Nuevo, K. M. Górski, S. Gratton, A. Gruppuso, J. E. Gudmundsson, J. Hamann, W. Handley, F. K. Hansen, D. Herranz, S. R. Hildebrandt, E. Hivon, Z. Huang, A. H. Jaffe, W. C. Jones, A. Karakci, E. Keihänen, R. Keskitalo, K. Kiiveri, J. Kim, T. S. Kisner, L. Knox, N. Krachmalnicoff, M. Kunz, H. Kurki-Suonio, G. Lagache, J.-M. Lamarre, A. Lasenby, M. Lattanzi, C. R. Lawrence, M. Le Jeune, P. Lemos, J. Lesgourgues, F. Levrier, A. Lewis, M. Liguori, P. B. Lilje, M. Lilley, V. Lindholm, M. López-Caniego, P. M. Lubin, Y.-Z. Ma, J. F. Macías-Pérez, G. Maggio, D. Maino, N. Mandolesi, A. Mangilli, A. Marcos-Caballero, M. Maris, P. G. Martin, M. Martinelli, E. Martínez-González, S. Matarrese, N. Mauri, J. D. McEwen, P. R. Meinhold, A. Melchiorri, A. Mennella, M. Migliaccio, M. Millea, S. Mitra, M.-A. Miville-Deschênes, D. Molinari, L. Montier, G. Morgante, A. Moss, P. Natoli, H. U. Nørgaard-Nielsen, L. Pagano, D. Paoletti, B. Partridge, G. Patanchon, H. V. Peiris, F. Perrotta, V. Pettorino, F. Piacentini, L. Polastri, G. Polenta, J.-L. Puget, J. P. Rachen, M. Reinecke, M. Remazeilles, A. Renzi, G. Rocha, C. Rosset, G. Roudier, J. A. Rubiño-Martín, B. Ruiz-Granados, L. Salvati, M. Sandri, M. Savelainen, D. Scott, E. P. S. Shellard, C. Sirignano, G. Sirri, L. D. Spencer, R. Sunyaev, Suur-Uski, A.-S., Tauber, J. A., Tavagnacco, D., M. Tenti, L. Toffo-

latti, M. Tomasi, T. Trombetti, L. Valenziano, J. Valiviita, B. Van Tent, L. Vibert, P. Vielva, F. Villa, N. Vittorio, B. D. Wandelt, I. K. Wehus, M. White, S. D. M. White, A. Zacchei, and A. Zonca. Planck 2018 results - vi. cosmological parameters. *A&A*, 641:A6, 2020.

[4] R. A. Alpher, H. Bethe, and G. Gamow. The Origin of Chemical Elements. *Physical Review*, 73(7):803–804, April 1948.

[5] Robert V. Wagoner, William A. Fowler, and F. Hoyle. On the Synthesis of Elements at Very High Temperatures. *ApJ*, 148:3, April 1967.

[6] A. A. Penzias and R. W. Wilson. A Measurement of Excess Antenna Temperature at 4080 Mc/s. *ApJ*, 142:419–421, July 1965.

[7] R. H. Dicke, P. J. E. Peebles, P. G. Roll, and D. T. Wilkinson. Cosmic Black-Body Radiation. *ApJ*, 142:414–419, July 1965.

[8] J. C. Mather, E. S. Cheng, D. A. Cottingham, Jr. Eplee, R. E., D. J. Fixsen, T. Hewagama, R. B. Isaacman, K. A. Jensen, S. S. Meyer, P. D. Noerdlinger, S. M. Read, L. P. Rosen, R. A. Shafer, E. L. Wright, C. L. Bennett, N. W. Boggess, M. G. Hauser, T. Kelsall, Jr. Moseley, S. H., R. F. Silverberg, G. F. Smoot, R. Weiss, and D. T. Wilkinson. Measurement of the Cosmic Microwave Background Spectrum by the COBE FIRAS Instrument. *ApJ*, 420:439, January 1994.

[9] Dorothea Samtleben, Suzanne Staggs, and Bruce Winstein. The Cosmic Microwave Background for Pedestrians: A Review for Particle and Nuclear Physicists. *Annual Review of Nuclear and Particle Science*, 57(1):245–283, November 2007.

[10] F. Zwicky. Republication of: The redshift of extragalactic nebulae. *General Relativity and Gravitation*, 41(1):207–224, January 2009.

[11] V. C. Rubin. The Rotation of Spiral Galaxies. *Science*, 220(4604):1339–1344, June 1983.

[12] Branko Novakovic, Dubravko Majetic, Josip Kasac, Danko Brezak, and Vladimir Milic. Application of control terms p1 and p2 to estimation of rotation curve of stars. In *Journal of Trends in the Development of Machinery and Associated Technology*, volume 18, pages 219–222, September 2014.

[13] Brian Dunbar. Planck mission brings universe into sharp focus. https://www.nasa.gov/mission_pages/planck/news/planck20130321.html, June 2013.

[14] Barbara Ryden. *Introduction to cosmology*. Addison Wesley, 2003.

[15] G. Hinshaw, M. R. Nolta, C. L. Bennett, R. Bean, O. Doré, M. R. Greason, M. Halpern, R. S. Hill, N. Jarosik, A. Kogut, E. Komatsu, M. Limon, N. Odegard, S. S. Meyer, L. Page, H. V. Peiris, D. N. Spergel, G. S. Tucker,

L. Verde, J. L. Weiland, E. Wollack, and E. L. Wright. Three-Year Wilkinson Microwave Anisotropy Probe (WMAP) Observations: Temperature Analysis. *ApJS*, 170(2):288–334, June 2007.

[16] Ofer Lahav and Andrew R. Liddle. The Cosmological Parameters 2014. *arXiv e-prints*, page arXiv:1401.1389, January 2014.

[17] Alan H. Guth. Inflationary universe: A possible solution to the horizon and flatness problems. *Phys. Rev. D*, 23(2):347–356, January 1981.

[18] Ethan Siegel. Distances, position, and motion in the universe. https://scienceblogs.com/startswithabang/2009/08/03/distances-position-and-motion, 2009.

[19] Andrew R. Liddle and D. H. Lyth. *Cosmological inflation and large-scale structure.* Cambridge University Press, 2009.

[20] Uroš Seljak and Matias Zaldarriaga. Signature of Gravity Waves in the Polarization of the Microwave Background. *Phys. Rev. Lett.*, 78(11):2054–2057, March 1997.

[21] Marc Kamionkowski. Possible Relics from New Physics in the Early Universe: Inflation, the Cosmic Microwave Background, and Particle Dark Matter. *arXiv e-prints*, pages astro–ph/9809214, September 1998.

[22] Matias Zaldarriaga and Uroš Seljak. Gravitational lensing effect on cosmic microwave background polarization. *Phys. Rev. D*, 58(2):023003, July 1998.

[23] Daniel Baumann, Mark G. Jackson, Peter Adshead, Alexandre Amblard, Amjad Ashoorioon, Nicola Bartolo, Rachel Bean, Maria Beltràn, Francesco de Bernardis, Simeon Bird, Xingang Chen, Daniel J. H. Chung, Loris Colombo, Asantha Cooray, Paolo Creminelli, Scott Dodelson, Joanna Dunkley, Cora Dvorkin, Richard Easther, Fabio Finelli, Raphael Flauger, Mark P. Hertzberg, Katherine Jones-Smith, Shamit Kachru, Kenji Kadota, Justin Khoury, William H. Kinney, Eiichiro Komatsu, Lawrence M. Krauss, Julien Lesgourgues, Andrew Liddle, Michele Liguori, Eugene Lim, Andrei Linde, Sabino Matarrese, Harsh Mathur, Liam McAllister, Alessandro Melchiorri, Alberto Nicolis, Luca Pagano, Hiranya V. Peiris, Marco Peloso, Levon Pogosian, Elena Pierpaoli, Antonio Riotto, Uroš Seljak, Leonardo Senatore, Sarah Shandera, Eva Silverstein, Tristan Smith, Pascal Vaudrevange, Licia Verde, Ben Wandelt, David Wands, Scott Watson, Mark Wyman, Amit Yadav, Wessel Valkenburg, and Matias Zaldarriaga. Probing inflation with cmb polarization. *AIP Conference Proceedings*, 1141(1):10–120, 2009.

[24] Vihan Patel and Charley Lineweaver. Solutions to the cosmic initial entropy problem without equilibrium initial conditions. *Entropy*, 19:411, August 2017.

[25] Kevork N. Abazajian, Peter Adshead, Zeeshan Ahmed, Steven W. Allen, David Alonso, Kam S. Arnold, Carlo Baccigalupi, James G. Bartlett, Nicholas Battaglia, Bradford A. Benson, Colin A. Bischoff, Julian Borrill, Victor Buza, Erminia Calabrese, Robert Caldwell, John E. Carlstrom, Clarence L. Chang, Thomas M. Crawford, Francis-Yan Cyr-Racine, Francesco De Bernardis, Tijmen de Haan, Sperello di Serego Alighieri, Joanna Dunkley, Cora Dvorkin, Josquin Errard, Giulio Fabbian, Stephen Feeney, Simone Ferraro, Jeffrey P. Filippini, Raphael Flauger, George M. Fuller, Vera Gluscevic, Daniel Green, Daniel Grin, Evan Grohs, Jason W. Henning, J. Colin Hill, Renee Hlozek, Gilbert Holder, William Holzapfel, Wayne Hu, Kevin M. Huffenberger, Reijo Keskitalo, Lloyd Knox, Arthur Kosowsky, John Kovac, Ely D. Kovetz, Chao-Lin Kuo, Akito Kusaka, Maude Le Jeune, Adrian T. Lee, Marc Lilley, Marilena Loverde, Mathew S. Madhavacheril, Adam Mantz, David J. E. Marsh, Jeffrey McMahon, Pieter Daniel Meerburg, Joel Meyers, Amber D. Miller, Julian B. Munoz, Ho Nam Nguyen, Michael D. Niemack, Marco Peloso, Julien Peloton, Levon Pogosian, Clement Pryke, Marco Raveri, Christian L. Reichardt, Graca Rocha, Aditya Rotti, Emmanuel Schaan, Marcel M. Schmittfull, Douglas Scott, Neelima Sehgal, Sarah Shandera, Blake D. Sherwin, Tristan L. Smith, Lorenzo Sorbo, Glenn D. Starkman, Kyle T. Story, Alexander van Engelen, Joaquin D. Vieira, Scott Watson, Nathan Whitehorn, and W. L. Kimmy Wu. CMB-S4 Science Book, First Edition. *arXiv e-prints*, page arXiv:1610.02743, October 2016.

[26] Steve K. Choi, Matthew Hasselfield, Shuay-Pwu Patty Ho, Brian Koopman, Marius Lungu, Maximilian H. Abitbol, Graeme E. Addison, Peter A. R. Ade, Simone Aiola, David Alonso, Mandana Amiri, Stefania Amodeo, Elio Angile, Jason E. Austermann, Taylor Baildon, Nick Battaglia, James A. Beall, Rachel Bean, Daniel T. Becker, J. Richard Bond, Sarah Marie Bruno, Erminia Calabrese, Victoria Calafut, Luis E. Campusano, Felipe Carrero, Grace E. Chesmore, Hsiao-mei Cho, Susan E. Clark, Nicholas F. Cothard, Devin Crichton, Kevin T. Crowley, Omar Darwish, Rahul Datta, Edward V. Denison, Mark J. Devlin, Cody J. Duell, Shannon M. Duff, Adriaan J. Duivenvoorden, Jo Dunkley, Rolando Dünner, Thomas Essinger-Hileman, Max Fankhanel, Simone Ferraro, Anna E. Fox, Brittany Fuzia, Patricio A. Gallardo, Vera Gluscevic, Joseph E. Golec, Emily Grace, Megan Gralla, Yilun Guan, Kirsten Hall, Mark Halpern, Dongwon Han, Peter Hargrave, Shawn Henderson, Brandon Hensley, J. Colin Hill, Gene C. Hilton, Matt Hilton, Adam D. Hincks, Renée Hložek, Johannes Hubmayr, Kevin M. Huffenberger, John P. Hughes, Leopoldo Infante, Kent Irwin, Rebecca Jackson, Jeff Klein, Kenda Knowles, Arthur Kosowsky, Vincent Lakey, Dale Li, Yaqiong Li, Zack Li, Martine Lokken, Thibaut Louis, Amanda MacInnis, Mathew Madhavacheril, Felipe Maldonado, Maya Mallaby-Kay, Danica Marsden, Loïc Maurin, Jeff McMahon, Felipe Menanteau, Kavilan Moodley, Tim Morton, Sigurd Naess, Toshiya Namikawa, Federico Nati, Laura Newburgh, John P. Nibarger, Andrina Nicola, Michael D. Niemack, Michael R. Nolta, John Orlowski-Sherer, Lyman A. Page, Christine G. Pappas, Bruce Partridge, Phumlani Phakathi, Heather Prince, Roberto Puddu, Frank J. Qu, Jesus Rivera,

Naomi Robertson, Felipe Rojas, Maria Salatino, Emmanuel Schaan, Alessandro Schillaci, Benjamin L. Schmitt, Neelima Sehgal, Blake D. Sherwin, Carlos Sierra, Jon Sievers, Cristobal Sifon, Precious Sikhosana, Sara Simon, David N. Spergel, Suzanne T. Staggs, Jason Stevens, Emilie Storer, Dhaneshwar D. Sunder, Eric R. Switzer, Ben Thorne, Robert Thornton, Hy Trac, Jesse Treu, Carole Tucker, Leila R. Vale, Alexander Van Engelen, Jeff Van Lanen, Eve M. Vavagiakis, Kasey Wagoner, Yuhan Wang, Jonathan T. Ward, Edward J. Wollack, Zhilei Xu, Fernando Zago, and Ningfeng Zhu. The Atacama Cosmology Telescope: a measurement of the Cosmic Microwave Background power spectra at 98 and 150 GHz. *J. Cosmology Astropart. Phys.*, 2020(12):045, December 2020.

[27] Naoshi Sugiyama. Introduction to temperature anisotropies of Cosmic Microwave Background radiation. *Progress of Theoretical and Experimental Physics*, 2014(6):06B101, June 2014.

[28] Y. B. Zeldovich and R. A. Sunyaev. The Interaction of Matter and Radiation in a Hot-Model Universe. *Ap&SS*, 4(3):301–316, July 1969.

[29] R. A. Sunyaev and Y. B. Zeldovich. The Spectrum of Primordial Radiation, its Distortions and their Significance. *Comments on Astrophysics and Space Physics*, 2:66, March 1970.

[30] John E. Carlstrom, Gilbert P. Holder, and Erik D. Reese. Cosmology with the Sunyaev-Zel'dovich Effect. *ARA&A*, 40:643–680, January 2002.

[31] Alexander van Engelen, Blake D. Sherwin, Neelima Sehgal, Graeme E. Addison, Rupert Allison, Nick Battaglia, Francesco de Bernardis, J. Richard Bond, Erminia Calabrese, Kevin Coughlin, Devin Crichton, Rahul Datta, Mark J. Devlin, Joanna Dunkley, Rolando Dünner, Patricio Gallardo, Emily Grace, Megan Gralla, Amir Hajian, Matthew Hasselfield, Shawn Henderson, J. Colin Hill, Matt Hilton, Adam D. Hincks, Renée Hlozek, Kevin M. Huffenberger, John P. Hughes, Brian Koopman, Arthur Kosowsky, Thibaut Louis, Marius Lungu, Mathew Madhavacheril, Loïc Maurin, Jeff McMahon, Kavilan Moodley, Charles Munson, Sigurd Naess, Federico Nati, Laura Newburgh, Michael D. Niemack, Michael R. Nolta, Lyman A. Page, Christine Pappas, Bruce Partridge, Benjamin L. Schmitt, Jonathan L. Sievers, Sara Simon, David N. Spergel, Suzanne T. Staggs, Eric R. Switzer, Jonathan T. Ward, and Edward J. Wollack. The Atacama Cosmology Telescope: Lensing of CMB Temperature and Polarization Derived from Cosmic Infrared Background Cross-correlation. *ApJ*, 808(1):7, July 2015.

[32] P. A. R. Ade, Y. Akiba, A. E. Anthony, K. Arnold, M. Atlas, D. Barron, D. Boettger, J. Borrill, S. Chapman, Y. Chinone, M. Dobbs, T. Elleflot, J. Errard, G. Fabbian, C. Feng, D. Flanigan, A. Gilbert, W. Grainger, N. W. Halverson, M. Hasegawa, K. Hattori, M. Hazumi, W. L. Holzapfel, Y. Hori, J. Howard, P. Hyland, Y. Inoue, G. C. Jaehnig, A. Jaffe, B. Keating, Z. Kermish, R. Keskitalo, T. Kisner, M. Le Jeune, A. T. Lee, E. Linder, E. M. Leitch, M. Lungu, F. Matsuda, T. Matsumura, X. Meng, N. J. Miller, H. Morii, S. Moyerman,

M. J. Myers, M. Navaroli, H. Nishino, H. Paar, J. Peloton, E. Quealy, G. Rebeiz, C. L. Reichardt, P. L. Richards, C. Ross, I. Schanning, D. E. Schenck, B. Sherwin, A. Shimizu, C. Shimmin, M. Shimon, P. Siritanasak, G. Smecher, H. Spieler, N. Stebor, B. Steinbach, R. Stompor, A. Suzuki, S. Takakura, T. Tomaru, B. Wilson, A. Yadav, O. Zahn, and Polarbear Collaboration. Measurement of the Cosmic Microwave Background Polarization Lensing Power Spectrum with the POLARBEAR Experiment. *Phys. Rev. Lett.*, 113(2):021301, July 2014.

[33] D. Hanson, S. Hoover, A. Crites, P. A. R. Ade, K. A. Aird, J. E. Austermann, J. A. Beall, A. N. Bender, B. A. Benson, L. E. Bleem, J. J. Bock, J. E. Carlstrom, C. L. Chang, H. C. Chiang, H. M. Cho, A. Conley, T. M. Crawford, T. de Haan, M. A. Dobbs, W. Everett, J. Gallicchio, J. Gao, E. M. George, N. W. Halverson, N. Harrington, J. W. Henning, G. C. Hilton, G. P. Holder, W. L. Holzapfel, J. D. Hrubes, N. Huang, J. Hubmayr, K. D. Irwin, R. Keisler, L. Knox, A. T. Lee, E. Leitch, D. Li, C. Liang, D. Luong-Van, G. Marsden, J. J. McMahon, J. Mehl, S. S. Meyer, L. Mocanu, T. E. Montroy, T. Natoli, J. P. Nibarger, V. Novosad, S. Padin, C. Pryke, C. L. Reichardt, J. E. Ruhl, B. R. Saliwanchik, J. T. Sayre, K. K. Schaffer, B. Schulz, G. Smecher, A. A. Stark, K. T. Story, C. Tucker, K. Vanderlinde, J. D. Vieira, M. P. Viero, G. Wang, V. Yefremenko, O. Zahn, and M. Zemcov. Detection of B-Mode Polarization in the Cosmic Microwave Background with Data from the South Pole Telescope. *Phys. Rev. Lett.*, 111(14):141301, October 2013.

[34] BICEP2/Keck Collaboration, Planck Collaboration, P. A. R. Ade, N. Aghanim, Z. Ahmed, R. W. Aikin, K. D. Alexander, M. Arnaud, J. Aumont, C. Baccigalupi, A. J. Banday, D. Barkats, R. B. Barreiro, J. G. Bartlett, N. Bartolo, E. Battaner, K. Benabed, A. Benoît, A. Benoit-Lévy, S. J. Benton, J. P. Bernard, M. Bersanelli, P. Bielewicz, C. A. Bischoff, J. J. Bock, A. Bonaldi, L. Bonavera, J. R. Bond, J. Borrill, F. R. Bouchet, F. Boulanger, J. A. Brevik, M. Bucher, I. Buder, E. Bullock, C. Burigana, R. C. Butler, V. Buza, E. Calabrese, J. F. Cardoso, A. Catalano, A. Challinor, R. R. Chary, H. C. Chiang, P. R. Christensen, L. P. L. Colombo, C. Combet, J. Connors, F. Couchot, A. Coulais, B. P. Crill, A. Curto, F. Cuttaia, L. Danese, R. D. Davies, R. J. Davis, P. de Bernardis, A. De Rosa, G. de Zotti, J. Delabrouille, J. M. Delouis, F. X. Désert, C. Dickinson, J. M. Diego, H. Dole, S. Donzelli, O. Doré, M. Douspis, C. D. Dowell, L. Duband, A. Ducout, J. Dunkley, X. Dupac, C. Dvorkin, G. Efstathiou, F. Elsner, T. A. Enßlin, H. K. Eriksen, E. Falgarone, J. P. Filippini, F. Finelli, S. Fliescher, O. Forni, M. Frailis, A. A. Fraisse, E. Franceschi, A. Frejsel, S. Galeotta, S. Galli, K. Ganga, T. Ghosh, M. Giard, E. Gjerløw, S. R. Golwala, J. González-Nuevo, K. M. Górski, S. Gratton, A. Gregorio, A. Gruppuso, J. E. Gudmundsson, M. Halpern, F. K. Hansen, D. Hanson, D. L. Harrison, M. Hasselfield, G. Helou, S. Henrot-Versillé, D. Herranz, S. R. Hildebrandt, G. C. Hilton, E. Hivon, M. Hobson, W. A. Holmes, W. Hovest, V. V. Hristov, K. M. Huffenberger, H. Hui, G. Hurier, K. D. Irwin, A. H. Jaffe, T. R. Jaffe, J. Jewell, W. C. Jones, M. Juvela, A. Karakci, K. S. Karkare, J. P. Kaufman, B. G.

Keating, S. Kefeli, E. Keihänen, S. A. Kernasovskiy, R. Keskitalo, T. S. Kisner, R. Kneissl, J. Knoche, L. Knox, J. M. Kovac, N. Krachmalnicoff, M. Kunz, C. L. Kuo, H. Kurki-Suonio, G. Lagache, A. Lähteenmäki, J. M. Lamarre, A. Lasenby, M. Lattanzi, C. R. Lawrence, E. M. Leitch, R. Leonardi, F. Levrier, A. Lewis, M. Liguori, P. B. Lilje, M. Linden-Vørnle, M. López-Caniego, P. M. Lubin, M. Lueker, J. F. Macías-Pérez, B. Maffei, D. Maino, N. Mandolesi, A. Mangilli, M. Maris, P. G. Martin, E. Martínez-González, S. Masi, P. Mason, S. Matarrese, K. G. Megerian, P. R. Meinhold, A. Melchiorri, L. Mendes, A. Mennella, M. Migliaccio, S. Mitra, M. A. Miville-Deschênes, A. Moneti, L. Montier, G. Morgante, D. Mortlock, A. Moss, D. Munshi, J. A. Murphy, P. Naselsky, F. Nati, P. Natoli, C. B. Netterfield, H. T. Nguyen, H. U. Nørgaard-Nielsen, F. Noviello, D. Novikov, I. Novikov, R. O'Brient, R. W. Ogburn, A. Orlando, L. Pagano, F. Pajot, R. Paladini, D. Paoletti, B. Partridge, F. Pasian, G. Patanchon, T. J. Pearson, O. Perdereau, L. Perotto, V. Pettorino, F. Piacentini, M. Piat, D. Pietrobon, S. Plaszczynski, E. Pointecouteau, G. Polenta, N. Ponthieu, G. W. Pratt, S. Prunet, C. Pryke, J. L. Puget, J. P. Rachen, W. T. Reach, R. Rebolo, M. Reinecke, M. Remazeilles, C. Renault, A. Renzi, S. Richter, I. Ristorcelli, G. Rocha, M. Rossetti, G. Roudier, M. Rowan-Robinson, J. A. Rubiño-Martín, B. Rusholme, M. Sandri, D. Santos, M. Savelainen, G. Savini, R. Schwarz, D. Scott, M. D. Seiffert, C. D. Sheehy, L. D. Spencer, Z. K. Staniszewski, V. Stolyarov, R. Sudiwala, R. Sunyaev, D. Sutton, A. S. Suur-Uski, J. F. Sygnet, J. A. Tauber, G. P. Teply, L. Terenzi, K. L. Thompson, L. Toffolatti, J. E. Tolan, M. Tomasi, M. Tristram, M. Tucci, A. D. Turner, L. Valenziano, J. Valiviita, B. van Tent, L. Vibert, P. Vielva, A. G. Vieregg, F. Villa, L. A. Wade, B. D. Wandelt, R. Watson, A. C. Weber, I. K. Wehus, M. White, S. D. M. White, J. Willmert, C. L. Wong, K. W. Yoon, D. Yvon, A. Zacchei, A. Zonca, Bicep2/Keck, and Planck Collaborations. Joint Analysis of BICEP2/Keck Array and Planck Data. *Phys. Rev. Lett.*, 114(10):101301, March 2015.

[35] Oliver P. Lay and Nils W. Halverson. The Impact of Atmospheric Fluctuations on Degree-Scale Imaging of the Cosmic Microwave Background. *ApJ*, 543(2):787–798, November 2000.

[36] A. Kusaka, T. Essinger-Hileman, J. W. Appel, P. Gallardo, K. D. Irwin, N. Jarosik, M. R. Nolta, L. A. Page, L. P. Parker, S. Raghunathan, J. L. Sievers, S. M. Simon, S. T. Staggs, and K. Visnjic. Modulation of cosmic microwave background polarization with a warm rapidly rotating half-wave plate on the Atacama B-Mode Search instrument. *Review of Scientific Instruments*, 85(2):024501, February 2014.

[37] Planck Collaboration, P. A. R. Ade, M. I. R. Alves, G. Aniano, C. Armitage-Caplan, M. Arnaud, F. Atrio-Barandela, J. Aumont, C. Baccigalupi, A. J. Banday, R. B. Barreiro, E. Battaner, K. Benabed, A. Benoit-Lévy, J. P. Bernard, M. Bersanelli, P. Bielewicz, J. J. Bock, J. R. Bond, J. Borrill, F. R. Bouchet, F. Boulanger, C. Burigana, J. F. Cardoso, A. Catalano, A. Chamballu, H. C. Chiang, L. P. L. Colombo, C. Combet, F. Couchot, A. Coulais, B. P. Crill,

A. Curto, F. Cuttaia, L. Danese, R. D. Davies, R. J. Davis, P. de Bernardis, G. de Zotti, J. Delabrouille, F. X. Désert, C. Dickinson, J. M. Diego, S. Donzelli, O. Doré, M. Douspis, J. Dunkley, X. Dupac, T. A. Enßlin, H. K. Eriksen, E. Falgarone, F. Finelli, O. Forni, M. Frailis, A. A. Fraisse, E. Franceschi, S. Galeotta, K. Ganga, T. Ghosh, M. Giard, J. González-Nuevo, K. M. Górski, A. Gregorio, A. Gruppuso, V. Guillet, F. K. Hansen, D. L. Harrison, G. Helou, C. Hernández-Monteagudo, S. R. Hildebrandt, E. Hivon, M. Hobson, W. A. Holmes, A. Hornstrup, A. H. Jaffe, T. R. Jaffe, W. C. Jones, E. Keihänen, R. Keskitalo, T. S. Kisner, R. Kneissl, J. Knoche, M. Kunz, H. Kurki-Suonio, G. Lagache, J. M. Lamarre, A. Lasenby, C. R. Lawrence, J. P. Leahy, R. Leonardi, F. Levrier, M. Liguori, P. B. Lilje, M. Linden-Vørnle, M. López-Caniego, P. M. Lubin, J. F. Macías-Pérez, B. Maffei, A. M. Magalhães, D. Maino, N. Mandolesi, M. Maris, D. J. Marshall, P. G. Martin, E. Martínez-González, S. Masi, S. Matarrese, P. Mazzotta, A. Melchiorri, L. Mendes, A. Mennella, M. Migliaccio, M. A. Miville-Deschênes, A. Moneti, L. Montier, G. Morgante, D. Mortlock, D. Munshi, J. A. Murphy, P. Naselsky, F. Nati, P. Natoli, C. B. Netterfield, F. Noviello, D. Novikov, I. Novikov, N. Oppermann, C. A. Oxborrow, L. Pagano, F. Pajot, D. Paoletti, F. Pasian, O. Perdereau, L. Perotto, F. Perrotta, F. Piacentini, D. Pietrobon, S. Plaszczynski, E. Pointecouteau, G. Polenta, L. Popa, G. W. Pratt, J. P. Rachen, W. T. Reach, M. Reinecke, M. Remazeilles, C. Renault, S. Ricciardi, T. Riller, I. Ristorcelli, G. Rocha, C. Rosset, G. Roudier, J. A. Rubiño-Martín, B. Rusholme, E. Salerno, M. Sandri, G. Savini, D. Scott, L. D. Spencer, V. Stolyarov, R. Stompor, R. Sudiwala, D. Sutton, A. S. Suur-Uski, J. F. Sygnet, J. A. Tauber, L. Terenzi, L. Toffolatti, M. Tomasi, M. Tristram, M. Tucci, L. Valenziano, J. Valiviita, B. Van Tent, P. Vielva, F. Villa, B. D. Wandelt, A. Zacchei, and A. Zonca. Planck intermediate results. XXII. Frequency dependence of thermal emission from Galactic dust in intensity and polarization. *A&A*, 576:A107, April 2015.

[38] Peter Ade, James Aguirre, Zeeshan Ahmed, Simone Aiola, Aamir Ali, David Alonso, Marcelo A. Alvarez, Kam Arnold, Peter Ashton, Jason Austermann, Humna Awan, Carlo Baccigalupi, Taylor Baildon, Darcy Barron, Nick Battaglia, Richard Battye, Eric Baxter, Andrew Bazarko, James A. Beall, Rachel Bean, Dominic Beck, Shawn Beckman, Benjamin Beringue, Federico Bianchini, Steven Boada, David Boettger, J. Richard Bond, Julian Borrill, Michael L. Brown, Sarah Marie Bruno, Sean Bryan, Erminia Calabrese, Victoria Calafut, Paolo Calisse, Julien Carron, Anthony Challinor, Grace Chesmore, Yuji Chinone, Jens Chluba, Hsiao-Mei Sherry Cho, Steve Choi, Gabriele Coppi, Nicholas F. Cothard, Kevin Coughlin, Devin Crichton, Kevin D. Crowley, Kevin T. Crowley, Ari Cukierman, John M. D'Ewart, Rolando Dünner, Tijmen de Haan, Mark Devlin, Simon Dicker, Joy Didier, Matt Dobbs, Bradley Dober, Cody J. Duell, Shannon Duff, Adri Duivenvoorden, Jo Dunkley, John Dusatko, Josquin Errard, Giulio Fabbian, Stephen Feeney, Simone Ferraro, Pedro Fluxà, Katherine Freese, Josef C. Frisch, Andrei Frolov, George Fuller, Brittany Fuzia, Nicholas Galitzki, Patricio A. Gallardo, Jose Tomas Galvez Ghersi, Jiansong

Gao, Eric Gawiser, Martina Gerbino, Vera Gluscevic, Neil Goeckner-Wald, Joseph Golec, Sam Gordon, Megan Gralla, Daniel Green, Arpi Grigorian, John Groh, Chris Groppi, Yilun Guan, Jon E. Gudmundsson, Dongwon Han, Peter Hargrave, Masaya Hasegawa, Matthew Hasselfield, Makoto Hattori, Victor Haynes, Masashi Hazumi, Yizhou He, Erin Healy, Shawn W. Henderson, Carlos Hervias-Caimapo, Charles A. Hill, J. Colin Hill, Gene Hilton, Matt Hilton, Adam D. Hincks, Gary Hinshaw, Renée Hložek, Shirley Ho, Shuay-Pwu Patty Ho, Logan Howe, Zhiqi Huang, Johannes Hubmayr, Kevin Huffenberger, John P. Hughes, Anna Ijjas, Margaret Ikape, Kent Irwin, Andrew H. Jaffe, Bhuvnesh Jain, Oliver Jeong, Daisuke Kaneko, Ethan D. Karpel, Nobuhiko Katayama, Brian Keating, Sarah S. Kernasovskiy, Reijo Keskitalo, Theodore Kisner, Kenji Kiuchi, Jeff Klein, Kenda Knowles, Brian Koopman, Arthur Kosowsky, Nicoletta Krachmalnicoff, Stephen E. Kuenstner, Chao-Lin Kuo, Akito Kusaka, Jacob Lashner, Adrian Lee, Eunseong Lee, David Leon, Jason S. Y. Leung, Antony Lewis, Yaqiong Li, Zack Li, Michele Limon, Eric Linder, Carlos Lopez-Caraballo, Thibaut Louis, Lindsay Lowry, Marius Lungu, Mathew Madhavacheril, Daisy Mak, Felipe Maldonado, Hamdi Mani, Ben Mates, Frederick Matsuda, Loïc Maurin, Phil Mauskopf, Andrew May, Nialh McCallum, Chris McKenney, Jeff McMahon, P. Daniel Meerburg, Joel Meyers, Amber Miller, Mark Mirmelstein, Kavilan Moodley, Moritz Munchmeyer, Charles Munson, Sigurd Naess, Federico Nati, Martin Navaroli, Laura Newburgh, Ho Nam Nguyen, Michael Niemack, Haruki Nishino, John Orlowski-Scherer, Lyman Page, Bruce Partridge, Julien Peloton, Francesca Perrotta, Lucio Piccirillo, Giampaolo Pisano, Davide Poletti, Roberto Puddu, Giuseppe Puglisi, Chris Raum, Christian L. Reichardt, Mathieu Remazeilles, Yoel Rephaeli, Dominik Riechers, Felipe Rojas, Anirban Roy, Sharon Sadeh, Yuki Sakurai, Maria Salatino, Mayuri Sathyanarayana Rao, Emmanuel Schaan, Marcel Schmittfull, Neelima Sehgal, Joseph Seibert, Uros Seljak, Blake Sherwin, Meir Shimon, Carlos Sierra, Jonathan Sievers, Precious Sikhosana, Maximiliano Silva-Feaver, Sara M. Simon, Adrian Sinclair, Praween Siritanasak, Kendrick Smith, Stephen R. Smith, David Spergel, Suzanne T. Staggs, George Stein, Jason R. Stevens, Radek Stompor, Aritoki Suzuki, Osamu Tajima, Satoru Takakura, Grant Teply, Daniel B. Thomas, Ben Thorne, Robert Thornton, Hy Trac, Calvin Tsai, Carole Tucker, Joel Ullom, Sunny Vagnozzi, Alexander van Engelen, Jeff Van Lanen, Daniel D. Van Winkle, Eve M. Vavagiakis, Clara Vergès, Michael Vissers, Kasey Wagoner, Samantha Walker, Jon Ward, Ben Westbrook, Nathan Whitehorn, Jason Williams, Joel Williams, Edward J. Wollack, Zhilei Xu, Byeonghee Yu, Cyndia Yu, Fernando Zago, Hezi Zhang, Ningfeng Zhu, and Simons Observatory Collaboration. The Simons Observatory: science goals and forecasts. *J. Cosmology Astropart. Phys.*, 2019(2):056, February 2019.

[39] Kyle S. Dawson, David J. Schlegel, Christopher P. Ahn, Scott F. Anderson, Éric Aubourg, Stephen Bailey, Robert H. Barkhouser, Julian E. Bautista, Alessandra Beifiori, Andreas A. Berlind, Vaishali Bhardwaj, Dmitry Bizyaev, Cullen H. Blake, Michael R. Blanton, Michael Blomqvist, Adam S. Bolton, Arnaud Borde, Jo Bovy, W. N. Brandt, Howard Brewington, Jon Brinkmann, Peter J. Brown,

Joel R. Brownstein, Kevin Bundy, N. G. Busca, William Carithers, Aurelio R. Carnero, Michael A. Carr, Yanmei Chen, Johan Comparat, Natalia Connolly, Frances Cope, Rupert A. C. Croft, Antonio J. Cuesta, Luiz N. da Costa, James R. A. Davenport, Timothée Delubac, Roland de Putter, Saurav Dhital, Anne Ealet, Garrett L. Ebelke, Daniel J. Eisenstein, S. Escoffier, Xiaohui Fan, N. Filiz Ak, Hayley Finley, Andreu Font-Ribera, R. Génova-Santos, James E. Gunn, Hong Guo, Daryl Haggard, Patrick B. Hall, Jean-Christophe Hamilton, Ben Harris, David W. Harris, Shirley Ho, David W. Hogg, Diana Holder, Klaus Honscheid, Joe Huehnerhoff, Beatrice Jordan, Wendell P. Jordan, Guinevere Kauffmann, Eyal A. Kazin, David Kirkby, Mark A. Klaene, Jean-Paul Kneib, Jean-Marc Le Goff, Khee-Gan Lee, Daniel C. Long, Craig P. Loomis, Britt Lundgren, Robert H. Lupton, Marcio A. G. Maia, Martin Makler, Elena Malanushenko, Viktor Malanushenko, Rachel Mandelbaum, Marc Manera, Claudia Maraston, Daniel Margala, Karen L. Masters, Cameron K. McBride, Patrick McDonald, Ian D. McGreer, Richard G. McMahon, Olga Mena, Jordi Miralda-Escudé, Antonio D. Montero-Dorta, Francesco Montesano, Demitri Muna, Adam D. Myers, Tracy Naugle, Robert C. Nichol, Pasquier Noterdaeme, Sebastián E. Nuza, Matthew D. Olmstead, Audrey Oravetz, Daniel J. Oravetz, Russell Owen, Nikhil Padmanabhan, Nathalie Palanque-Delabrouille, Kaike Pan, John K. Parejko, Isabelle Pâris, Will J. Percival, Ismael Pérez-Fournon, Ignasi Pérez-Ràfols, Patrick Petitjean, Robert Pfaffenberger, Janine Pforr, Matthew M. Pieri, Francisco Prada, Adrian M. Price-Whelan, M. Jordan Raddick, Rafael Rebolo, James Rich, Gordon T. Richards, Constance M. Rockosi, Natalie A. Roe, Ashley J. Ross, Nicholas P. Ross, Graziano Rossi, J. A. Rubiño-Martin, Lado Samushia, Ariel G. Sánchez, Conor Sayres, Sarah J. Schmidt, Donald P. Schneider, C. G. Scóccola, Hee-Jong Seo, Alaina Shelden, Erin Sheldon, Yue Shen, Yiping Shu, Anže Slosar, Stephen A. Smee, Stephanie A. Snedden, Fritz Stauffer, Oliver Steele, Michael A. Strauss, Alina Streblyanska, Nao Suzuki, Molly E. C. Swanson, Tomer Tal, Masayuki Tanaka, Daniel Thomas, Jeremy L. Tinker, Rita Tojeiro, Christy A. Tremonti, M. Vargas Magaña, Licia Verde, Matteo Viel, David A. Wake, Mike Watson, Benjamin A. Weaver, David H. Weinberg, Benjamin J. Weiner, Andrew A. West, Martin White, W. M. Wood-Vasey, Christophe Yeche, Idit Zehavi, Gong-Bo Zhao, and Zheng Zheng. The Baryon Oscillation Spectroscopic Survey of SDSS-III. *AJ*, 145(1):10, January 2013.

[40] Brenna L. Flaugher, Timothy M. C. Abbott, Jim Annis, Michelle L. Antonik, Jim Bailey, Otger Ballester, Joseph P. Bernstein, Rebecca Bernstein, Marco Bonati, Gale Bremer, Jorge Briones, David Brooks, Elizabeth J. Buckley-Geer, Julia Campa, Laia Cardiel-Sas, Francisco Castander, Javier Castilla, Herman Cease, Steve Chappa, Edward C. Chi, Luis da Costa, Darren L. DePoy, Gregory Derylo, Juan De Vicente, H. Thomas Diehl, Peter Doel, Juan Estrada, Jacob Eiting, Anne Elliott, David Finley, Josh Frieman, Enrique Gaztanaga, David Gerdes, Mike Gladders, V. Guarino, G. Gutierrez, Jim Grudzinski, Bill Hanlon, Jiangang Hao, Steve Holland, Klaus Honscheid, Dave Huffman, Cheryl Jackson, Inga Karliner, Daekwang Kau, Steve Kent, Kurt Krempetz, John Krider, Mark

Kozlovsky, Donna Kubik, Kyler W. Kuehn, Stephen E. Kuhlmann, Kevin Kuk, Ofer Lahav, Peter Lewis, Huan Lin, Wolfgang Lorenzon, Stuart Marshall, Gustavo Martínez, Timothy McKay, Wyatt Merritt, Mark Meyer, Ramon Miquel, Jim Morgan, Peter Moore, Todd Moore, Brian Nord, R. Ogando, Jamieson Olsen, John Peoples, Andreas Plazas, Natalie Roe, Aaron Roodman, B. Rossetto, E. Sanchez, Vic Scarpine, Terry Schalk, Rafe Schindler, Ricardo Schmidt, Richard Schmitt, Mike Schubnell, Kenneth Schultz, M. Selen, S. Serrano, Terri Shaw, Vaidis Simaitis, Jean Slaughter, R. Christopher Smith, Hal Spinka, Andy Stefanik, Walter Stuermer, Adam Sypniewski, Rick Talaga, Greg Tarle, Jon Thaler, Doug Tucker, Alistair R. Walker, Curtis Weaverdyck, William Wester, Robert J. Woods, Sue Worswick, and Allen Zhao. Status of the dark energy survey camera (DECam) project. In Ian S. McLean, Suzanne K. Ramsay, and Hideki Takami, editors, *Ground-based and Airborne Instrumentation for Astronomy III*, volume 7735, pages 186 – 199. International Society for Optics and Photonics, SPIE, 2010.

[41] Michael Levi, Chris Bebek, Timothy Beers, Robert Blum, Robert Cahn, Daniel Eisenstein, Brenna Flaugher, Klaus Honscheid, Richard Kron, Ofer Lahav, Patrick McDonald, Natalie Roe, David Schlegel, and representing the DESI collaboration. The DESI Experiment, a whitepaper for Snowmass 2013. *arXiv e-prints*, page arXiv:1308.0847, August 2013.

[42] Satoshi Miyazaki, Yutaka Komiyama, Hidehiko Nakaya, Yukiko Kamata, Yoshi Doi, Takashi Hamana, Hiroshi Karoji, Hisanori Furusawa, Satoshi Kawanomoto, Tomoki Morokuma, Yuki Ishizuka, Kyoji Nariai, Yoko Tanaka, Fumihiro Uraguchi, Yousuke Utsumi, Yoshiyuki Obuchi, Yuki Okura, Masamune Oguri, Tadafumi Takata, Daigo Tomono, Tomio Kurakami, Kazuhito Namikawa, Tomonori Usuda, Hitomi Yamanoi, Tsuyoshi Terai, Hatsue Uekiyo, Yoshihiko Yamada, Michitaro Koike, Hiro Aihara, Yuki Fujimori, Sogo Mineo, Hironao Miyatake, Naoki Yasuda, Jun Nishizawa, Tomoki Saito, Manobu Tanaka, Tomohisa Uchida, Nobu Katayama, Shiang-Yu Wang, Hsin-Yo Chen, Robert Lupton, Craig Loomis, Steve Bickerton, Paul Price, Jim Gunn, Hisanori Suzuki, Yasuhito Miyazaki, Masaharu Muramatsu, Koei Yamamoto, Makoto Endo, Yutaka Ezaki, Noboru Itoh, Yoshinori Miwa, Hideo Yokota, Toru Matsuda, Ryuichi Ebinuma, and Kunio Takeshi. Hyper Suprime-Cam. In Ian S. McLean, Suzanne K. Ramsay, and Hideki Takami, editors, *Ground-based and Airborne Instrumentation for Astronomy IV*, volume 8446, pages 327–335. International Society for Optics and Photonics, SPIE, 2012.

[43] Željko Ivezić, Steven M. Kahn, J. Anthony Tyson, Bob Abel, Emily Acosta, Robyn Allsman, David Alonso, Yusra AlSayyad, Scott F. Anderson, John Andrew, and et al. Lsst: From science drivers to reference design and anticipated data products. *The Astrophysical Journal*, 873(2):111, March 2019.

[44] T. J. Waskett, B. Sibthorpe, M. J. Griffin, and P. F. Chanial. Determining the

139

optimum scan map strategy for Herschel-SPIRE using the SPIRE photometer simulator. *MNRAS*, 381(4):1583–1590, November 2007.

[45] J. T. Ward, D. Alonso, J. Errard, M. J. Devlin, and M. Hasselfield. The Effects of Bandpass Variations on Foreground Removal Forecasts for Future CMB Experiments. *ApJ*, 861(2):82, July 2018.

[46] Wayne Holland, Steve Watson, Colin Cunningham, Tom Bradshaw, Martin Crook, Andy Vick, David Pearson, Maria Milanova, Steve Greenland, Stephen Todd, Chris Waring, Ewan Fitzsimons, and Donald MacLeod. CubeSats for infrared astronomy. In Makenzie Lystrup, Howard A. MacEwen, Giovanni G. Fazio, Natalie Batalha, Nicholas Siegler, and Edward C. Tong, editors, *Space Telescopes and Instrumentation 2018: Optical, Infrared, and Millimeter Wave*, volume 10698, pages 560 – 575. International Society for Optics and Photonics, SPIE, 2018.

[47] Atmosphere model. https://almascience.eso.org/about-alma/atmosphere-model, 2021.

[48] R. J. Thornton, P. A. R. Ade, S. Aiola, F. E. Angilè, M. Amiri, J. A. Beall, D. T. Becker, H. M. Cho, S. K. Choi, P. Corlies, K. P. Coughlin, R. Datta, M. J. Devlin, S. R. Dicker, R. Dünner, J. W. Fowler, A. E. Fox, P. A. Gallardo, J. Gao, E. Grace, M. Halpern, M. Hasselfield, S. W. Henderson, G. C. Hilton, A. D. Hincks, S. P. Ho, J. Hubmayr, K. D. Irwin, J. Klein, B. Koopman, Dale Li, T. Louis, M. Lungu, L. Maurin, J. McMahon, C. D. Munson, S. Naess, F. Nati, L. Newburgh, J. Nibarger, M. D. Niemack, P. Niraula, M. R. Nolta, L. A. Page, C. G. Pappas, A. Schillaci, B. L. Schmitt, N. Sehgal, J. L. Sievers, S. M. Simon, S. T. Staggs, C. Tucker, M. Uehara, J. van Lanen, J. T. Ward, and E. J. Wollack. The Atacama Cosmology Telescope: The Polarization-sensitive ACTPol Instrument. *ApJS*, 227(2):21, December 2016.

[49] F. De Bernardis, J. R. Stevens, M. Hasselfield, D. Alonso, J. R. Bond, E. Calabrese, S. K. Choi, K. T. Crowley, M. Devlin, J. Dunkley, P. A. Gallardo, S. W. Henderson, M. Hilton, R. Hlozek, S. P. Ho, K. Huffenberger, B. J. Koopman, A. Kosowsky, T. Louis, M. S. Madhavacheril, J. McMahon, S. Næss, F. Nati, L. Newburgh, M. D. Niemack, L. A. Page, M. Salatino, A. Schillaci, B. L. Schmitt, N. Sehgal, J. L. Sievers, S. M. Simon, D. N. Spergel, S. T. Staggs, A. van Engelen, E. M. Vavagiakis, and E. J. Wollack. Survey strategy optimization for the Atacama Cosmology Telescope. In Alison B. Peck, Robert L. Seaman, and Chris R. Benn, editors, *Observatory Operations: Strategies, Processes, and Systems VI*, volume 9910 of *Society of Photo-Optical Instrumentation Engineers (SPIE) Conference Series*, page 991014, July 2016.

[50] Charles Munson. *Technology Development for Cosmic Microwave Background Cosmology*. PhD thesis, University of Michigan, 2016.

[51] S. M. Duff, J. Austermann, J. A. Beall, D. Becker, R. Datta, P. A. Gallardo, S. W. Henderson, G. C. Hilton, S. P. Ho, J. Hubmayr, B. J. Koopman, D. Li, J. McMahon, F. Nati, M. D. Niemack, C. G. Pappas, M. Salatino, B. L. Schmitt, S. M. Simon, S. T. Staggs, J. R. Stevens, J. Van Lanen, E. M. Vavagiakis, J. T. Ward, and E. J. Wollack. Advanced ACTPol Multichroic Polarimeter Array Fabrication Process for 150 mm Wafers. *Journal of Low Temperature Physics*, 184(3-4):634–641, August 2016.

[52] Jonathan T. Ward, Jason Austermann, James A. Beall, Steve K. Choi, Kevin T. Crowley, Mark J. Devlin, Shannon M. Duff, Patricio A. Gallardo, Shawn W. Henderson, Shuay-Pwu Patty Ho, Gene Hilton, Johannes Hubmayr, Niloufar Khavari, Jeffrey Klein, Brian J. Koopman, Dale Li, Jeffrey McMahon, Grace Mumby, Federico Nati, Michael D. Niemack, Lyman A. Page, Maria Salatino, Alessandro Schillaci, Benjamin L. Schmitt, Sara M. Simon, Suzanne T. Staggs, Robert Thornton, Joel N. Ullom, Eve M. Vavagiakis, and Edward J. Wollack. Mechanical designs and development of TES bolometer detector arrays for the Advanced ACTPol experiment. In Wayne S. Holland and Jonas Zmuidzinas, editors, *Millimeter, Submillimeter, and Far-Infrared Detectors and Instrumentation for Astronomy VIII*, volume 9914 of *Society of Photo-Optical Instrumentation Engineers (SPIE) Conference Series*, page 991437, July 2016.

[53] J. Dunkley, A. Amblard, C. Baccigalupi, M. Betoule, D. Chuss, A. Cooray, J. Delabrouille, C. Dickinson, G. Dobler, J. Dotson, H. K. Eriksen, D. Finkbeiner, D. Fixsen, P. Fosalba, A. Fraisse, C. Hirata, A. Kogut, J. Kristiansen, C. Lawrence, A. M. Magalhães, M. A. Miville-Deschênes, S. Meyer, A. Miller, S. K. Naess, L. Page, H. V. Peiris, N. Phillips, E. Pierpaoli, G. Rocha, J. E. Vaillancourt, and L. Verde. Prospects for polarized foreground removal. In Scott Dodelson, Daniel Baumann, Asantha Cooray, Joanna Dunkley, Aurelien Fraisse, Mark G. Jackson, Alan Kogut, Lawrence Krauss, Matias Zaldarriaga, and Kendrick Smith, editors, *CMB Polarization Workshop: Theory and Foregrounds: CMBPol Mission Concept Study*, volume 1141 of *American Institute of Physics Conference Series*, pages 222–264, June 2009.

[54] Sara M. Simon, Jason Austermann, James A. Beall, Steve K. Choi, Kevin P. Coughlin, Shannon M. Duff, Patricio A. Gallardo, Shawn W. Henderson, Felicity B. Hills, Shuay-Pwu Patty Ho, Johannes Hubmayr, Alec Josaitis, Brian J. Koopman, Jeff J. McMahon, Federico Nati, Laura Newburgh, Michael D. Niemack, Maria Salatino, Alessandro Schillaci, Benjamin L. Schmitt, Suzanne T. Staggs, Eve M. Vavagiakis, Jonathan Ward, and Edward J. Wollack. The design and characterization of wideband spline-profiled feedhorns for Advanced ACTPol. In Wayne S. Holland and Jonas Zmuidzinas, editors, *Millimeter, Submillimeter, and Far-Infrared Detectors and Instrumentation for Astronomy VIII*, volume 9914 of *Society of Photo-Optical Instrumentation Engineers (SPIE) Conference Series*, page 991416, July 2016.

[55] Rahul Datta. *The First Multichroic Receiver and Results from ACTPol.* PhD thesis, University of Michigan, 2016.

[56] K. D. Irwin and G. C. Hilton. *Transition-Edge Sensors*, volume 99, pages 81–97. Springer, July 2005.

[57] L. D. Jennings and C. A. Swenson. Effects of pressure on the superconducting transition temperatures of sn, in, ta, tl, and hg. *Phys. Rev.*, 112:31–43, October 1958.

[58] Piet A. J. de Korte, Joern Beyer, Steve Deiker, Gene C. Hilton, Kent D. Irwin, Mike MacIntosh, Sae Woo Nam, Carl D. Reintsema, Leila R. Vale, and Martin E. Huber. Time-division superconducting quantum interference device multiplexer for transition-edge sensors. *Review of Scientific Instruments*, 74(8):3807–3815, August 2003.

[59] Nicholas Galitzki, Aamir Ali, Kam S. Arnold, Peter C. Ashton, Jason E. Austermann, Carlo Baccigalupi, Taylor Baildon, Darcy Barron, James A. Beall, Shawn Beckman, Sarah Marie M. Bruno, Sean Bryan, Paolo G. Calisse, Grace E. Chesmore, Yuji Chinone, Steve K. Choi, Gabriele Coppi, Kevin D. Crowley, Kevin T. Crowley, Ari Cukierman, Mark J. Devlin, Simon Dicker, Bradley Dober, Shannon M. Duff, Jo Dunkley, Giulio Fabbian, Patricio A. Gallardo, Martina Gerbino, Neil Goeckner-Wald, Joseph E. Golec, Jon E. Gudmundsson, Erin E. Healy, Shawn Henderson, Charles A. Hill, Gene C. Hilton, Shuay-Pwu Patty Ho, Logan A. Howe, Johannes Hubmayr, Oliver Jeong, Brian Keating, Brian J. Koopman, Kenji Kiuchi, Akito Kusaka, Jacob Lashner, Adrian T. Lee, Yaqiong Li, Michele Limon, Marius Lungu, Frederick Matsuda, Philip D. Mauskopf, Andrew J. May, Nialh McCallum, Jeff McMahon, Federico Nati, Michael D. Niemack, John L. Orlowski-Scherer, Stephen C. Parshley, Lucio Piccirillo, Mayuri Sathyanarayana Rao, Christopher Raum, Maria Salatino, Joseph S. Seibert, Carlos Sierra, Max Silva-Feaver, Sara M. Simon, Suzanne T. Staggs, Jason R. Stevens, Aritoki Suzuki, Grant Teply, Robert Thornton, Calvin Tsai, Joel N. Ullom, Eve M. Vavagiakis, Michael R. Vissers, Benjamin Westbrook, Edward J. Wollack, Zhilei Xu, and Ningfeng Zhu. The Simons Observatory: instrument overview. In Jonas Zmuidzinas and Jian-Rong Gao, editors, *Millimeter, Submillimeter, and Far-Infrared Detectors and Instrumentation for Astronomy IX*, volume 10708 of *Society of Photo-Optical Instrumentation Engineers (SPIE) Conference Series*, page 1070804, July 2018.

[60] Jason R. Stevens, Neil Goeckner-Wald, Reijo Keskitalo, Nialh McCallum, Aamir Ali, Julian Borrill, Michael L. Brown, Yuji Chinone, Patricio A. Gallardo, Akito Kusaka, Adrian T. Lee, Jeff McMahon, Michael D. Niemack, Lyman Page, Giuseppe Puglisi, Maria Salatino, Suet Ying D. Mak, Grant Teply, Daniel B. Thomas, Eve M. Vavagiakis, Edward J. Wollack, Zhilei Xu, and Ningfeng Zhu. Designs for next generation CMB survey strategies from Chile. In Jonas Zmuidzinas and Jian-Rong Gao, editors, *Millimeter, Submillimeter, and Far-Infrared De-*

tectors and Instrumentation for Astronomy IX, volume 10708 of *Society of Photo-Optical Instrumentation Engineers (SPIE) Conference Series*, page 1070841, July 2018.

[61] Ningfeng Zhu, John L. Orlowski-Scherer, Zhilei Xu, Aamir Ali, Kam S. Arnold, Peter C. Ashton, Gabriele Coppi, Mark J. Devlin, Simon Dicker, Nicholas Galitzki, Patricio A. Gallardo, Shawn W. Henderson, Shuay-Pwu Patty Ho, Johannes Hubmayr, Brian Keating, Adrian T. Lee, Michele Limon, Marius Lungu, Philip D. Mauskopf, Andrew J. May, Jeff McMahon, Michael D. Niemack, Lucio Piccirillo, Giuseppe Puglisi, Mayuri Sathyanarayana Rao, Maria Salatino, Max Silva-Feaver, Sara M. Simon, Suzanne Staggs, Robert Thornton, Joel N. Ullom, Eve M. Vavagiakis, Benjamin Westbrook, and Edward J. Wollack. Simons Observatory large aperture telescope receiver design overview. In Jonas Zmuidzinas and Jian-Rong Gao, editors, *Millimeter, Submillimeter, and Far-Infrared Detectors and Instrumentation for Astronomy IX*, volume 10708 of *Society of Photo-Optical Instrumentation Engineers (SPIE) Conference Series*, page 1070829, July 2018.

[62] Zhilei Xu, Shunsuke Adachi, Peter Ade, J. A. Beall, Tanay Bhandarkar, J. Richard Bond, Grace E. Chesmore, Yuji Chinone, Steve K. Choi, Jake A. Connors, Gabriele Coppi, Nicholas F. Cothard, Kevin D. Crowley, Mark Devlin, Simon Dicker, Bradley Dober, Shannon M. Duff, Nicholas Galitzki, Patricio A. Gallardo, Joseph E. Golec, Jon E. Gudmundsson, Saianeesh K. Haridas, Kathleen Harrington, Carlos Hervias-Caimapo, Shuay-Pwu Patty Ho, Zachary B. Huber, Johannes Hubmayr, Jeffrey Iuliano, Daisuke Kaneko, Anna M. Kofman, Brian J. Koopman, Jack Lashner, Michele Limon, Michael J. Link, Tammy J. Lucas, Frederick Matsuda, Heather McCarrick, Federico Nati, Michael D. Niemack, John Orlowski-Scherer, Lucio Piccirillo, Karen Perez Sarmiento, Emmanuel Schaan, Maximiliano Silva-Feaver, Rita Sonka, Shreya Sutariya, Osamu Tajima, Grant P. Teply, Tomoki Terasaki, Robert Thornton, Carole Tucker, Joel Ullom, Eve M. Vavagiakis, Michael R. Vissers, Samantha Walker, Zachary Whipps, Edward J. Wollack, Mario Zannoni, Ningfeng Zhu, Andrea Zonca, and Simons Observatory Collaboration. The Simons Observatory: The Large Aperture Telescope (LAT). *Research Notes of the American Astronomical Society*, 5(4):100, April 2021.

[63] Zhilei Xu, Tanay Bhandarkar, Gabriele Coppi, Anna Kofman, John L. Orlowski-Scherer, Ningfeng Zhu, Aamir M. Ali, Kam Arnold, Jason E. Austermann, Steve K. Choi, Jake Connors, Nicholas F. Cothard, Mark Devlin, Simon Dicker, Bradley Dober, Shannon M. Duff, Giulio Fabbian, Nicholas Galitzki, Saianeesh Haridas, Katheleen Harrington, Erin Healy, Shuay-Pwu Patty Ho, Johannes Hubmayr, Jeffrey Iuliano, Jack Lashner, Yaqiong Li, Michele Limon, Brian J. Koopman, Heather McCarrick, Jenna Moore, Federico Nati, Michael D. Niemack, Christian L. Reichardt, Karen Sarmiento, Joseph Seibert, Maximiliano Silva-Feaver, Rita F. Sonka, Suzanne Staggs, Robert J. Thornton, Eve M. Vavagiakis, Michael R. Vissers, Samantha Walker, Yuhan Wang, Edward J. Wollack, and Kaiwen Zheng. The Simons Observatory: the Large Aperture Tele-

scope Receiver (LATR) integration and validation results. In *Society of Photo-Optical Instrumentation Engineers (SPIE) Conference Series*, volume 11453 of *Society of Photo-Optical Instrumentation Engineers (SPIE) Conference Series*, page 1145315, December 2020.

[64] Ningfeng Zhu, Tanay Bhandarkar, Gabriele Coppi, Anna M. Kofman, John L. Orlowski-Scherer, Zhilei Xu, Shunsuke Adachi, Peter Ade, Simone Aiola, Jason Austermann, Andrew O. Bazarko, James A. Beall, Sanah Bhimani, J. Richard Bond, Grace E. Chesmore, Steve K. Choi, Jake Connors, Nicholas F. Cothard, Mark Devlin, Simon Dicker, Bradley Dober, Cody J. Duell, Shannon M. Duff, Rolando Dünner, Giulio Fabbian, Nicholas Galitzki, Patricio A. Gallardo, Joseph E. Golec, Saianeesh K. Haridas, Kathleen Harrington, Erin Healy, Shuay-Pwu Patty Ho, Zachary B. Huber, Johannes Hubmayr, Jeffrey Iuliano, Bradley R. Johnson, Brian Keating, Kenji Kiuchi, Brian J. Koopman, Jack Lashner, Adrian T. Lee, Yaqiong Li, Michele Limon, Michael Link, Tammy J. Lucas, Heather McCarrick, Jenna Moore, Federico Nati, Laura B. Newburgh, Michael D. Niemack, Elena Pierpaoli, Michael J. Randall, Karen Perez Sarmiento, Lauren J. Saunders, Joseph Seibert, Carlos Sierra, Rita Sonka, Jacob Spisak, Shreya Sutariya, Osamu Tajima, Grant P. Teply, Robert J. Thornton, Tran Tsan, Carole Tucker, Joel Ullom, Eve M. Vavagiakis, Michael R. Vissers, Samantha Walker, Benjamin Westbrook, Edward J. Wollack, and Mario Zannoni. The Simons Observatory Large Aperture Telescope Receiver. *ApJS*, 256(1):23, September 2021.

[65] Heather McCarrick, Erin Healy, Zeeshan Ahmed, Kam Arnold, Zachary Atkins, Jason E. Austermann, Tanay Bhandarkar, Jim A. Beall, Sarah Marie Bruno, Steve K. Choi, Jake Connors, Nicholas F. Cothard, Kevin D. Crowley, Simon Dicker, Bradley Dober, Cody J. Duell, Shannon M. Duff, Daniel Dutcher, Josef C. Frisch, Nicholas Galitzki, Megan B. Gralla, Jon E. Gudmundsson, Shawn W. Henderson, Gene C. Hilton, Shuay-Pwu Patty Ho, Zachary B. Huber, Johannes Hubmayr, Jeffrey Iuliano, Bradley R. Johnson, Anna M. Kofman, Akito Kusaka, Jack Lashner, Adrian T. Lee, Yaqiong Li, Michael J. Link, Tammy J. Lucas, Marius Lungu, J. A. B. Mates, Jeffrey J. McMahon, Michael D. Niemack, John Orlowski-Scherer, Joseph Seibert, Maximiliano Silva-Feaver, Sara M. Simon, Suzanne Staggs, Aritoki Suzuki, Tomoki Terasaki, Joel N. Ullom, Eve M. Vavagiakis, Leila R. Vale, Jeff Van Lanen, Michael R. Vissers, Yuhan Wang, Edward J. Wollack, Zhilei Xu, Edward Young, Cyndia Yu, Kaiwen Zheng, and Ningfeng Zhu. The Simons Observatory microwave SQUID multiplexing detector module design. *arXiv e-prints*, page arXiv:2106.14797, June 2021.

[66] Akito Kusaka, John Appel, Thomas Essinger-Hileman, James A. Beall, Luis E. Campusano, Hsiao-Mei Cho, Steve K. Choi, Kevin Crowley, Joseph W. Fowler, Patricio Gallardo, Matthew Hasselfield, Gene Hilton, Shuay-Pwu P. Ho, Kent Irwin, Norman Jarosik, Michael D. Niemack, Glen W. Nixon, Michael Nolta, Jr. Page, Lyman A., Gonzalo A. Palma, Lucas Parker, Srinivasan Raghunathan, Carl D. Reintsema, Jonathan Sievers, Sara M. Simon, Suzanne T. Staggs, Ka-

terina Visnjic, and Ki-Won Yoon. Results from the Atacama B-mode Search (ABS) experiment. *JCAP*, 2018(9):005, September 2018.

[67] Maximilian H. Abitbol, David Alonso, Sara M. Simon, Jack Lashner, Kevin T. Crowley, Aamir M. Ali, Susanna Azzoni, Carlo Baccigalupi, Darcy Barron, Michael L. Brown, Erminia Calabrese, Julien Carron, Yuji Chinone, Jens Chluba, Gabriele Coppi, Kevin D. Crowley, Mark Devlin, Jo Dunkley, Josquin Errard, Valentina Fanfani, Nicholas Galitzki, Martina Gerbino, J. Colin Hill, Bradley R. Johnson, Baptiste Jost, Brian Keating, Nicoletta Krachmalnicoff, Akito Kusaka, Adrian T. Lee, Thibaut Louis, Mathew S. Madhavacheril, Heather McCarrick, Jeffrey McMahon, P. Daniel Meerburg, Federico Nati, Haruki Nishino, Lyman A. Page, Davide Poletti, Giuseppe Puglisi, Michael J. Randall, Aditya Rotti, Jacob Spisak, Aritoki Suzuki, Grant P. Teply, Clara Vergès, Edward J. Wollack, Zhilei Xu, and Mario Zannoni. The Simons Observatory: gain, bandpass and polarization-angle calibration requirements for B-mode searches. *J. Cosmology Astropart. Phys.*, 2021(5):032, May 2021.

[68] D. K. Lambert and P. L. Richards. Martin-Puplett interferometer: an analysis. *Appl. Opt.*, 17(10):1595–1602, May 1978.

[69] A. Kogut, D. J. Fixsen, D. T. Chuss, J. Dotson, E. Dwek, M. Halpern, G. F. Hinshaw, S. M. Meyer, S. H. Moseley, M. D. Seiffert, D. N. Spergel, and E. J. Wollack. The Primordial Inflation Explorer (PIXIE): a nulling polarimeter for cosmic microwave background observations. *J. Cosmology Astropart. Phys.*, 2011(7):025, July 2011.

[70] J. Maciel, F. Rodríguez, M. Mora-González, F. Gerardo, P. Lecona, V. Manuel, and D. Ramírez. Digital processing techniques for fringe analysis. In *Optical Interferometry*, 2017.

[71] F. Matsuda, L. Lowry, A. Suzuki, M. Aguilar Fáundez, K. Arnold, D. Barron, F. Bianchini, K. Cheung, Y. Chinone, T. Elleflot, G. Fabbian, N. Goeckner-Wald, M. Hasegawa, D. Kaneko, N. Katayama, B. Keating, A. T. Lee, M. Navaroli, H. Nishino, H. Paar, G. Puglisi, P. L. Richards, J. Seibert, P. Siritanasak, O. Tajima, S. Takatori, C. Tsai, and B. Westbrook. The POLARBEAR Fourier transform spectrometer calibrator and spectroscopic characterization of the POLARBEAR instrument. *Review of Scientific Instruments*, 90(11):115115, November 2019.

[72] F. Matsuda, L. Lowry, A. Suzuki, M. Aguilar Fáundez, K. Arnold, D. Barron, F. Bianchini, K. Cheung, Y. Chinone, T. Elleflot, G. Fabbian, N. Goeckner-Wald, M. Hasegawa, D. Kaneko, N. Katayama, B. Keating, A. T. Lee, M. Navaroli, H. Nishino, H. Paar, G. Puglisi, P. L. Richards, J. Seibert, P. Siritanasak, O. Tajima, S. Takatori, C. Tsai, and B. Westbrook. The POLARBEAR Fourier transform spectrometer calibrator and spectroscopic characterization of the POLARBEAR instrument. *Review of Scientific Instruments*, 90(11):115115, November 2019.

145

[73] W. Herres and J. Gronholz. Understanding ft-ir data processing. *Fourier Transform Infrared Spectrometry, 2nd ed.*, 1984.

[74] N. Krachmalnicoff, E. Carretti, C. Baccigalupi, G. Bernardi, S. Brown, B. M. Gaensler, M. Haverkorn, M. Kesteven, F. Perrotta, S. Poppi, and L. Staveley-Smith. S-PASS view of polarized Galactic synchrotron at 2.3 GHz as a contaminant to CMB observations. *A&A*, 618:A166, October 2018.

[75] R. H. Dicke. The Measurement of Thermal Radiation at Microwave Frequencies. *Review of Scientific Instruments*, 17(7):268–275, July 1946.

[76] ArtMechanic. *An aspheric biconvex lens.* Wikipedia, 2007.

[77] Joseph W. Goodman. *Introduction to Fourier optics.* McGraw-Hill, 2005.

[78] Blake D. Sherwin, Alexander van Engelen, Neelima Sehgal, Mathew Madhavacheril, Graeme E. Addison, Simone Aiola, Rupert Allison, Nicholas Battaglia, Daniel T. Becker, James A. Beall, J. Richard Bond, Erminia Calabrese, Rahul Datta, Mark J. Devlin, Rolando Dünner, Joanna Dunkley, Anna E. Fox, Patricio Gallardo, Mark Halpern, Matthew Hasselfield, Shawn Henderson, J. Colin Hill, Gene C. Hilton, Johannes Hubmayr, John P. Hughes, Adam D. Hincks, Renée Hlozek, Kevin M. Huffenberger, Brian Koopman, Arthur Kosowsky, Thibaut Louis, Loïc Maurin, Jeff McMahon, Kavilan Moodley, Sigurd Naess, Federico Nati, Laura Newburgh, Michael D. Niemack, Lyman A. Page, Jonathan Sievers, David N. Spergel, Suzanne T. Staggs, Robert J. Thornton, Jeff Van Lanen, Eve Vavagiakis, and Edward J. Wollack. Two-season Atacama Cosmology Telescope polarimeter lensing power spectrum. *Phys. Rev. D*, 95(12):123529, June 2017.

[79] Thibaut Louis, Emily Grace, Matthew Hasselfield, Marius Lungu, Loïc Maurin, Graeme E. Addison, Peter A. R. Ade, Simone Aiola, Rupert Allison, Mandana Amiri, Elio Angile, Nicholas Battaglia, James A. Beall, Francesco de Bernardis, J. Richard Bond, Joe Britton, Erminia Calabrese, Hsiao-mei Cho, Steve K. Choi, Kevin Coughlin, Devin Crichton, Kevin Crowley, Rahul Datta, Mark J. Devlin, Simon R. Dicker, Joanna Dunkley, Rolando Dünner, Simone Ferraro, Anna E. Fox, Patricio Gallardo, Megan Gralla, Mark Halpern, Shawn Henderson, J. Colin Hill, Gene C. Hilton, Matt Hilton, Adam D. Hincks, Renée Hlozek, S. P. Patty Ho, Zhiqi Huang, Johannes Hubmayr, Kevin M. Huffenberger, John P. Hughes, Leopoldo Infante, Kent Irwin, Simon Muya Kasanda, Jeff Klein, Brian Koopman, Arthur Kosowsky, Dale Li, Mathew Madhavacheril, Tobias A. Marriage, Jeff McMahon, Felipe Menanteau, Kavilan Moodley, Charles Munson, Sigurd Naess, Federico Nati, Laura Newburgh, John Nibarger, Michael D. Niemack, Michael R. Nolta, Carolina Nuñez, Lyman A. Page, Christine Pappas, Bruce Partridge, Felipe Rojas, Emmanuel Schaan, Benjamin L. Schmitt, Neelima Sehgal, Blake D. Sherwin, Jon Sievers, Sara Simon, David N. Spergel, Suzanne T. Staggs, Eric R. Switzer, Robert Thornton, Hy Trac, Jesse Treu, Carole Tucker, Alexander Van Engelen, Jonathan T. Ward, and Edward J. Wollack. The Atacama Cosmology

Telescope: two-season ACTPol spectra and parameters. *J. Cosmology Astropart. Phys.*, 2017(6):031, June 2017.

[80] Steve K. Choi, Matthew Hasselfield, Shuay-Pwu Patty Ho, Brian Koopman, Marius Lungu, Maximilian H. Abitbol, Graeme E. Addison, Peter A. R. Ade, Simone Aiola, David Alonso, Mandana Amiri, Stefania Amodeo, Elio Angile, Jason E. Austermann, Taylor Baildon, Nick Battaglia, James A. Beall, Rachel Bean, Daniel T. Becker, J. Richard Bond, Sarah Marie Bruno, Erminia Calabrese, Victoria Calafut, Luis E. Campusano, Felipe Carrero, Grace E. Chesmore, Hsiao-mei Cho, Susan E. Clark, Nicholas F. Cothard, Devin Crichton, Kevin T. Crowley, Omar Darwish, Rahul Datta, Edward V. Denison, Mark J. Devlin, Cody J. Duell, Shannon M. Duff, Adriaan J. Duivenvoorden, Jo Dunkley, Rolando Dünner, Thomas Essinger-Hileman, Max Fankhanel, Simone Ferraro, Anna E. Fox, Brittany Fuzia, Patricio A. Gallardo, Vera Gluscevic, Joseph E. Golec, Emily Grace, Megan Gralla, Yilun Guan, Kirsten Hall, Mark Halpern, Dongwon Han, Peter Hargrave, Shawn Henderson, Brandon Hensley, J. Colin Hill, Gene C. Hilton, Matt Hilton, Adam D. Hincks, Renée Hložek, Johannes Hubmayr, Kevin M. Huffenberger, John P. Hughes, Leopoldo Infante, Kent Irwin, Rebecca Jackson, Jeff Klein, Kenda Knowles, Arthur Kosowsky, Vincent Lakey, Dale Li, Yaqiong Li, Zack Li, Martine Lokken, Thibaut Louis, Amanda MacInnis, Mathew Madhavacheril, Felipe Maldonado, Maya Mallaby-Kay, Danica Marsden, Loïc Maurin, Jeff McMahon, Felipe Menanteau, Kavilan Moodley, Tim Morton, Sigurd Naess, Toshiya Namikawa, Federico Nati, Laura Newburgh, John P. Nibarger, Andrina Nicola, Michael D. Niemack, Michael R. Nolta, John Orlowski-Sherer, Lyman A. Page, Christine G. Pappas, Bruce Partridge, Phumlani Phakathi, Heather Prince, Roberto Puddu, Frank J. Qu, Jesus Rivera, Naomi Robertson, Felipe Rojas, Maria Salatino, Emmanuel Schaan, Alessandro Schillaci, Benjamin L. Schmitt, Neelima Sehgal, Blake D. Sherwin, Carlos Sierra, Jon Sievers, Cristobal Sifon, Precious Sikhosana, Sara Simon, David N. Spergel, Suzanne T. Staggs, Jason Stevens, Emilie Storer, Dhaneshwar D. Sunder, Eric R. Switzer, Ben Thorne, Robert Thornton, Hy Trac, Jesse Treu, Carole Tucker, Leila R. Vale, Alexander Van Engelen, Jeff Van Lanen, Eve M. Vavagiakis, Kasey Wagoner, Yuhan Wang, Jonathan T. Ward, Edward J. Wollack, Zhilei Xu, Fernando Zago, and Ningfeng Zhu. The Atacama Cosmology Telescope: a measurement of the Cosmic Microwave Background power spectra at 98 and 150 GHz. *J. Cosmology Astropart. Phys.*, 2020(12):045, December 2020.

[81] Sigurd Naess, Simone Aiola, Jason E. Austermann, Nick Battaglia, James A. Beall, Daniel T. Becker, Richard J. Bond, Erminia Calabrese, Steve K. Choi, Nicholas F. Cothard, Kevin T. Crowley, Omar Darwish, Rahul Datta, Edward V. Denison, Mark Devlin, Cody J. Duell, Shannon M. Duff, Adriaan J. Duivenvoorden, Jo Dunkley, Rolando Dünner, Anna E. Fox, Patricio A. Gallardo, Mark Halpern, Dongwon Han, Matthew Hasselfield, J. Colin Hill, Gene C. Hilton, Matt Hilton, Adam D. Hincks, Renée Hložek, Shuay-Pwu Patty Ho, Johannes Hubmayr, Kevin Huffenberger, John P. Hughes, Arthur B. Kosowsky, Thibaut Louis,

Mathew S. Madhavacheril, Jeff McMahon, Kavilan Moodley, Federico Nati, John P. Nibarger, Michael D. Niemack, Lyman Page, Bruce Partridge, Maria Salatino, Emmanuel Schaan, Alessandro Schillaci, Benjamin Schmitt, Blake D. Sherwin, Neelima Sehgal, Cristóbal Sifón, David Spergel, Suzanne Staggs, Jason Stevens, Emilie Storer, Joel N. Ullom, Leila R. Vale, Alexander Van Engelen, Jeff Van Lanen, Eve M. Vavagiakis, Edward J. Wollack, and Zhilei Xu. The Atacama Cosmology Telescope: arcminute-resolution maps of 18 000 square degrees of the microwave sky from ACT 2008–2018 data combined with Planck. *J. Cosmology Astropart. Phys.*, 2020(12):046, December 2020.

[82] Mathew S. Madhavacheril, J. Colin Hill, Sigurd Næss, Graeme E. Addison, Simone Aiola, Taylor Baildon, Nicholas Battaglia, Rachel Bean, J. Richard Bond, Erminia Calabrese, Victoria Calafut, Steve K. Choi, Omar Darwish, Rahul Datta, Mark J. Devlin, Joanna Dunkley, Rolando Dünner, Simone Ferraro, Patricio A. Gallardo, Vera Gluscevic, Mark Halpern, Dongwon Han, Matthew Hasselfield, Matt Hilton, Adam D. Hincks, Renée Hložek, Shuay-Pwu Patty Ho, Kevin M. Huffenberger, John P. Hughes, Brian J. Koopman, Arthur Kosowsky, Martine Lokken, Thibaut Louis, Marius Lungu, Amanda MacInnis, Loïc Maurin, Jeffrey J. McMahon, Kavilan Moodley, Federico Nati, Michael D. Niemack, Lyman A. Page, Bruce Partridge, Naomi Robertson, Neelima Sehgal, Emmanuel Schaan, Alessandro Schillaci, Blake D. Sherwin, Cristóbal Sifón, Sara M. Simon, David N. Spergel, Suzanne T. Staggs, Emilie R. Storer, Alexander van Engelen, Eve M. Vavagiakis, Edward J. Wollack, and Zhilei Xu. Atacama Cosmology Telescope: Component-separated maps of CMB temperature and the thermal Sunyaev-Zel'dovich effect. *Phys. Rev. D*, 102(2):023534, July 2020.

[83] E. M. Vavagiakis, P. A. Gallardo, V. Calafut, S. Amodeo, S. Aiola, J. E. Austermann, N. Battaglia, E. S. Battistelli, J. A. Beall, R. Bean, J. R. Bond, E. Calabrese, S. K. Choi, N. F. Cothard, M. J. Devlin, C. J. Duell, S. M. Duff, A. J. Duivenvoorden, J. Dunkley, R. Dunner, S. Ferraro, Y. Guan, J. C. Hill, G. C. Hilton, M. Hilton, R. Hložek, Z. B. Huber, J. Hubmayr, K. M. Huffenberger, J. P. Hughes, B. J. Koopman, A. Kosowsky, Y. Li, M. Lokken, M. Madhavacheril, J. McMahon, K. Moodley, S. Naess, F. Nati, L. B. Newburgh, M. D. Niemack, L. A. Page, B. Partridge, E. Schaan, A. Schillaci, C. Sifón, D. N. Spergel, S. T. Staggs, J. N. Ullom, L. R. Vale, A. Van Engelen, J. Van Lanen, E. J. Wollack, and Z. Xu. The Atacama Cosmology Telescope: Probing the baryon content of SDSS DR15 galaxies with the thermal and kinematic Sunyaev-Zel'dovich effects. *Phys. Rev. D*, 104(4):043503, August 2021.

[84] Omar Darwish, Mathew S. Madhavacheril, Blake D. Sherwin, Simone Aiola, Nicholas Battaglia, James A. Beall, Daniel T. Becker, J. Richard Bond, Erminia Calabrese, Steve K. Choi, Mark J. Devlin, Jo Dunkley, Rolando Dünner, Simone Ferraro, Anna E. Fox, Patricio A. Gallardo, Yilun Guan, Mark Halpern, Dongwon Han, Matthew Hasselfield, J. Colin Hill, Gene C. Hilton, Matt Hilton, Adam D. Hincks, Shuay-Pwu Patty Ho, J. Hubmayr, John P. Hughes, Brian J. Koopman, Arthur Kosowsky, J. Van Lanen, Thibaut Louis, Marius Lungu,

Amanda MacInnis, Loïc Maurin, Jeffrey McMahon, Kavilan Moodley, Sigurd Naess, Toshiya Namikawa, Federico Nati, Laura Newburgh, John P. Nibarger, Michael D. Niemack, Lyman A. Page, Bruce Partridge, Frank J. Qu, Naomi Robertson, Alessandro Schillaci, Benjamin Schmitt, Neelima Sehgal, Cristóbal Sifón, David N. Spergel, Suzanne Staggs, Emilie Storer, Alexander van Engelen, and Edward J. Wollack. The Atacama Cosmology Telescope: a CMB lensing mass map over 2100 square degrees of sky and its cross-correlation with BOSS-CMASS galaxies. *MNRAS*, 500(2):2250–2263, January 2021.

[85] Toshiya Namikawa, Yilun Guan, Omar Darwish, Blake D. Sherwin, Simone Aiola, Nicholas Battaglia, James A. Beall, Daniel T. Becker, J. Richard Bond, Erminia Calabrese, Grace E. Chesmore, Steve K. Choi, Mark J. Devlin, Joanna Dunkley, Rolando Dünner, Anna E. Fox, Patricio A. Gallardo, Vera Gluscevic, Dongwon Han, Matthew Hasselfield, Gene C. Hilton, Adam D. Hincks, Renée Hložek, Johannes Hubmayr, Kevin Huffenberger, John P. Hughes, Brian J. Koopman, Arthur Kosowsky, Thibaut Louis, Marius Lungu, Amanda MacInnis, Mathew S. Madhavacheril, Maya Mallaby-Kay, Loïc Maurin, Jeffrey McMahon, Kavilan Moodley, Sigurd Naess, Federico Nati, Laura B. Newburgh, John P. Nibarger, Michael D. Niemack, Lyman A. Page, Frank J. Qu, Naomi Robertson, Alessandro Schillaci, Neelima Sehgal, Cristóbal Sifón, Sara M. Simon, David N. Spergel, Suzanne T. Staggs, Emilie R. Storer, Alexander van Engelen, Jeff van Lanen, and Edward J. Wollack. Atacama Cosmology Telescope: Constraints on cosmic birefringence. *Phys. Rev. D*, 101(8):083527, April 2020.

[86] Susmita Adhikari, Tae-hyeon Shin, Bhuvnesh Jain, Matt Hilton, Eric Baxter, Chihway Chang, Risa H. Wechsler, Nick Battaglia, J. Richard Bond, Sebastian Bocquet, Joseph DeRose, Steve K. Choi, Mark Devlin, Jo Dunkley, August E. Evrard, Simone Ferraro, J. Colin Hill, John P. Hughes, Patricio A. Gallardo, Martine Lokken, Amanda MacInnis, Jeffrey McMahon, Mathew S. Madhavacheril, Frederico Nati, Laura B. Newburgh, Michael D. Niemack, Lyman A. Page, Antonella Palmese, Bruce Partridge, Eduardo Rozo, Eli Rykoff, Maria Salatino, Alessandro Schillaci, Neelima Sehgal, Cristóbal Sifón, Chun-Hao To, Ed Wollack, Hao-Yi Wu, Zhilei Xu, Michel Aguena, Sahar Allam, Alexandra Amon, James Annis, Santiago Avila, David Bacon, Emmanuel Bertin, Sunayana Bhargava, David Brooks, David L. Burke, Aurelio C. Rosell, Matias Carrasco Kind, Jorge Carretero, Francisco Javier Castander, Ami Choi, Matteo Costanzi, Luiz N. da Costa, Juan De Vicente, Shantanu Desai, Thomas H. Diehl, Peter Doel, Spencer Everett, Ismael Ferrero, Agnès Ferté, Brenna Flaugher, Pablo Fosalba, Josh Frieman, Juan García-Bellido, Enrique Gaztanaga, Daniel Gruen, Robert A. Gruendl, Julia Gschwend, Gaston Gutierrez, Will G. Hartley, Samuel R. Hinton, Devon L. Hollowood, Klaus Honscheid, David J. James, Tesla Jeltema, Kyler Kuehn, Nikolay Kuropatkin, Ofer Lahav, Marcos Lima, Marcio A. G. Maia, Jennifer L. Marshall, Paul Martini, Peter Melchior, Felipe Menanteau, Ramon Miquel, Robert Morgan, Ricardo L. C. Ogando, Francisco Paz-Chinchón, Andrés Plazas Malagón, Eusebio Sanchez, Basilio Santiago, Vic

Scarpine, Santiago Serrano, Ignacio Sevilla-Noarbe, Mathew Smith, Marcelle Soares-Santos, Eric Suchyta, Molly E. C. Swanson, Tamas N. Varga, Reese D. Wilkinson, Yuanyuan Zhang, Jason E. Austermann, James A. Beall, Daniel T. Becker, Edward V. Denison, Shannon M. Duff, Gene C. Hilton, Johannes Hubmayr, Joel N. Ullom, Jeff Van Lanen, Leila R. Vale, DES Collaboration, and ACT Collaboration. Probing galaxy evolution in massive clusters using ACT and DES: splashback as a cosmic clock. *arXiv e-prints*, page arXiv:2008.11663, August 2020.

[87] V. Calafut, P. A. Gallardo, E. M. Vavagiakis, S. Amodeo, S. Aiola, J. E. Austermann, N. Battaglia, E. S. Battistelli, J. A. Beall, R. Bean, J. R. Bond, E. Calabrese, S. K. Choi, N. F. Cothard, M. J. Devlin, C. J. Duell, S. M. Duff, A. J. Duivenvoorden, J. Dunkley, R. Dunner, S. Ferraro, Y. Guan, J. C. Hill, G. C. Hilton, M. Hilton, R. Hložek, Z. B. Huber, J. Hubmayr, K. M. Huffenberger, J. P. Hughes, B. J. Koopman, A. Kosowsky, Y. Li, M. Lokken, M. Madhavacheril, J. McMahon, K. Moodley, S. Naess, F. Nati, L. B. Newburgh, M. D. Niemack, L. A. Page, B. Partridge, E. Schaan, A. Schillaci, C. Sifón, D. N. Spergel, S. T. Staggs, J. N. Ullom, L. R. Vale, A. Van Engelen, J. Van Lanen, E. J. Wollack, and Z. Xu. The Atacama Cosmology Telescope: Detection of the pairwise kinematic Sunyaev-Zel'dovich effect with SDSS DR15 galaxies. *Phys. Rev. D*, 104(4):043502, August 2021.

[88] John Orlowski-Scherer, Luca Di Mascolo, Tanay Bhandarkar, Alex Manduca, Tony Mroczkowski, Stefania Amodeo, Nick Battaglia, Mark Brodwin, Steve K. Choi, Mark Devlin, Simon Dicker, Jo Dunkley, Anthony H. Gonzalez, Dongwon Han, Matt Hilton, Kevin Huffenberger, John P. Hughes, Amanda MacInnis, Kenda Knowles, Brian J. Koopman, Ian Lowe, Kavilan Moodley, Federico Nati, Michael D. Niemack, Lyman A. Page, Bruce Partridge, Charles Romero, Maria Salatino, Alessandro Schillaci, Neelima Sehgal, Cristóbal Sifón, Suzanne Staggs, S. A. Stanford, Robert Thornton, Eve M. Vavagiakis, Edward J. Wollack, Zhilei Xu, and Ningfeng Zhu. Atacama Cosmology Telescope measurements of a large sample of candidates from the Massive and Distant Clusters of WISE Survey: Sunyaev-Zeldovich effect confirmation of MaDCoWS candidates using ACT. *arXiv e-prints*, page arXiv:2105.00068, April 2021.

[89] K. N. Abazajian, K. Arnold, J. Austermann, B. A. Benson, C. Bischoff, J. Bock, J. R. Bond, J. Borrill, E. Calabrese, J. E. Carlstrom, C. S. Carvalho, C. L. Chang, H. C. Chiang, S. Church, A. Cooray, T. M. Crawford, K. S. Dawson, S. Das, M. J. Devlin, M. Dobbs, S. Dodelson, O. Doré, J. Dunkley, J. Errard, A. Fraisse, J. Gallicchio, N. W. Halverson, S. Hanany, S. R. Hildebrandt, A. Hincks, R. Hlozek, G. Holder, W. L. Holzapfel, K. Honscheid, W. Hu, J. Hubmayr, K. Irwin, W. C. Jones, M. Kamionkowski, B. Keating, R. Keisler, L. Knox, E. Komatsu, J. Kovac, C. L. Kuo, C. Lawrence, A. T. Lee, E. Leitch, E. Linder, P. Lubin, J. McMahon, A. Miller, L. Newburgh, M. D. Niemack, H. Nguyen, H. T. Nguyen, L. Page, C. Pryke, C. L. Reichardt, J. E. Ruhl, N. Sehgal, U. Seljak, J. Sievers, E. Silverstein, A. Slosar, K. M. Smith, D. Spergel, S. T. Staggs, A. Stark, R. Stompor,

A. G. Vieregg, G. Wang, S. Watson, E. J. Wollack, W. L. K. Wu, K. W. Yoon, and O. Zahn. Neutrino physics from the cosmic microwave background and large scale structure. *Astroparticle Physics*, 63:66–80, March 2015.